Advances in Acoustics and Vibration

Active Noise Control

Guest Editor: Marek Pawelczyk

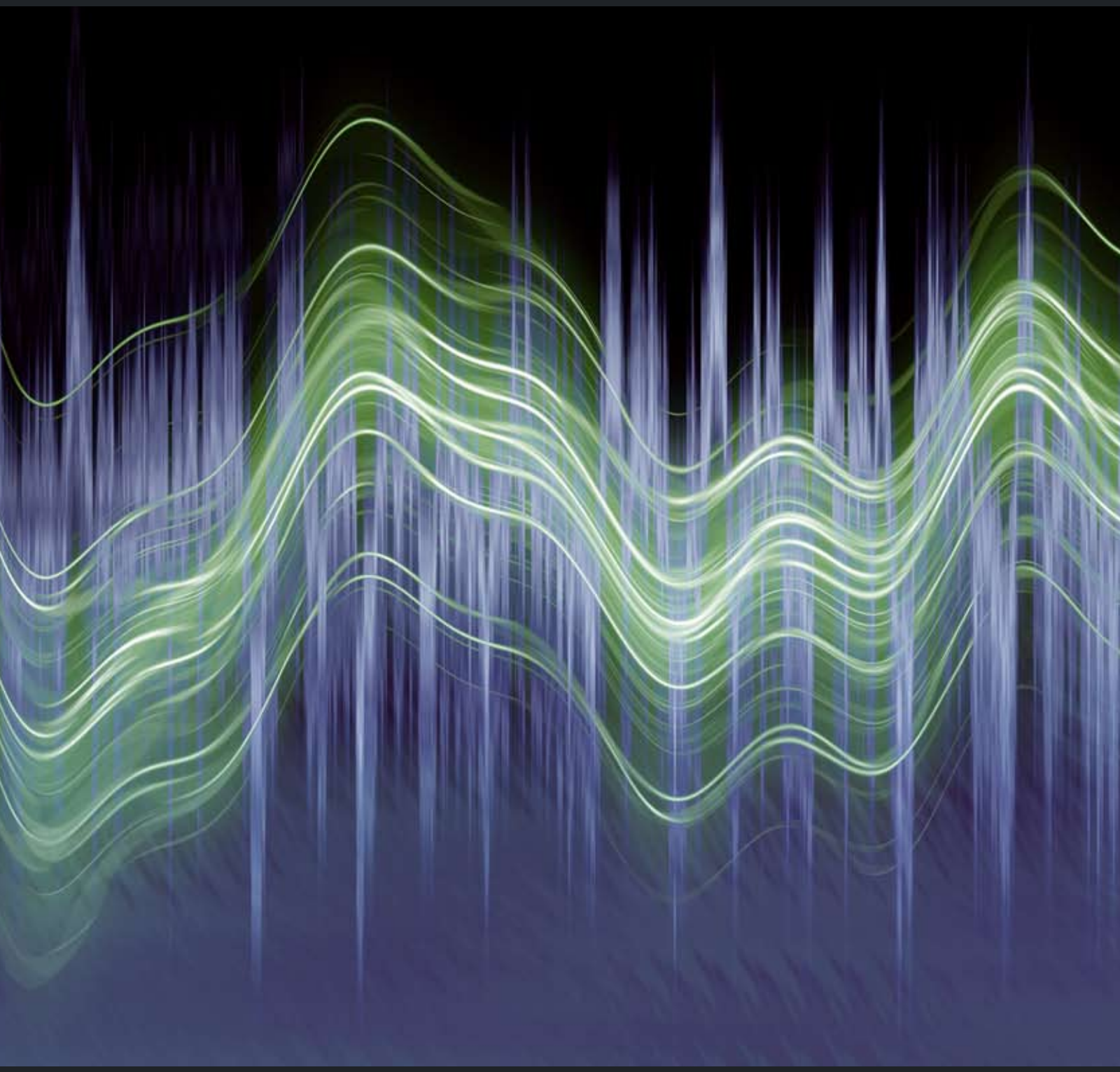

Active Noise Control

Advances in Acoustics and Vibration

Active Noise Control

Guest Editor: Marek Pawelczyk

Contents

Hindawi Publishing Corporation
Advances in Acoustics and Vibration
Volume 2008, Article ID 350943, 2 pages
doi:10.1155/2008/350943

Editorial
Active Noise Control

Marek Pawelczyk

Institute of Automatic Control, Silesian University of Technology, Akademicka 16 Street, 44-101 Gliwice, Poland

Correspondence should be addressed to Marek Pawelczyk, marek.pawelczyk@polsl.pl

Received 16 June 2008; Accepted 16 June 2008

Active noise control generally aims at reducing an unwanted and unpleasant sound referred to as the noise. The general idea is very simple. However, there are many problems related to the acoustic phenomena as well as control limitations. Thus, the problem is still exciting and attracts attention of a number of scientists originating from different scientific disciplines. Rapid development of technology and extensive research allow for manufacturing sensors and actuators of more advantegous properties, designing more robust and effective algorithms, and finally performing succesful applications in different noise pollutted areas.

The aim of the special issue is just to present recent advances in active noise control and its applications. I would like to thank all the authors who accepted my invitation and decided to share their work with a wide circle of readers, what the open-access journal offers. The papers published in this issue were peer-reviewed by independent experts. I appreciate help of the experts very much. Even four reviews per paper where made. Therefore, the eight papers which are finally included in the issue are of very high quality. Below I am barely announcing main topics discussed in the issue.

A novel audiointegrated approach to achieving active noise control for incubators is proposed by L. Liu et al. The system reduces excessive broadband noise in neonatal care units and in incubators, which is generally due to ventillation or breathing equipment. Therefore, the system tries to protect against auditory damage to preterm infants both due to short-term and long-term effects. At the same time, the system recreates prenatal ambience for premature infants. In particular, an efficient robust nonlinear FXLMS-based adaptive control algorithm is presented. It allows for stable operation of the ANC system in the presence of impulsive interference in the input.

An integrated control system is designed by L. Wang et al. to improve bass reproduction of the audio equippment and cancel engine noise in the cabins of automobiles. The problem is difficult because of the frequency overlap of the bass audio sound and engine noise. On the other hand, small volume of the cabin and poor low-frequency performance of loudspeakers need special approach. The proposed system equalizes the engine-noise harmonics based on the bass information to enhance the low-frequency part of the audio signal. The system responses also to variations of engine-noise frequencies. Multifrequency approaches to active noise equalization with frequency-sampling filters are used.

A system with a pair of loudspeakers is designed by D. Bismor to create a virtual unidirectional sound source. It enables successful cancellation of the acoustic feedback effect and, if supplemented by an active control system, efficient cancellation of the acoustic noise propagating downstream. Both fixed parameter and adaptive solutions are used. In the latter case, the problem of a hazard in tuning the virtual unidirectional sound source and active noise control algorithm is disclosed and guidelines for scheduling those operations are given. The overall system has been validated for noise control in an acoustic duct.

An active noise control system with online modelling of time-varying acoustic paths is designed by J. Yuan. Contrary to most publications, any external signal and thus persistent excitation is not required. Instead, orthogonal adaptation is used to cancel the acoustic feedback in order to recover the reference signal. The proposed system's behavior is stable and converges quickly even in case of significant and rapid changes of the acoustic path inside a duct.

A Hinf optimal control system with a pair of loudspeakers is proposed by Y. Kobayashi and H. Fujioka. As a fixed parameter solution it requires significantly less computations than an adaptive solution and still recovers benefits of the Swinbanks' source. However, by considering the pair of loudspeakers as two independent actuators, it gives more

flexibility and better noise control results are possible. The system is suitable for ventilation ducts in houses.

A modification of the FXLMS algorithm is proposed by S. P. Lovstedt et al. in order to compensate for its frequency dependent convergence behavior, which is particularly severe for plants responding with high peaks and deep valleys. Magnitude of the frequency response of the secondary path model is modified using a genetic algorithm to equalize eigenvalues of the autocorrelation matrix of the filtered-reference signal, while preserving phase of the frequency response of the model. As a result, higher attenuation and faster convergence are observed. In the experiments, swept tone noise and multiple tone noise, important in terms of many practical applications, are considered.

An active sound intensity probe consisting of a sound hard tube terminated by aloudspeaker and equipped with a pair of microphones is designed by T. Kletschkowski and D.Sachau. Active control techniques are used to generate acoustic free field conditions in the tube. Thus, the probe acts as a local sound absorber and therefore the effect of the device on a source is reduced. The probe can be used for sound source localization, especially in weakly damped interior noise fields at low frequencies.

A state-feedback control system is proposed by V. Lhuillier et al. in order to reduce sound transmission through a panel excited by an acoustic wave. The effect of decreasing eigen frequencies of high-radiation modes and thus reducing vibration amplitudes at resonance frequencies by adding active modal masses is used. This effect can also be considered as virtual transformations of structures that can be used in the field of sound quality.

I believe that this special issue will be found interesting by the active noise control community.

Marek Pawelczyk

Hindawi Publishing Corporation
Advances in Acoustics and Vibration
Volume 2008, Article ID 495317, 9 pages
doi:10.1155/2008/495317

Research Article

Still in Womb: Intrauterine Acoustic Embedded Active Noise Control for Infant Incubators

Lichuan Liu, Shruthi Gujjula, Priya Thanigai, and Sen M. Kuo

Department of Electrical Engineering, Northern Illinois University, DeKalb, IL 60115, USA

Correspondence should be addressed to Lichuan Liu, ll24@njit.edu

Received 1 December 2007; Revised 4 February 2008; Accepted 5 March 2008

Recommended by Marek Pawelczyk

Excessive noise in neonatal care units and inside incubators can have a number of detrimental effects on an infant's health. We proposed a novel, audio-integrated approach to achieve active noise control (ANC) for infant incubators. We also presented the implementation of the robust, nonlinear filtered-X least mean M-estimate algorithm, for reducing impulsive interference in incubators. The healthcare application is further enhanced by integrating the "womb effect", that is, by using intrauterine and maternal heart sounds, proven to be beneficial to infant health, for soothing the infant and masking the residual noise. A computer model for audio-integrated noise cancellation utilizing experimentally measured transfer functions is developed for simulations using real medical equipment noise. The simulation of the audio integrated ANC system produced optimal results and the system was further validated by real-time experiments to be robust and efficient.

1. INTRODUCTION

Neonatal intensive care units (NICU) house and treat premature infants until their organ systems are considered fully developed. These infants are enclosed in incubators, as shown in Figure 1, that monitor their vital statistics and ensure that environmental conditions are maintained at optimum levels. The incubators create the precise and consistent environment [1], such as temperature and humidity, controlled by microprocessor. However, according to the American Academy of Pediatrics [2], high noise levels are common in the NICU and in incubators, causing considerable auditory damage to preterm infants [3]. The noise is typically due to ventilation or breathing equipment and human activity. Figure 2 is an example of the real incubator noise in time domain with segments marked by impulse due to respiratory pumps and the background equipment hum. The consequences of exposing infants to incubator noise vary from short-term effects such as sleep disturbance to long-term effects such as delayed speech development. To reduce medical equipment noise and external noise from the NICU, passive control systems such as absorbers [4] are not always efficient. This puts forth a need for an active noise control (ANC) system that can cancel noise inside the incubator adaptively [5, 6]. Another approach to create a healthier ambience in NICUs is the introduction of intrauterine audio into the incubator that allows the infant to feel comforted. Intrauterine audio is a combination of low-frequency sounds from the womb and includes the sound of the muffled heartbeat which can be heard distinctly in the background.

However, neither playing soothing audio nor applying an ANC system is individually efficient creating the need for an integrated system that can reduce harmful equipment noise while simultaneously playing beneficial intrauterine audio. To achieve this end, this paper proposes an innovative application for neonatal healthcare—the intrauterine acoustics embedded active noise controller. The integrated system aims at recreating prenatal ambience for premature infants who are required to spend extended periods enclosed inside infant incubators.

Section 2 of the paper discusses the positive effects of playing uterine audio to premature infants. These positive effects are both medical and psychological, and reflect results from studies carried out over the last three decades. Section 3 focuses on developing an ANC system utilizing the filtered-X least mean square (FXLMS) algorithm for cancellation of broadband noise using transfer functions

Figure 1: Mobile incubator unit: Giraffe Incubator by GE Healthcare.

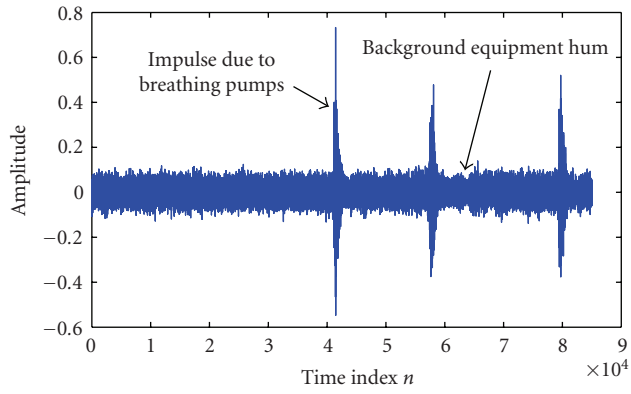

Figure 2: Example wave form of incubator noise, sampling frequency $f_s = 4$ KHz.

measured from the real GE Healthcare Girraffe incubator. The laboratory setup was modeled using the same incubator shown in Figure 1. Section 4 introduces the novel filtered-X least mean M-estimate (FXLMM) algorithm that is found to be statistically robust in the presence of impulsive interference in the input. Section 5 outlines the audio-integration algorithm that introduces intrauterine audio and allows it to be played simultaneously while the ANC system is in operation. This integration serves two important purposes—it provides a potential health benefit for infants by utilizing womb sounds as heard by the infant and also masks the residual noise after noise cancellation has been performed. The algorithm is intended to prevent interference from the soothing audio on the performance of the ANC algorithm and ensures that the audio is not cancelled by the ANC system. The audio interference cancellation filter also performs online modeling of the secondary path to enhance the performance of the ANC system. Section 6 shows the simulation and real time experiment results.

2. A STUDY OF NEONATAL RESPONSE TO UTERINE SOUNDS

This section briefly reviews that the numerous benefits intrauterine audio has on neonatal growth from [5]. It is widely accepted that the brain of the fetus develops while it is inside the womb. An infant's ears begin to develop when it is around eight weeks old and can be considered fully developed by the twenty-fourth week. The development of the inner ears and the nerve endings from the brain is so advanced that the baby can hear the muffled sounds of the heartbeat and the blood flowing through the umbilical cord. The human cochlear system, which is considered fully developed by the twenty-fourth week, transforms acoustic vibrations into nervous influx allowing infants to have an understanding of rhythm at a very early stage [7]. These sounds form an imprint on the fetal brain and it has been verified that post birth, the infant is comforted while listening to it.

Playing soothing audio has always been known to relieve stress and has in recent years become an established form of therapy. There have been a number of studies that indicate that music has a positive impact on premature infants yet the kind of audio to be played is contentious. The various available options include playing nature sounds, live and recorded music. But "womb music" has consistently been considered the most favorable choice. According to [7] the womb is not a silent place and is typically awash with sounds. Sounds that are heard inside the uterus include maternal heartbeat, respiration, intestinal gurgling and sounds from blood vessels. The maternal heartbeat heard by the infant is a muffled version of the original as it passes through layers of tissues before reaching the infant. A study conducted by Rosner and Doherty in [8] states that "playing prerecorded intrauterine sounds to newborns reportedly soothes the babies." The study concluded that 90% of infants who listened to intrauterine audio were calmed down significantly.

In another study conducted by Murooka et al. [9], the authors used a piezoelectric microphone to record and analyze intrauterine sounds. The sounds were found to be mainly from blood vessels and were found to produce a calming effect on 86% of the infants, and 30% of the infants were found to have increased sleep cycles. The authors asserted that playing such sounds externally recreates the "in-utero" ambience for infants [9]. A pioneering study conducted by Salk [10] exposed neonates to prerecorded maternal heartbeat and concluded that test infants showed increased weight gain and food intake. Flowers, McCain, and Hilker combined uterine sounds with soft ballads and tested the impact of music on nine African-American premature infants. The infants displayed improvement in respiration rate, oxygen saturation, and time spent in sleeping [11].

This paper therefore proposes the utilization of sound files from a commercially available product—the Baby Sleep System [12]. The soothing audio consists of intrauterine heartbeat recorded through a condenser microphone, which is a very accurate representation of uterine sounds as heard by the infant. The heartbeats were taken at 72 beats per minute, the rate of a relaxed adult heart. They were combined

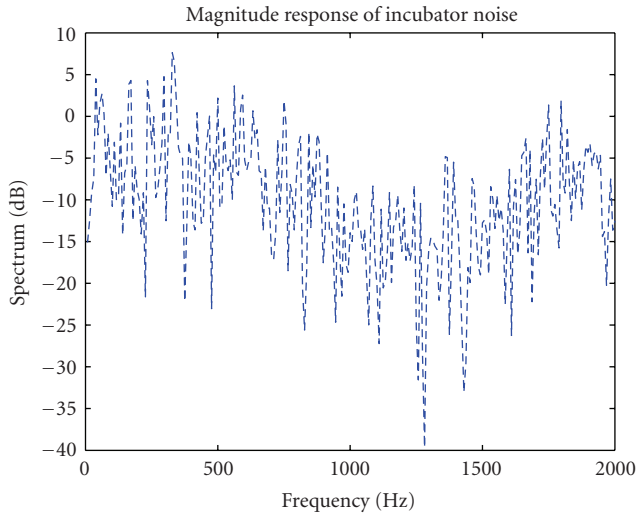

Figure 3: Magnitude response of the incubator wideband noise.

with the sound of blood and fluid movement to produce an "in-utero" effect for the infant. This audio was incorporated along with the ANC system and serves two main purposes. The ANC system is optimized to cancel equipment and external NICU noise to the maximum possible extent. The audio integration allows for the soothing audio to be played continuously without interfering with the ANC system. Also, the integrated system can be considered cost effective as the power amplifiers and loudspeakers used by the ANC system can be used for playing the soothing audio, thus maximizing the utility of resources.

3. ACTIVE NOISE CONTROL FOR THE INCUBATORS

The noise in incubator can be classified as broadband noise because it covers a wide range of frequencies [13]. The noise sources are some medical equipments in the ICU, such as a blowers, nebulizers, humidifiers, and pumps. Figure 3 shows the magnitude spectrum of the recorded sample of broadband incubator noise. We can find that the power of the noise is spread over a wide spectrum of the noise signal. The ANC systems can be used to cancel this high-power wideband noise.

ANC is based on the principle of untilizing destructive interference to cancel unwanted noise. The objective of an ANC system is to generate an "antinoise" to cancel the primary noise. The amount of noise which can be cancelled depends on the accuracy of the amplitude and phase of this antinoise [14].

The block diagram of a feedforward broadband ANC system using the FXLMS algorithm is illustrated in Figure 4, where $P(z)$ is the transfer function of the primary path from the noise source to the error microphones, $S(z)$ is the transfer function of secondary path and $\hat{S}(z)$ is its estimate. The primary noise $d(n)$ inside the incubator is cancelled by the antinoise $y(n)$ generated by the adaptive filter $W(z)$. The antinoise is produced by the secondary loudspeakers and $e(n)$ is the residual noise picked up by the error microphone.

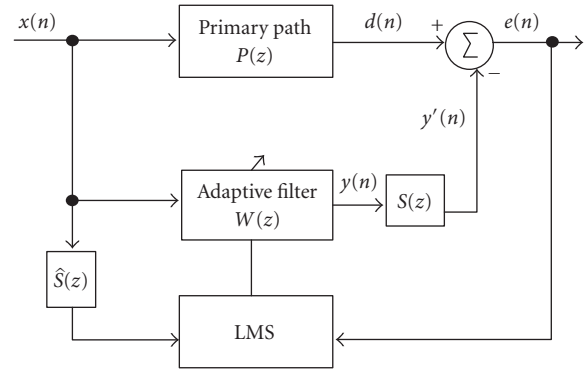

Figure 4: Block diagram of ANC system with the FXLMS algorithm.

In Figure 4, $S(z)$ which is the secondary path between $e(n)$ and $y(n)$, includes the secondary loudspeakers, error microphones, and acoustic path between the loudspeakers and the error microphones. The secondary path is modeled offline and retained during the online operation of ANC. The estimate compensates for the secondary-path effects [15].

The output of the adaptive filter can be represented as [15]

$$y(n) = \mathbf{w}^T(n)\mathbf{x}(n), \tag{1}$$

where $\mathbf{w}(n) = [w_0(n)\ w_1(n) \cdots w_{L-1}(n)]^T$ is the coefficient vector of the adaptive filter $W(z)$ and $\mathbf{x}(n) = [x(n)\ x(n-1) \cdots x(n-L+1)]^T$ is the $L \times 1$ reference signal vector. The signal $y(n)$ is filtered through the secondary path $S(z)$ and is subtracted from the primary noise $d(n)$ to generate the residual error $e(n)$. The equations for simulation are given by

$$\begin{aligned} d(n) &= p(n) * x(n), \\ y'(n) &= s(n) * y(n), \\ e(n) = d(n) - y'(n) &= d(n) - s(n) * [\mathbf{w}^T(n)\mathbf{x}(n)], \end{aligned} \tag{2}$$

where $*$ denotes the convolution operator, and $p(n)$ and $s(n)$ are the primary and secondary path responses, respectively. All these operations are carried out by the system internally and the signals picked up in real-time ANC are the reference signal $x(n)$ and the residual error $e(n)$. For the adaptive filter, the weight update equation is

$$\mathbf{w}(n+1) = \mathbf{w}(n) + \mu e(n)\mathbf{x}'(n), \tag{3}$$

μ is the step size; $\mathbf{x}'(n) = [x'(n)\ x'(n-1) \cdots x'(n-L+1)]^T$ is the reference signal vector $\mathbf{x}(n)$ filtered by the secondary path model $\hat{S}(z)$,

$$x'(n) = \hat{s}(n) * x(n), \tag{4}$$

where $\hat{s}(n)$ is an accurate estimate of $s(n)$.

The experimental setup is shown in Figure 5. One microphone is placed on either side of the infant head. The outputs from both are analyzed by a spectrum analyzer.

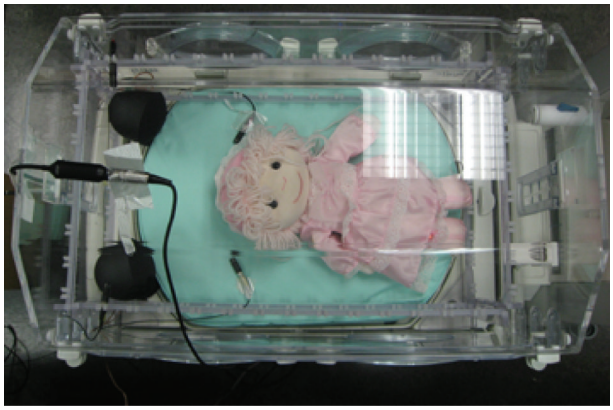

Figure 5: Experiment setup by using the GE Healthcare Giraffe Incubator.

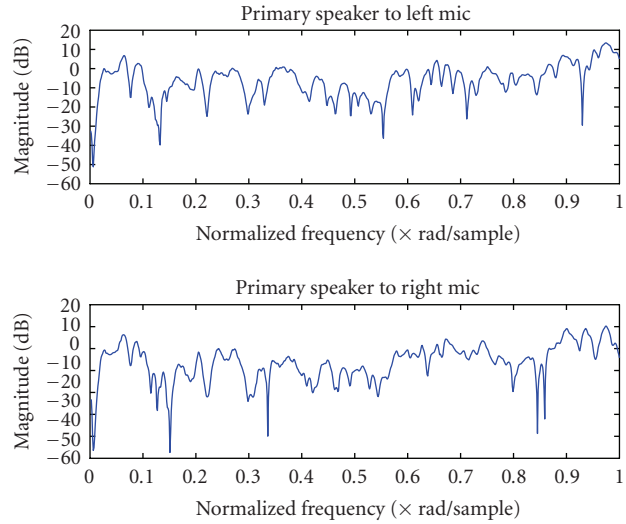

Figure 6: Magnitude responses of the primary paths.

The cancelling loudspeakers are placed in the incubator, and can be seen behind the infant head. Typically the offline modeling of the secondary paths from the cancelling loudspeakers to the error microphones is using adaptive filters with the least mean square algorithm. The magnitude responses of the primary paths $P(z)$ from the experimental setup are shown in Figure 6.

Typically, white noise is used for adaptive system identification. But it is found to be annoying especially in sensitive environments like the NICU. The proposed method utilizes offline modeling approach. Nature's sound, in this case, the sound of a flowing stream is used. Nature's sounds are preferred owing to their flat spectrum and their pleasing effect on the listener. The secondary paths estimator converged for a filter length of 30. Satisfactory results of offline modeling are shown in Figure 7.

4. NONLINEAR ALGORITHM FOR IMPULSE NOISE SUPPRESSION

The performance of the linear adaptive filters degrade dramatically in the presence of impulse noise, therefore nonlinear algorithms are capable of reducing the adverse effects [16]. The FXLMM algorithm is a simple and robust method. It employs the mean M-estimation error objective function and is capable of performing effectively in impulsive environment [17–19].

The objective of the adaptive filter $W(z)$ is to minimize the least M-estimate function criterion $\rho[e(i)]$ where $\rho(\cdot)$ is the M-estimate function. The coefficient vector $\mathbf{w}(n)$ is updated in the negative direction of the gradient vector

$$\mathbf{w}(n+1) = \mathbf{w}(n) - \mu \nabla J_{MP} \tag{5}$$

and the objective function is

$$J_{MP} \equiv E[\rho[e(n)]] \cong \rho[e(n)], \tag{6}$$

where $E[\cdot]$ is the expectation operator, $\rho(\cdot)$ is chosen to be the Hampel three-part redescending M-estimate function, which is well known for its computational simplicity. It defines as

$$\rho[e(n)] = \begin{cases} \dfrac{e^2(n)}{2}, & 0 \le |e(n)| < \xi, \\ \xi|e(n)| - \dfrac{\xi^2}{2}, & \xi \le |e(n)| < \Delta_1, \\ \dfrac{\xi}{2(\Delta_1+\Delta_2)} - \dfrac{\xi^2}{2} + \dfrac{(\xi|e(n)| - \Delta_2)^2}{2(\Delta_1-\Delta_2)}, & \Delta_1 \le |e(n)| < \Delta_2, \\ \dfrac{\xi}{2(\Delta_1+\Delta_2)} - \dfrac{\xi^2}{2}, & \Delta_2 \le |e(n)|, \end{cases} \tag{7}$$

where ξ, Δ_1, and Δ_2 are the threshold parameters.

The objective function is minimized by

$$\nabla J_{MP} = \frac{\partial J_{MP(n)}}{\partial \mathbf{w}(n)} = \frac{\partial \rho[e(n)]}{\partial e(n)} \frac{\partial e(n)}{\partial \mathbf{w}(n)}. \tag{8}$$

Let $\psi[e(n)]$ be the first-order partial derivative of $\rho[e(n)]$, (8) becomes

$$\begin{aligned} \nabla J_{MP} &= \psi[e(n)] \frac{\partial e(n)}{\partial \mathbf{w}(n)} = \psi[e(n)][-s(n) * \mathbf{x}(n)] \\ &= -q[e(n)]e(n)[s(n) * \mathbf{x}(n)]. \end{aligned} \tag{9}$$

Define $q[e(n)] \equiv \psi[e(n)]/e(n)$ as the weight function. Since $s(n)$ is the impulse response of the secondary path and not available directly, we use its estimation to calculate the gradient,

$$\nabla J_{MP} \cong -q[e(n)]e(n)[\hat{s}(n) * \mathbf{x}(n)] = -q[e(n)]e(n)\mathbf{x}'(n). \tag{10}$$

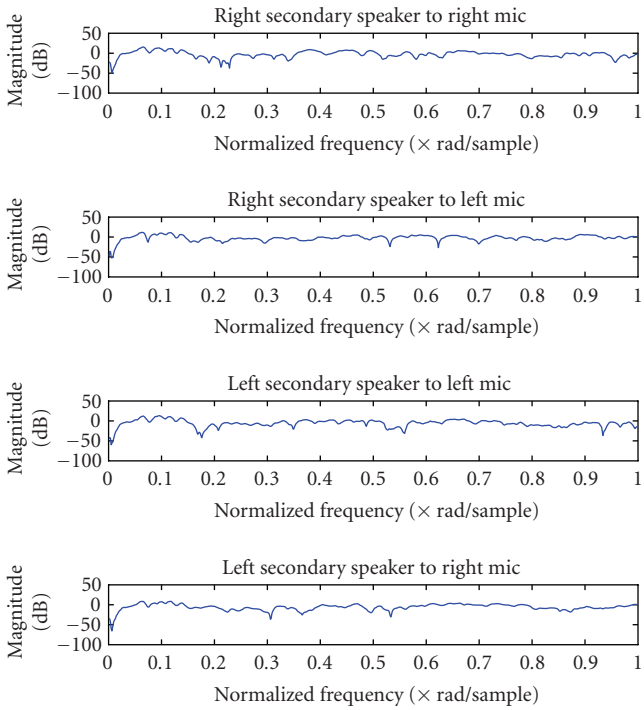

Figure 7: Magnitude responses of the secondary paths.

Substituting (10) into (5), we can get the weight vector update equation as

$$\mathbf{w}(n+1) = \mathbf{w}(n) + \mu q[e(n)]e(n)\mathbf{x}'(n), \tag{11}$$

where μ is the step size parameter. Equation (11) is known as the least M-estimate algorithm and can be viewed as a generalization of the LMS algorithm. It becomes identical to the LMS algorithm when noise $e(n)$ is less than a threshold ξ. When the signal error $e(n) > \xi$, $q[e(n)]$ in (11) decreases and reaches 0 when $e(n) > \Delta_2$. Thus, the least M-estimate algorithm is capable of reducing the effect of large signal error during the updating process [17].

5. INTRAUTERINE ACOUSTICS EMBEDDED ACTIVE NOISE CONTROLLER

This section develops an algorithm that can integrate the "comfort" audio with the existing ANC system, and provide an environment that is capable of improving the health of the infant by masking the undesired residual noise. The comfort audio used is a combination of maternal heartbeat and other intrauterine sounds [12]. Research has proven that playing womb sound to infant in incubator showed significant benefit in the respiration rate, sleep cycle, and oxygen saturation [11]. Unfortunately, there are two main issues with the integration of audio to the ANC system need to be considered: first, the audio signal can act as interference to the ANC system and impede proper adaptation; and second, the ANC system can cancel the intended soothing sound. Hence, a method must be devised to subtract the audio from error signal before it is used to update the

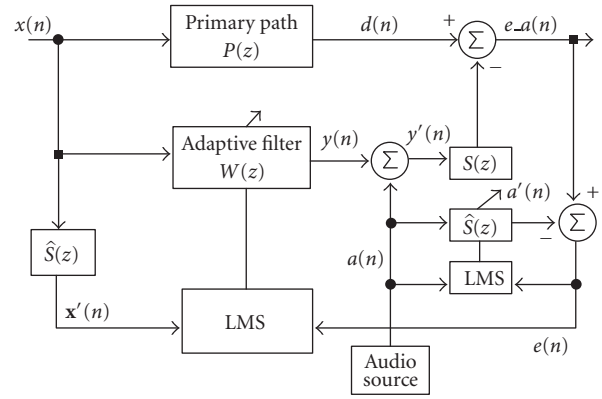

Figure 8: Block diagram of the audio-integrated ANC system.

coefficients of the adaptive filter [20]. The block diagram of the audio integration algorithm is shown in Figure 8. The soothing audio $a(n)$ is added to $y(n)$ and can be heard by the infant inside the incubator.

At the acoustic summing junction, the antinoise $y'(n)$ and the primary noise $d(n)$ are combined to produce the residual error $e\_a(n)$. It contains the true error (residual noise) $e(n)$ and the component of audio. Therefore, by subtracting the audio from the residual error $e\_a(n)$, we can get the true error, then the true error is used to update the weight vector of the adaptive filter $W(z)$. It should be noted that the audio signal passed the secondary path, and filtered by $S(z)$, then it is subtracted. The z transform of residual error $e\_a(n)$ can be expressed as [21]

$$E\_A(z) = D(z) - S(z)[Y(z) + A(z)]. \tag{12}$$

The adaptive filter $\hat{S}(z)$ is used to cancel the audio interference on the performance of $W(z)$. This filter generates

$$E(z) = E\_A(z) + \hat{S}(z)A(z). \tag{13}$$

Then we can get the following equation by substituting (12) into (13):

$$E(z) = D(z) - S(z)Y(z). \tag{14}$$

We assume that $S(z) = \hat{S}(z)$ and the audio is uncorrelated with the primary noise. Then (13) can be expressed in time domain as

$$e(n) = d(n) - [y(n) * s(n)] \tag{15}$$

which is the true error used to update $W(z)$ by using the FXLMS system.

The main advantage of this algorithm lies in its ability to model the secondary path online. This involves the estimation of the secondary path in parallel with the operation of the ANC system. The $S(z)$ filter is modeled through a system identification scheme. It uses soothing audio as the reference signal and treats the secondary path as the unknown system. This makes the algorithm sensitive to time-varying secondary paths.

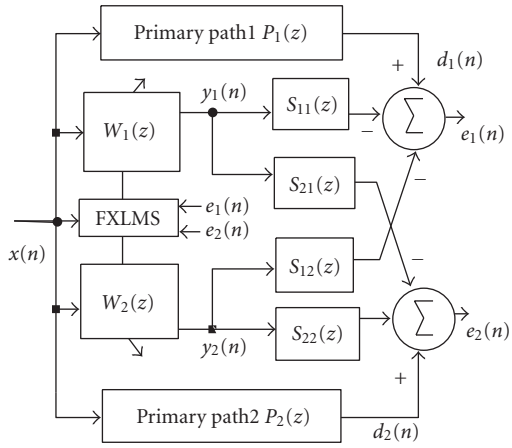

Figure 9: Block Diagram of the $1 \times 2 \times 2$ FXLMS algorithm.

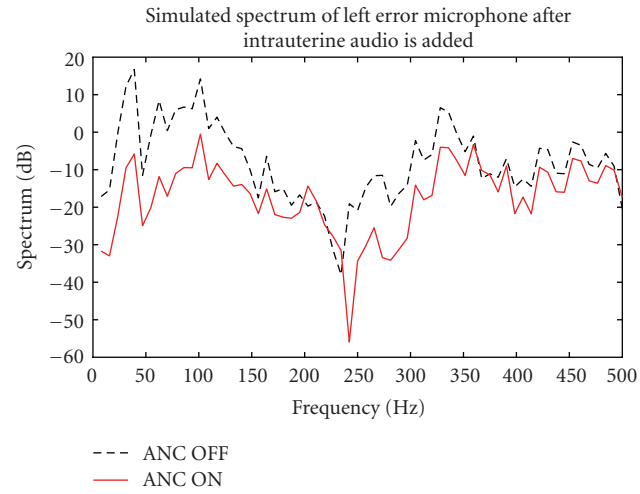

Figure 10: Simulated spectra at left error microphone before (ANC OFF) and after (ANC ON) active noise control.

The key advantages of the intrauterine acoustic embedded ANC system can be summarized as follows. (i) It re-establishes pre-natal ambience thus fostering infant health. (ii) The secondary path is modeled online making the system more receptive to changes in the environment. (iii) It is successful in masking residual error and in preventing the audio from interfering with the updation. (iv) The audio integration does not require supplementary hardware, existing speakers and power amplifier of the ANC system can be used making it cost effective.

6. SIMULATION AND EXPERIMENT RESULTS

6.1. Multichannel FXLMS algorithm

In the previous sections, we described the single channel ANC system. In this section, an example of multichannel ANC system, $1 \times 2 \times 2$ FXLMS algorithm is used for real experiment. Figure 9 shows the multichannel feedforward ANC system using the $1 \times 2 \times 2$ FXLMS algorithm. In this system, two secondary speakers and two error microphones are used independently. These two error microphones pick up the residual errors $e_1(n)$ and $e_2(n)$ at different positions, thus able to form two individual quiet zones centered at the error microphones. The ANC algorithm used two adaptive filters $W_1(z)$ and $W_2(z)$ to generate antinoise $y_1(n)$ and $y_2(n)$ to drive the two independent secondary speakers. In Figure 9, $d_1(n)$ and $d_2(n)$ are the primary noises to be cancelled, $S_{11}(z)$, $S_{12}(z)$, $S_{21}(z)$, and $S_{22}(z)$ are the secondary path transfer functions, and $P_1(z)$ and $P_2(z)$ are the primary path transfer functions.

The multichannel FXLMS algorithm is summarized as follows:

$$y_i(n) = \mathbf{w}_i^T(n)\mathbf{x}(n), \quad i = 1, 2,$$

$$\mathbf{w}_i(n+1) = \mathbf{w}_i(n) + \mu_i\left[e_i(n)\mathbf{x}(n) * \hat{s}_{i1}(n) + e_i(n)\mathbf{x}(n) * \hat{s}_{i2}(n)\right], \quad i = 1, 2, \tag{16}$$

where $\mathbf{w}_1(n)$ and $\mathbf{w}_2(n)$ are weight vectors of the adaptive filters $W_1(z)$ and $W_2(z)$, respectively, μ_1 and μ_2 are the step sizes, $\hat{s}_{11}(n)$, $\hat{s}_{12}(n)$, $\hat{s}_{21}(n)$, and $\hat{s}_{22}(n)$ are the impulse responses of $\hat{S}_{11}(z)$, $\hat{S}_{12}(z)$, $\hat{S}_{21}(z)$, and $\hat{S}_{22}(z)$, respectively.

Similar to the multichannel ANC system (as shown in Figure 9), we extended the single-channel audio-integrated ANC system (as shown in Figure 8) into a $1 \times 2 \times 2$ multichanel system. In this multichannel intrauterine acoustics embedded ANC system, the two adaptive filters $W_1(z)$ and $W_2(z)$ are used to update the two antinoise $y_1(n)$ and $y_2(n)$.

6.2. Simulation results

To evaluate the performance of the innovative intrauterine acoustic embedded ANC, we investigate the noise cancellation achievement through simulation and real time experiment.

In the simulation, we apply the intrauterine acoustics embedded ANC system described in Section 6.1. The input reference noise is taken from an incubator noise audio file at first. The ANC system is simulated with measured $P_1(z)$, $P_2(z)$, $S_{11}(z)$, $S_{12}(z)$, $S_{21}(z)$, and $S_{22}(z)$. A 60-tap filter with step size of 0.1 is used for the adaptive noise cancellation filter $W_1(z)$ and $W_2(z)$. The residual noise is found to be 16 dB lower than the input on average. The plots illustrating the spectra of noise before (ANC OFF) and after (ANC ON) cancellation at left error microphone and right error microphone after assigning intrauterine audio are shown in Figures 10 and 11.

To demonstrate the impulse noise suppress by nonlinear algorithms, the noise signal is interspersed with high-amplitude random impulses (30 dB higher than background). The impulses are at time $n = 40000$, 52000, and 64000 and last for a length of 100 samples. The FXLMM algorithm was implemented for the audio-integrated ANC

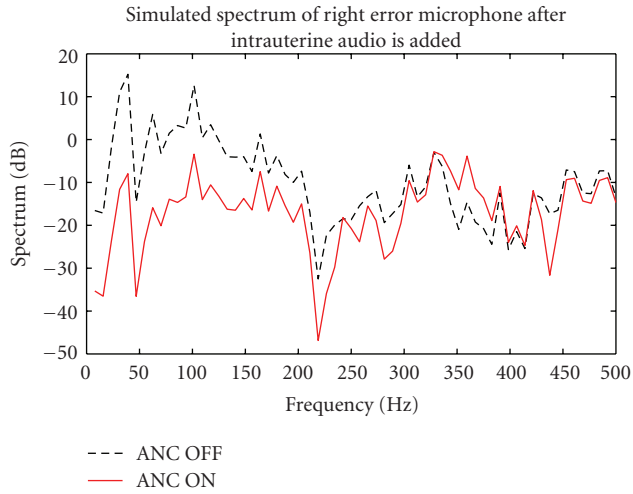

Figure 11: Simulated spectra at right error microphone before (ANC OFF) and after (ANC ON) active noise control.

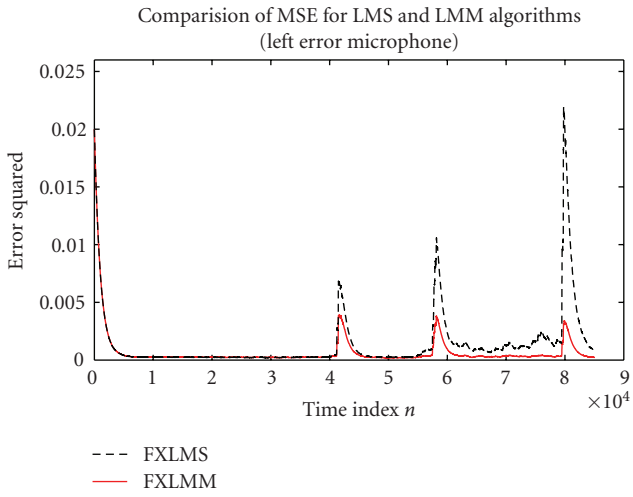

Figure 12: Learning curves at left error microphone for the FXLMS and FXLMM algorithms ($\mu = 0.0007$, impulse occurred at $n = 40000$, 62000, and 64000).

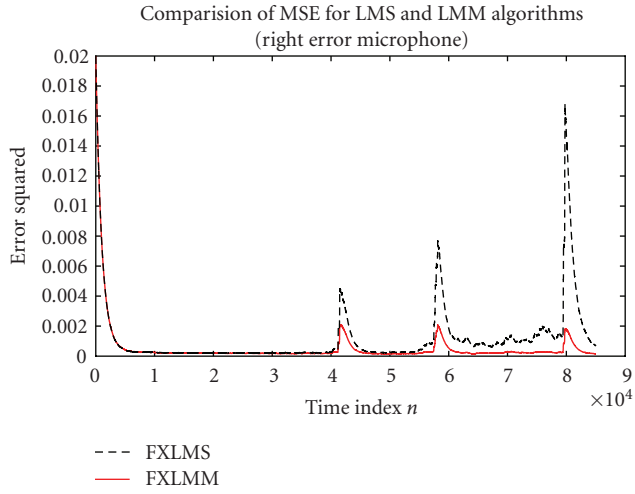

Figure 13: Learning curves at right error microphone for the FXLMS and FXLMM algorithms ($\mu = 0.0007$, impulse occurred at $n = 40000$, 62000, and 64000).

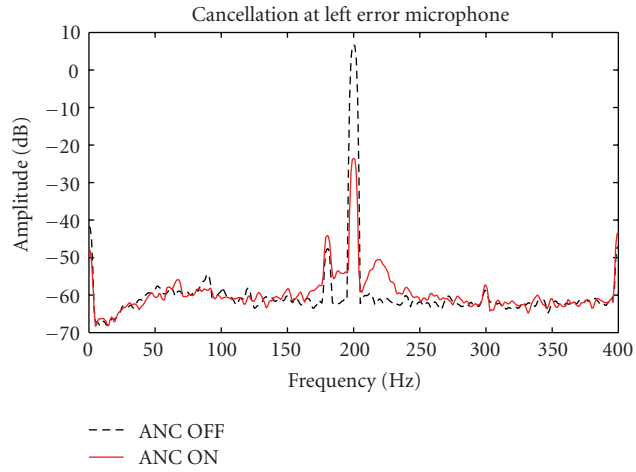

Figure 14: Real-time noise cancellation at left error microphone in the incubator.

system. The probabilities θ_ξ, θ_{Δ_1}, and θ_{Δ_2} for determining the threshold were taken to be 0.05, 0.025, and 0.005, respectively, for 95%, 97.5%, and 99.5% confidence that the error vector was in the interval $[0, \xi]$, $[0, \Delta_1]$, and $[0, \Delta_2]$, respectively [17]. A 60-tap adaptive filter with a step size of 0.0007 was implemented. The results of incubator noise cancellation are shown in Figures 12 and 13.

The simulation results show that the FXLMM algorithm behaves in an identical manner to the FXLMS algorithm until before the impulses are encountered. The FXLMS algorithm, however, exhibits a degraded system performance with a very high mean-squared error (MSE) in the presence of impulses. The FXLMM algorithm is found to be more robust while handling impulses. Comparing the MSE plots of the two algorithms shows that the FXLMM algorithm has superior performance in the presence of impulses and is more effective in suppressing the adverse influence of impulse noise.

6.3. *Real-time experiment results*

A real-time experiment is set up as shown in Figure 5 with the real GE Healthcare incubator, we use a 200 Hz sinusoidal signal generated by a loudspeaker as the primary noise (60 dB higher than the background), two antinoise loudspeakers are fixed in the incubator, two error microphones are placed near baby's ears to pick up the noise residue, the primary microphone is set on the top of the incubator in order to collect the primary noise signal. A TI TMS320C30 DSP is used for the ANC system. The assembly language is used for software developing in order to achieve the real-time processing requirement [22]. For the real-time experiment setup, the sampling frequency is 1.938 KHz, two 220-tap filters with the convergence factor of 0.0003 were used for the adaptive noise cancellation filters $W_1(z)$ and $W_2(z)$.

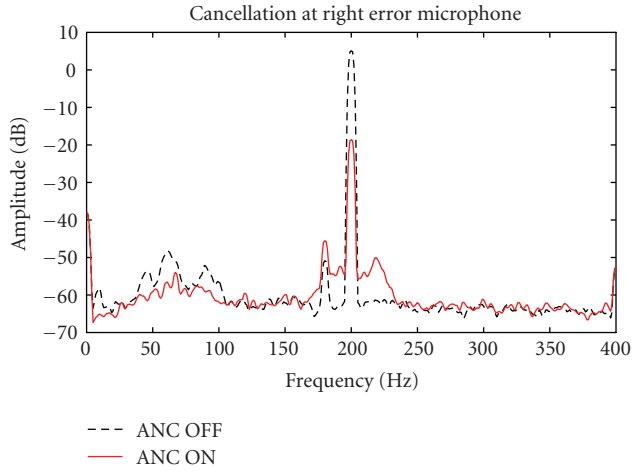

Figure 15: Real time noise cancellation at right error microphone in the incubator.

The real-time noise cancellation results based on the real time experiment are shown in Figures 14 and 15. By comparing the spectra of the noise before and after cancellation, we can find that the residual noises are 30.231 dB lower than the original noise at the left error microphone and 23.685 dB lower at the right error microphone. After the ANC system, the high power noise is dramatically reduced into an acceptable range and not harmful any more.

7. CONCLUSION

In this paper, a novel neonatal healthcare application, the intrauterine acoustics embedded active noise controller, has been presented. The integration algorithm created a beneficial environment for the infant and allowed the residual noise from the ANC system to be masked. The ANC system involved an adaptive method of noise cancellation using the statistically robust FXLMM algorithm. It allowed for stable operation of the ANC system in the presence of impulsive interference in the input. Real transfer functions measured from a laboratory setup were used to develop a computer model for simulation of the ANC system. The integration algorithm was proven to be highly advantageous as it allows the secondary path to be modeled online making the system more sensitive to changes in the environment. The real time controller was found to be cost effective and displayed stable performance in the real incubator.

REFERENCES

[1] G. Healthcare, Incubator the better care by design, http://www.gehealthcare.com/usen/perinatal/micro_environments/giraffe/products/giraffeincubator_fnb.html.

[2] R. A. Etzel, S. J. Balk, C. F. Bearer, M. D. Miller, and K. M. Shea, "Noise: a hazard for the fetus and newborn," *Pediatrics*, vol. 100, no. 4, pp. 724–727, 1997.

[3] P. Bremmer, J. F. Byers, and E. Kiehl, "Noise and the premature infant: physilological effects and practice impications," *Journal of Obstetric, Gynecologic, & Neonatal Nursing*, vol. 32, no. 4, pp. 447–454, 2003.

[4] A. N. Johnson, "Neonatal response to control of noise inside the incubator," *Pediatric Nursing*, vol. 27, no. 6, pp. 600–605, 2001.

[5] P. Thanigai, S. M. Kuo, and R. Yenduri, "Nonlinear active noise control for infant incubators in neo-natal intensive care units," in *Proceedings of the IEEE International Conference on Acoustics, Speech and Signal Processing (ICASSP '07)*, vol. 1, pp. 109–112, Honolulu, Hawaii, USA, April 2007.

[6] P. Thanigai and S. M. Kuo, "Intrauterine acoustic embedded active noise controller," in *Proceedings of the IEEE International Conference on Control Applications (CCA '07)*, pp. 1359–1364, Singapore, October 2007.

[7] G. E. Whitwell, "The importance of prenatal sound and music," http://www.birthpsychology.com/lifebefore/sound1.html.

[8] B. S. Rosner and N. E. Doherty, "The response of neonates to intra uterine sounds," *Developmental Medicine and Child Neurology*, vol. 21, pp. 723–729, 1979.

[9] H. Murooka, Y. Koie, and N. Suda, "Analysis of intrauterine sounds and their tranquilizing effects on the newborn infant," *Journal de Gynecologie, Obstetrique et Biologie de la Reproduction*, vol. 5, pp. 367–376, 1976.

[10] J. D. Tulloch, H. L. Jacobs, D. G. Prugh, and W. A. Greene, "Normal heartbeat sound and the behavior of newborn infants—a replication study," *Psychosomatic Medicine*, vol. 26, no. 6, pp. 661–670, 1964.

[11] J. M. Standley, "A meta-analysis of the efficacy of music therapy for premature infants," *Journal of Pediatric Nursing*, vol. 17, no. 2, pp. 107–113, 2002.

[12] The miracle baby sleep system, http://www.babysleepsystem.com/index.htm.

[13] W. B. Carvalho, M. L. G. Pedreira, and M. A. L. de Aguiar, "Noise level in a pediatric intensive care unit," *Jornal de Pediatria*, vol. 81, no. 6, pp. 485–498, 2005.

[14] S. M. Kuo and D. R. Morgan, "Active noise control: a tutorial review," *Proceedings of the IEEE*, vol. 87, no. 6, pp. 943–973, 1999.

[15] S. M. Kuo and D. R. Morgan, *Active Noise Control Systems Algorithms and DSP Implementations*, John Wiley & Sons, New York, NY, USA, 1996.

[16] P. J. Rousseeuw and A. M. Leroy, *Robust Regression and Outlier Detection*, John Wiley & Sons, New York, NY, USA, 1987.

[17] Y. Zou, S.-C. Chan, and T.-S. Ng, "Least mean M-estimate algorithms for robust adaptive filtering in impulse noise," *IEEE Transactions on Circuits and Systems II*, vol. 47, no. 12, pp. 1564–1569, 2000.

[18] Y. Zou, S.-C. Chan, and T.-S. Ng, "A robust M-estimate adaptive filter for impulse noise suppression," in *Proceedings of the IEEE International Conference on Acoustics, Speech, and Signal Processing (ICASSP '99)*, vol. 4, pp. 1765–1768, Phoenix, Ariz, USA, May 1999.

[19] S.-C. Chan and Y.-X. Zou, "A recursive least M-estimate algorithm for robust adaptive filtering in impulsive noise: fast algorithm and convergence performance analysis," *IEEE Transactions on Signal Processing*, vol. 52, no. 4, pp. 975–991, 2004.

[20] M. Zhang, H. Lan, and W. Ser, "A robust online secondary path modeling method with auxiliary noise power scheduling strategy and norm constraint manipulation," *IEEE Transactions on Speech and Audio Processing*, vol. 11, no. 1, pp. 45–53, 2003.

[21] W. S. Gan and S. M. Kuo, "An integrated audio and active noise control headsets," *IEEE Transactions on Consumer Electronics*, vol. 48, no. 2, pp. 242–247, 2002.

[22] S. M. Kuo, B. H. Lee, and W. Tian, *Real-Time Digital Signal Processing Implementations and Applications*, John Wiley & Sons, Hoboken, NJ, USA, 2006.

Hindawi Publishing Corporation
Advances in Acoustics and Vibration
Volume 2008, Article ID 869130, 9 pages
doi:10.1155/2008/869130

Research Article

Integration of Bass Enhancement and Active Noise Control System in Automobile Cabin

Liang Wang,[1] Woon Seng Gan,[1] and Sen M. Kuo[2]

[1] *School of Electrical and Electronic Engineering, College of Engineering, Nanyang Technological University, Nanyang Avenue, Singapore 639798*
[2] *Department of Electrical Engineering, Northern Illinois University, DeKalb, IL 60115, USA*

Correspondence should be addressed to Liang Wang, wang0136@ntu.edu.sg

Received 29 December 2007; Accepted 5 March 2008

Recommended by Marek Pawelczyk

With the advancement of digital signal processing technologies, consumers are more concerned with the quality of multimedia entertainment in automobiles. In order to meet this demand, an audio enhancement system is needed to improve bass reproduction and cancel engine noise in the cabins. This paper presents an integrated active noise control system that is based on frequency-sampling filters to track and extract the bass information from the audio signal, and a multifrequency active noise equalizer to tune the low-frequency engine harmonics to enhance the bass reproduction. In the noise cancellation mode, a maximum of 3 dB bass enhancement can be achieved with significant noise suppression, while higher bass enhancement can be achieved in the bass enhance mode. The results show that the proposed system is effective for solving both the bass audio reproduction and the noise control problems in automobile cabins.

1. INTRODUCTION

Noise control and the high-quality bass reproduction in automobile cabins are two interrelated problems. The later can be difficult due to the high-level noise present and the size of the loudspeakers that can be installed inside the cars. Traditional passive noise control techniques are only efficient at high frequencies. For the low-frequency engine noises, passive techniques become costly and bulky, which are not suitable for the use in automobile cabins. Due to its effectiveness in reducing low-frequency noise, the active noise control (ANC) [1] technique has received much attention since 1980s [2, 3].

On the other hand, with the advancement of multimedia digital signal processing (DSP) technologies, high-quality audio reproduction is becoming possible for the automobiles. However, there are many challenges in reproducing high-quality bass in cars due to the limited space and acoustic properties, and the low-frequency noise present in the cabins.

The ANC techniques generally produce good performance in canceling the narrowband engine noise. However, it does not offer complete control over the engine noise in cabins. In some practical applications, it prefers to enhance some preselected noise components to extract important sound information. For example, the driver may want to know how the engine is working when driving. Due to its flexibility of amplifying or attenuating noises with predetermined levels at certain frequencies, active noise equalizer (ANE) [4] systems and other similar algorithms [5–7] have potential applications.

High-quality audio reproduction in cabins can be difficult due to the engine noise and low-frequency performance of the loudspeakers. With the flexibility of ANE system, we propose a novel method to solve this problem. Instead of trying to cancel the engine noise entirely, the proposed integrated system equalizes the engine-noise harmonics based on the bass information to enhance the low- frequency part of audio signal. The main challenges are to track the frequencies of engine harmonics and to tune these harmonics to match the bass components of audio signal.In order to integrate active noise control with bass enhancement, the proposed system uses frequency-sampling filter (FSF) [8] and multifrequency ANE [4] to tune the engine harmonics, and convert the annoying low-frequency noise into desired audio bass components.

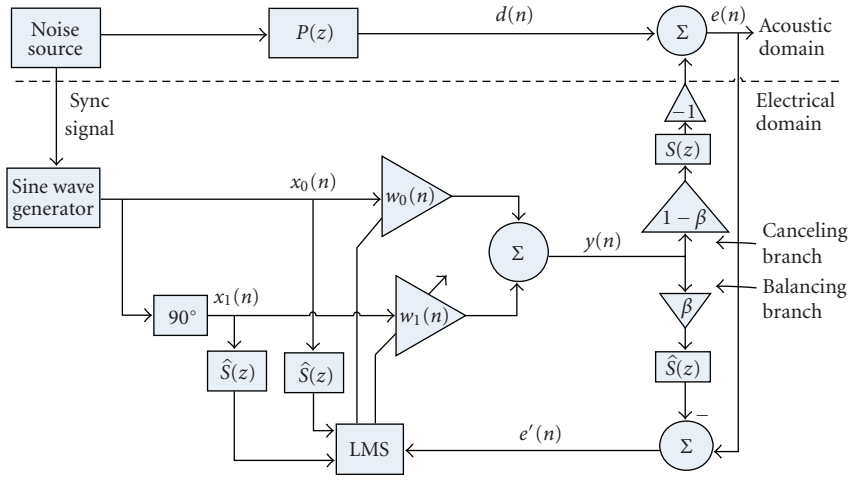

Figure 1: Block diagram of single-frequency ANE system.

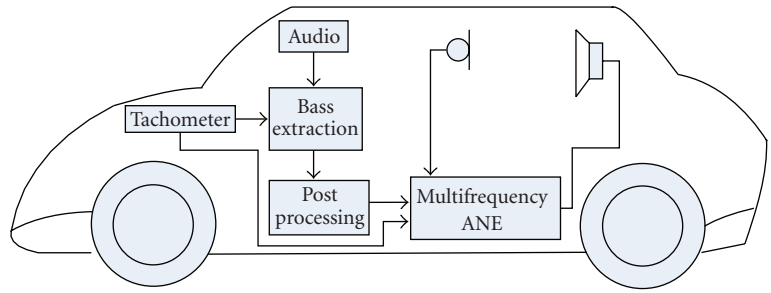

Figure 2: System block diagram inside the automobile cabin.

The remainder of this paper is structured as follows. Section 2 presents the narrowband ANE system, followed by a description of the proposed system in Section 3. Simulation results under different driving conditions are given in Section 4, and Section 5 concludes this paper.

2. NARROWBAND ACTIVE NOISE EQUALIZER

The single-frequency narrowband ANE [4] system is based on an adaptive notch filter using the filtered-X least mean square (FXLMS) [1] algorithm. As shown in Figure 1, the secondary output is split into two branches: the canceling branch and the balancing branch. A pseudoerror $e'(n)$ is used to trick the adaptive filter to converge to a desirable state determined by the user. The pseudoerror can be expressed as

$$e'(n) = d(n) - y(n)^* s(n). \tag{1}$$

After convergence, the pseudoerror approaches zero. However, the actual residual noise $e(n)$ converges to

$$e(n) = d(n) - (1-\beta)y(n)^* s(n) \approx \beta d(n), \tag{2}$$

where β is known as the gain factor determined by the user.

Depending on the gain factor β, ANE can be classified into four operation modes [4]:

(i) cancellation mode ($\beta = 0$): ANE functions as the conventional narrowband ANC;

(ii) attenuation mode ($0 < \beta < 1$): the amount of attenuation is determined by β. Therefore, it is possible to retain some portion of the noise at the selected frequency;

(iii) neutral mode ($\beta = 1$): the noise passes through the ANE system without attenuation;

(iv) enhancement mode ($\beta > 1$): the ANE functions as an amplifier that enhances the noise component with amount determined by β.

3. PROPOSED SYSTEM IN AUTOMOBILE CABINS

A proposed system in car cabins that integrates bass enhancement and active noise equalizer is shown in Figure 2. This system can be divided into three subsystems: (i) the "bass extraction" block extracts bass components from the car audio system based on the engine speed; (ii) the "postprocessing" block processes; these bass components to match with frequencies of engine harmonics; and (iii) the "multifrequency ANE" block implements a multifrequency ANE that enhances desired low-frequency audio components using equalized engine harmonics. A detailed overview of these subsystems is described as follows.

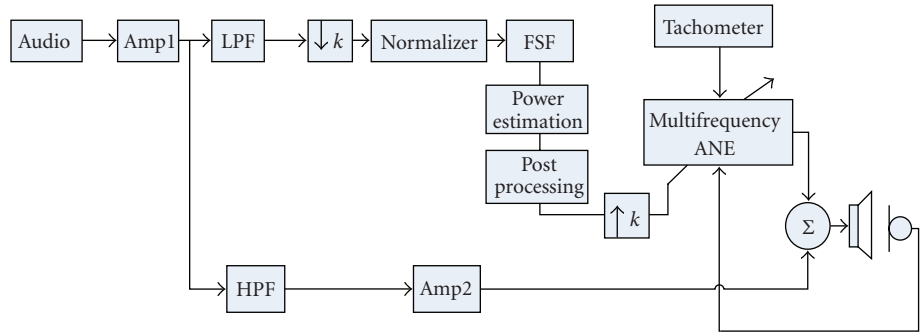

Figure 3: Audio signal extraction block diagram.

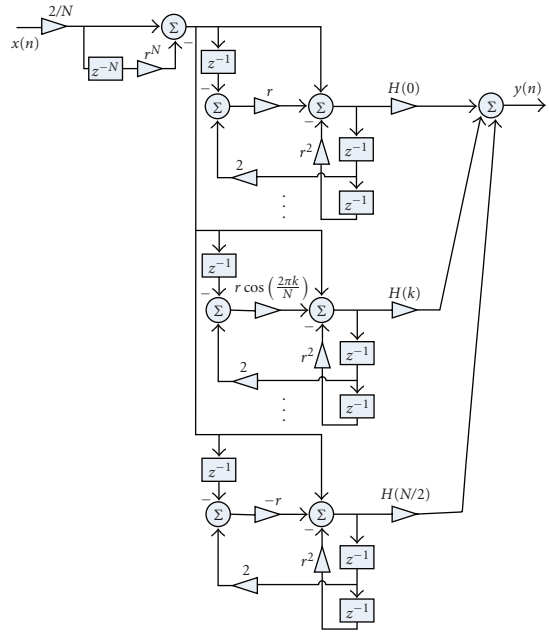

Figure 4: Frequency-sampling filter block diagram.

3.1. Bass extraction

The audio signal components that will be enhanced are those close to the engine-noise components, which are related to the engine revolutions per minute (RPM). Because the engine RPM is time varying, the engine-noise components change accordingly, thus the filters must self-configure according to the engine RPM to extract the desired audio signal components. In other words, the filter's center frequency should be tuned by the engine RPM.

As shown in Figure 3, the audio signal is passed through a low pass filter with a cutoff frequency at 500 Hz, and the audio signal is decimated to a lower sampling frequency of 1.5 kHz. Therefore, a lower computational load is achieved for processing bass information of the audio signal.

To utilize engine noise for enhancing bass reproduction, extraction of the audio signal at frequencies of engine harmonics is needed. This requires a bank of passband filters align with predominant engine harmonics. Fast online reconfiguration and computational efficiency are important considerations for designing the filter bank. The FSF is chosen to meet these requirements. It is based on sampling a desired amplitude spectrum to obtain the corresponding filter coefficients. The number of FSF channels equals to the number of predominant engine-noise harmonics, where each channel corresponds to one engine harmonic. As shown in Figure 4, the unique characteristic of the FSF structure allows recursive implementation of finite-impulse response filters, leading to both computational efficiency and fast online reconfiguration. The transfer function of the FSF is expressed as

$$H(z) = \frac{2}{N}\left(1 - r^L z^{-N}\right)\sum_{k \le N/2} (-1)^k H(k) \frac{1 - r\cos(2\pi k/N) z^{-1}}{1 - 2r\cos(2\pi k/N) z^{-1} + r^2 z^{-2}}, \quad (3)$$

where N is the filter length, $H(k)$ is frequency sample value at channel k, and r is a radius of pole that is slightly less than unity. Equation (3) shows that the FSF has N parallel bandpass filters with center frequencies at $2\pi k/N$, where $k = 0, 1, \ldots, N-1$. Therefore, the parameter N controls center frequencies of all bandpass filters. The following sections further describe how to design an FSF for a particular engine.

3.1.1. Engine RPM and the fundamental frequency of engine noise

This section investigates the fundamental and firing frequencies of a 4-stroke engine. A sampling frequency of 1.5 kHz is selected for the FSF processing block. This sampling frequency restricts the range of engine noise to 600 Hz. For a 4-stroke engine, the fundamental frequency is the product of the firing frequency and number of the cylinders, where the firing frequency is

$$\text{firing frequency} = \frac{1}{2} \times \frac{\text{RPM}}{60} \text{ Hz}. \quad (4)$$

The fundamental frequency of engine noise is the fourth harmonic of the firing frequency. Depending on the engine noise profile, the harmonics selected can be different. When higher frequency harmonics are selected, this range will be

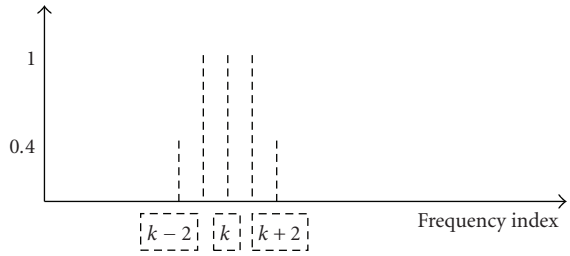

Figure 5: Diagram of FSF filter setting for fundamental engine noise frequency.

lowered accordingly. For most cars and with the objective of bass enhancement, the sampling frequency of 1.5 kHz is reasonable.

3.1.2. Parametric factor

There are two methods in determining the main parameters to control the filtering and center frequencies of FSF. One is to set the filter length N as a constant value and change each of the frequency sample values $H(k)$. However, this approach requires changing multiple sample values during online filter reconfiguration. On the other hand, if we first set the relative frequency samples at certain values, it is possible to achieve the reconfiguration by changing only the FSF filter length N. For example, when we set the filter $H(k)$ at $k = 10$ to coincide with the fundamental frequency of noise, the filter length can be derived as

$$\frac{\text{Fs}}{N} \times 10 = \frac{1}{2} \times \frac{\text{RPM}}{60} \times 4 \Longrightarrow N = \left[\frac{\text{Fs} \times 10 \times 30}{\text{RPM}}\right]. \quad (5)$$

When the RPM is 2500, the corresponding filter length is 180. It is also important to point out that the FSF does not incur a higher computational load when the filter length increases. This is because most frequency samples $H(k)$ are zero and only few frequency samples defined in the passband require computation.

3.1.3. Transition band sample value

Rabiner et al. proposed some typical values for the coefficients in the transition band [9]. In the case of designing the FSF for handling typical RPM from 1000 to 2500, the filter length ranges from 180 to 450. If three samples are used to define the frequency samples in the passband, the optimum value for transition band is found to be 0.4 [10] The illustration is shown in Figure 5.

3.1.4. Selecting suitable filter length/frequency resolution

As the sampling frequency Fs is 1500 Hz, the frequency resolution for FSF is Fs/N. According to the relationship:

$$\frac{\text{Fs}}{N} \times k = \frac{1}{2} \times \frac{\text{RPM}}{60} \times 4, \quad (6)$$

where k is the sample index that is selected to align at the engine noise frequency. As a result, index k controls the resolution of the filter. Therefore, the optimal resolution is determined by the frequency range of the engine noise. Offline calibration is required for different engines to select the proper value of k, which is set to the center frequency of fundamental engine noise, and correspondingly determine the frequency resolution.

3.2. Postprocessing

The signal power estimation is performed before sending to postprocessing block. The process can be expressed as

$$P_x(n) = \lambda P_x(n-1) + (1-\lambda)x^2(n), \quad (7)$$

where $P_x(n)$ is the signal power, $x(n)$ is the current sample, and λ is known as the smoothing parameter or forgetting factor, typically set between 0.9 to 0.999. There are many options for the postprocessing block. Users can perform different kinds of equalization. This paper proposes two schemes. The bass enhancement scheme is designed for higher amplification of equalized engine noise, and the noise cancellation scheme is designed for more engine noise reduction.

3.2.1. Bass enhancement scheme

The bass enhancement scheme emphasizes on the enhancement of bass components in the audio signal. Using the power estimation results obtained from previous block, the gain factors β_i, $i = 1, 2, \ldots, Ns$ in the ANE systems can be the calculated as

$$\beta_i = \sqrt{P_i} \times \alpha, \quad i = 1, 2, \ldots, Ns, \quad (8)$$

where P_i is the power of the FSF's output that corresponding to the engine harmonic frequency, and α is a constant that controls the volume of the sound in order to mix the tuned engine noise with the original audio output. Users can tune α to different levels of bass enhancement. The variable Ns is the number of predominant engine noise harmonics which is dependent on the particular engine type. If the in cabin loudspeakers are incapable in reproducing the signal at engine noise fundamental frequency, the perception of bass can still be enhanced by other harmonics due to the famous "missing fundamental" phenomenon.

In order to set the value of α that determines β_i, it is important to derive the relationship between the sound pressure level of the audio signal and engine noise. In typical audio system, the sound pressure level ranges from 50 dB to 80 dB. On the other hand, the engine noise level in a cabin ranges from 45 dB to 75 dB [9]. For a 16-bit audio signal, which is normalized to unit, the sound pressure level is stated as

$$\text{SPL}_A = 96\,\text{dB} + 10\log_{10}x^2(n)\,\text{dB}. \quad (9)$$

This equation sets the maximum sound pressure level SPL_A to 96 dB when the amplitude of $x(n)$ equals to 1.

To calibrate the value of factor α, it is assumed that if the signal SPL_A is 60 dB, the engine noise should be neither

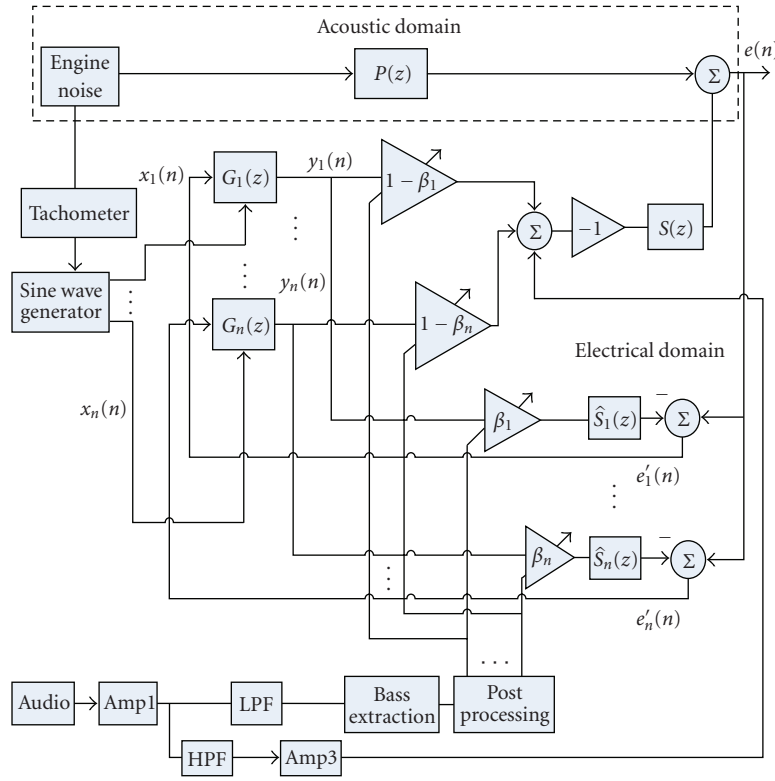

Figure 6: System block diagram of the multifrequency ANE.

amplified nor attenuated. According to (9) and setting SPL_A to 60 dB, the amplitude of the signal is computed as

$$A_A = 10^{(\mathrm{SPL}_A - 96)/20} \approx 0.016. \tag{10}$$

The power of the signal is approximately 1.28×10^{-4}. Setting β to 1 results in $\alpha \approx 88$.

3.2.2. Noise cancellation scheme

It can be seen from the previous scheme that by tuning the factor α, higher enhancement at the low frequency can be achieved. However, at the same time, the timbre of the original signal will also change. To fulfill the needs of enhancing bass reproduction while maintaining a balanced timbre with significant noise cancellation, we propose another scheme known as the noise cancellation scheme.

In this scheme, when engine noise is louder than the audio signal, a proper equalized engine noise is used to enhance the audio signal. In order to maintain a better timber, this scheme does not allow any amplification of the engine noise, or the gain factors for engine noise harmonics should be always smaller than one. The rationale behind this scheme is to make the amplitude of the engine harmonics equals to the corresponding amplitude of the audio signal at that frequency. In this way, when there is audio signal present at the engine noise harmonics, the ANE system amplifies the amplitude of the engine noise to produce a 3 dB enhancement of audio signal.

When the engine noise is lower than the audio signal, we keep or cancel the engine noise harmonics depending on whether the audio signal is present or not. As a result, the gain factor for the ANE system is either one or zero. The maximum gain of 3 dB is achieved when the engine noise level equals the audio signal level. Therefore, to achieve the desired gain adjustment in Section 2, a new gain scheme is proposed as follows:

$$\beta = \begin{cases} e^{(\mathrm{SPL}_A - \mathrm{SPL}_E)/\gamma}, & \mathrm{SPL}_O < \mathrm{SPL}_A < \mathrm{SPL}_E, \\ 1, & \mathrm{SPL}_O < \mathrm{SPL}_E < \mathrm{SPL}_A, \\ 0, & \mathrm{SPL}_A < \mathrm{SPL}_O, \end{cases} \tag{11}$$

where SPL_A is the sound pressure level of audio at the corresponding engine noise harmonic frequency, SPL_E is the sound pressure level of the engine noise harmonic, SPL_O is used as a threshold and is set to 45 dB, and γ is a constant governing the equalization between the gain factor and difference between the sound pressure level of audio signal and engine noise.

To equalize the engine noise when $\mathrm{SPL}_O < \mathrm{SPL}_A < \mathrm{SPL}_E$, the gain factor β is chosen such that

$$\beta A_E = A_A, \tag{12}$$

where A_E is the amplitude of the engine noise and A_A is the amplitude of the audio signal. Substituting (9) and (11) into

(12), we have

$$A_E e^{(\mathrm{SPL}_A - \mathrm{SPL}_E)/\gamma} = A_A,$$
$$e^{(\mathrm{SPL}_A - \mathrm{SPL}_E)/\gamma} = \frac{10^{(\mathrm{SPL}_A - 96)/20}}{10^{(\mathrm{SPL}_E - 96)/20}}. \quad (13)$$

Taking logarithm of both sides, we obtain

$$\left(\frac{\mathrm{SPL}_A - \mathrm{SPL}_E}{\gamma}\right)\log_{10} e = \frac{\mathrm{SPL}_A - 96}{20} - \frac{\mathrm{SPL}_E - 96}{20}. \quad (14)$$

This results in

$$\frac{\log_{10} e}{\gamma} = \frac{1}{20}, \quad (15)$$

and $\gamma \approx 8.6859$.

According to this gain factor scheme under a loud engine noise condition, it is expected to achieve both reduction of engine noise and a 3 dB bass enhancement at certain frequencies.

3.3. Multifrequency ANE system

To perform the active control of the engine noise, we designed a multifrequency ANE system consisting of several independent single-frequency ANE systems connected in parallel. Each single-frequency ANE is tuned to the corresponding harmonic frequency of the engine noise. The overall block diagram of the multichannel ANE is shown in Figure 6. The number of the single-frequency ANE system is determined by the number of the selected predominant engine noise harmonics. Each ANE block has its own gain factor tuned to the power of the related audio component. When the audio signal is changing with time, the equalization of the low-frequency signal responds accordingly.

4. SIMULATION RESULTS

Performance of the proposed system is evaluated by both a synthesized engine noise and a recorded in cabin engine noise (Toyota Crown at passenger seat with the engine running at around 2600 RPM). The reference signal is generated using cosine wave with the center frequency at the corresponding engine noise harmonic. Kim and Park showed in [11] that the self-generated reference could achieve good performance in ANC applications. Figures 7 and 8 show the spectrogram and power distribution of the engine noise, respectively. For this recorded engine noise, we select two predominant frequency components and an FSF is used to extract the bass audio information.

The audio signal used for the simulation is "Hotel California" by The Eagles (live version). The sound clip was taken from the start of the track, which consists of a bass drum with some audience noise. This track makes it easier to focus on the bass. The sound clip and simulation results wave files are available at [12].

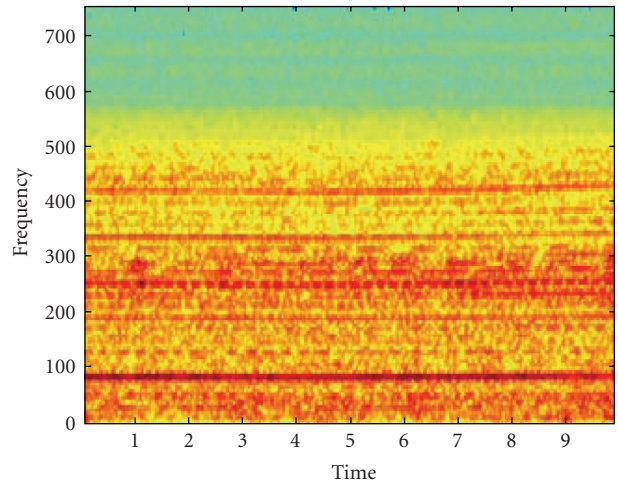

Figure 7: Spectrogram of the recorded engine noise.

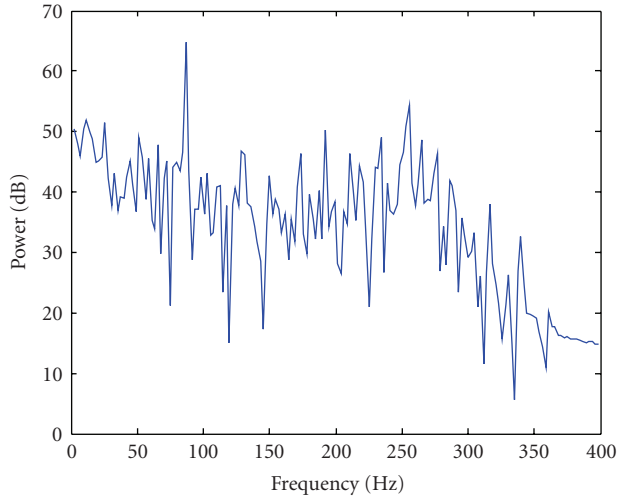

Figure 8: Power distribution of the recorded engine noise.

4.1. Bass enhancement scheme

The results shown in Figures 9 and 10 are the spectrograms that show bass components of audio signal before and after the process, respectively. The predominant engine noise harmonics are attenuated (marked as circles in diagrams) when the audio is absent, and tuned according to the gain factor shown in Figure 11, when the audio is present.

To display the tuned engine noise more clearly, the spectrogram of the tuned engine noise is shown in Figure 12. It is observed that the tuned engine noise has a similar spectrogram distribution as the audio signal.

The proposed system is also evaluated using synthesized engine noise to test the effectiveness at defined harmonics. In the following simulation, the synthesized engine is running at 3000 RPM, with its predominant harmonic frequencies at 100, 200, 300, and 400 Hz. As seen from Figure 13, the engine noise components at 100, 300, and 400 Hz are attenuated by 5, 8, and 15 dB. However, a 3 dB enhancement is achieved at 200 Hz. The equalized engine noise is equalized to enhance

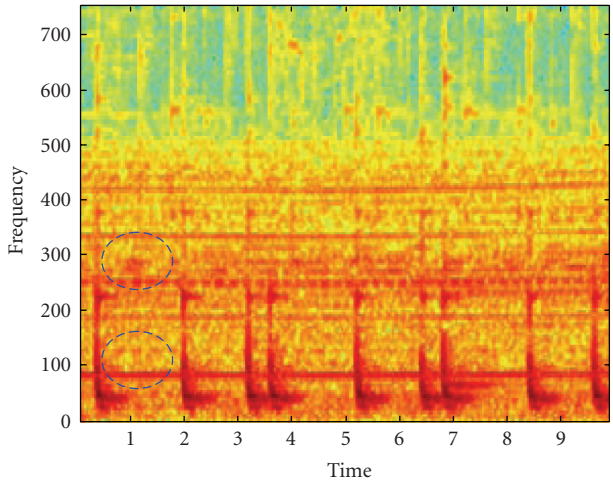

Figure 9: Spectrogram of the sound in cabin when system off.

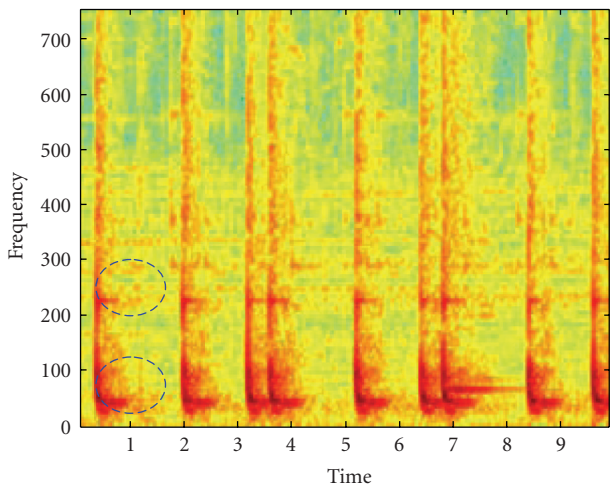

Figure 10: Spectrogram of the sound in cabin when system on.

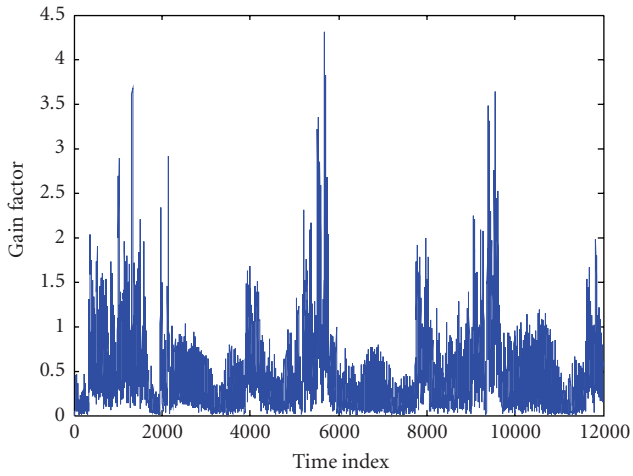

Figure 11: Gain factor for fundamental frequency.

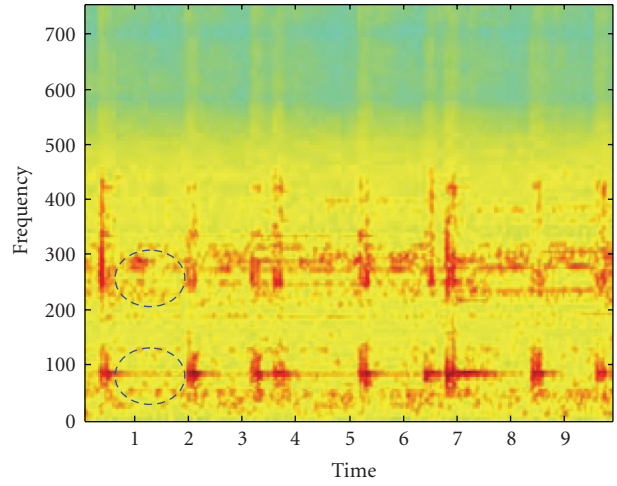

Figure 12: Spectrogram of the tuned noise.

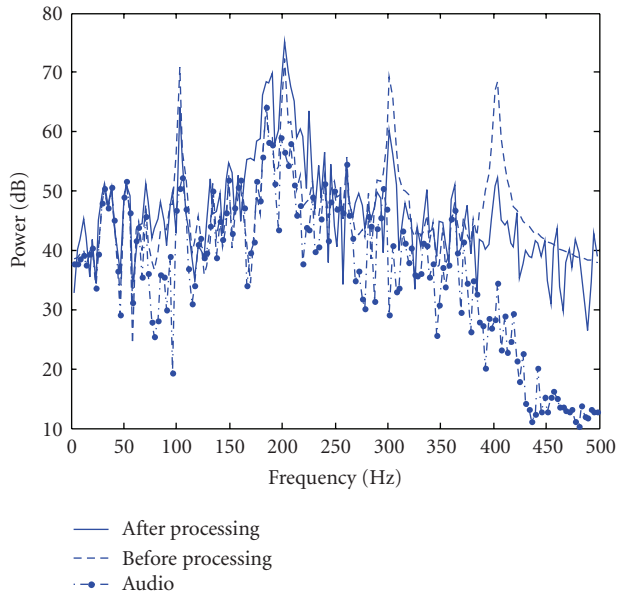

Figure 13: Bass enhancement scheme with synthesized engine noise.

the bass component of the audio signal. The gain factor value for the 200 Hz harmonic over the duration of simulation is shown in Figure 14.

4.2. Noise cancellation scheme

In this simulation, we investigate the performance of the proposed system under noise cancellation scheme. The system is tested with the recorded engine noise (running at 2600 RPM) and with SPL of 75 dB. The spectrogram of this engine noise is similar with those under bass enhancement mode.

The tested audio file is extracted from a short speech clip. We simulate the case when the driver is listening to news or

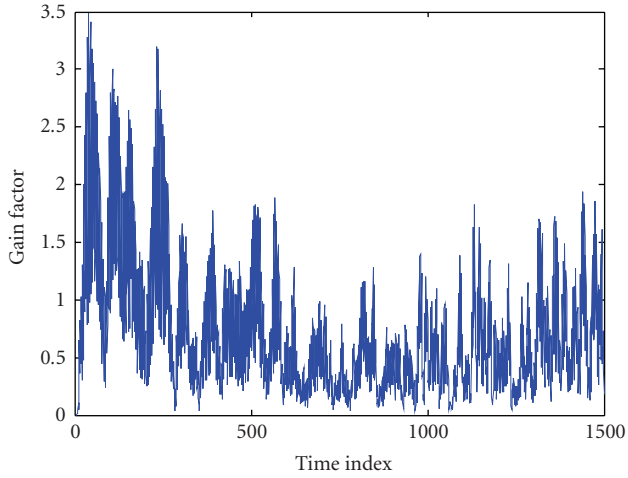

Figure 14: Gain factor (at 200 Hz) in bass enhancement scheme.

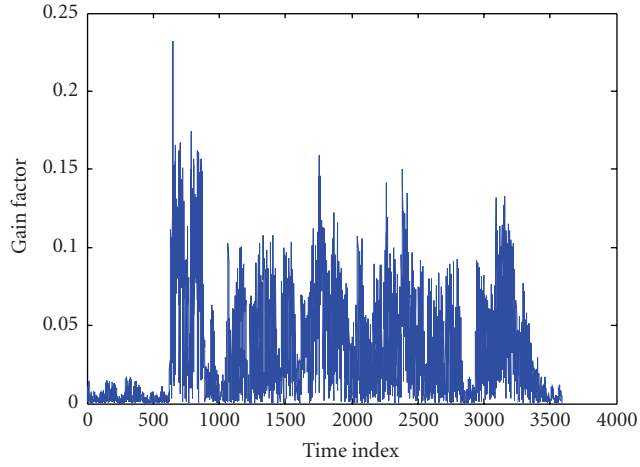

Figure 16: Gain factor using noise cancellation scheme.

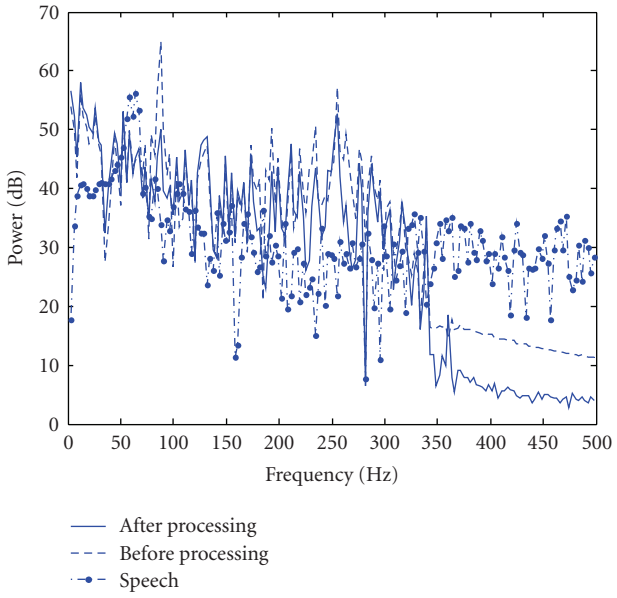

Figure 15: Engine noise before and after processing.

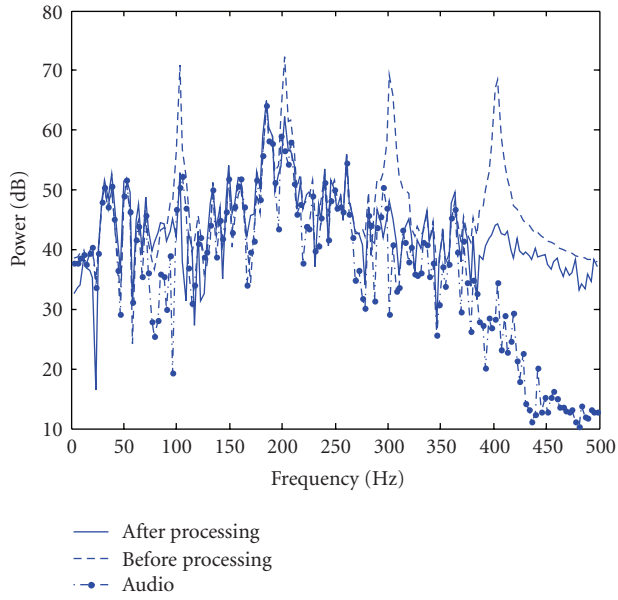

Figure 17: Noise cancellation scheme with synthesized engine noise.

making a phone call. The system adapts to cancel the engine noise to achieve a better SNR for speech perception in the car cabin. Engine noise before and after processing is shown in Figure 15. It can be clearly observed that the most prominent engine noise harmonics are reduced by 6 dB. Gain factor for the fundamental frequency over the period of simulation is shown in Figure 16.

Similar to the bass enhancement scheme, we evaluate the system using audio signal and the synthesized engine noise. As seen from Figure 17, the engine noise components are significantly reduced, especially at 400 Hz since there is very little audio component. The gain factor value for 200 Hz harmonic over the duration of simulation is shown in Figure 18. Compared with the result obtained in bass enhancement scheme, it clearly shows that the gain factor value is confined in the range of 0 to 1, and engine noise is never been amplified.

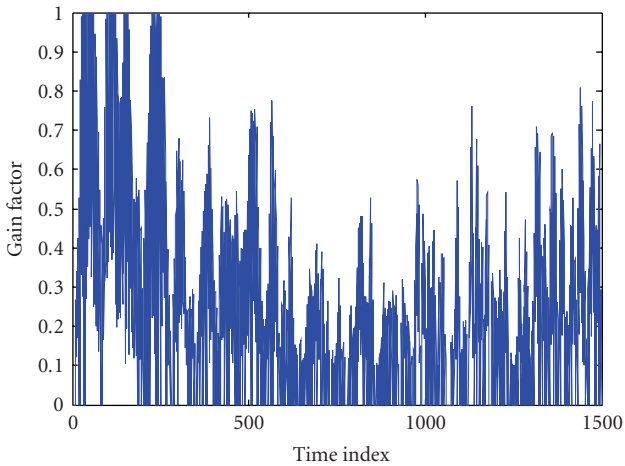

Figure 18: Gain factor (at 200 Hz) in noise cancellation scheme.

5. CONCLUSION

Instead of canceling the engine noise entirely, this paper presented a system that utilizes the engine noise to enhance the bass reproduction of audio signal in automobile cabins. The proposed system integrated bass extraction, audio signal processing, and active noise equalization to enhance desired bass signal and reduce noise. Several engine noises and audio signals are used to evaluate the performance of integrated audio and active noise equalization system. Simulation results showed that the proposed system can achieve audio bass reproduction and noise reduction inside the car cabins.

REFERENCES

[1] S. M. Kuo and D. R. Morgan, *Active Noise Control Systems: Algorithms and DSP Implementations*, John Wiley & Sons, New York, NY, USA, 1996.

[2] M. Vaishya, "Active noise control using a single sensor input," US patent no. 6917687, July, 2005.

[3] H. Sano, T. Inoue, A. Takahashi, K. Terai, and Y. Nakamura, "Active control system for low-frequency road noise combined with an audio system," *IEEE Transactions on Speech and Audio Processing*, vol. 9, no. 7, pp. 755–763, 2001.

[4] S. M. Kuo and M. J. Ji, "Development and analysis of an adaptive noise equalizer," *IEEE Transactions on Speech and Audio Processing*, vol. 3, no. 3, pp. 217–222, 1995.

[5] J. Feng and W. S. Gan, "Adaptive active noise equaliser," *Electronics Letters*, vol. 33, no. 18, pp. 1518–1519, 1997.

[6] L. E. Rees and S. J. Elliott, "Adaptive algorithms for active sound-profiling," *IEEE Transactions on Audio, Speech and Language Processing*, vol. 14, no. 2, pp. 711–719, 2006.

[7] L. Wang, W. S. Gan, Y. K. Chong, and S. M. Kuo, "A novel approach to bass enhancement in automobile cabin," in *Proceedings of IEEE International Conference on Acoustics, Speech and Signal Processing (ICASSP '06)*, vol. 3, pp. 1216–1219, Toulouse, France, May 2006.

[8] S. M. Kuo and B. H. Lee, *Real-Time Digital Signal Processing*, John Wiley & Sons, New York, NY, USA, 2001.

[9] D. J. Thompson and J. Dixon, "Vehicle noise," in *Advanced Applications in Acoustics, Noise and Vibration*, pp. 236–291, Spon Press, London, UK, 2004.

[10] L. R. Rabiner, B. Gold, and C. A. McGonegal, "An approach to the approximation problem for nonrecursive digital filters," *IEEE Transactions on Audio and Electroacoustics*, vol. 18, no. 2, pp. 83–106, 1970.

[11] S. Kim and Y. Park, "On-line fundamental frequency tracking method for harmonic signal and application to ANC," *Journal of Sound and Vibration*, vol. 241, no. 4, pp. 681–691, 2001.

[12] L. Wang, http://eeeweba.ntu.edu.sg/DSPLab/ANE/samples.html.

Hindawi Publishing Corporation
Advances in Acoustics and Vibration
Volume 2008, Article ID 647318, 12 pages
doi:10.1155/2008/647318

Research Article

Optimal and Adaptive Virtual Unidirectional Sound Source in Active Noise Control

Dariusz Bismor

Institute of Automatic Control, Silesian University of Technology, ul. Akademicka 16, 44-100 Gliwice, Poland

Correspondence should be addressed to Dariusz Bismor, dariusz.bismor@polsl.pl

Received 21 November 2007; Revised 22 February 2008; Accepted 5 May 2008

Recommended by Marek Pawelczyk

One of the problems concerned with active noise control is the existence of acoustical feedback between the control value ("active" loudspeaker output) and the reference signal. Various experiments show that such feedback can seriously decrease effects of attenuation or even make the whole ANC system unstable. This paper presents a detailed analysis of one of possible approaches allowing to deal with acoustical feedback, namely, virtual unidirectional sound source. With this method, *two* loudspeakers are used together with control algorithm assuring that the combined behaviour of the pair makes virtual propagation of sound only in one direction. Two different designs are presented for the application of active noise control in an acoustic duct: analytical (leading to fixed controller) and adaptive. The algorithm effectiveness in simulations and real experiments for both solutions is showed, discussed, and compared.

1. INTRODUCTION

Active noise control is mainly concerned with low-frequency sounds that cannot be suppressed in passive manner at reasonable cost. Other prerequisite for using ANC is that it does not obstruct media flow in ducts, for example, air conditioning ducts. Unfortunately, almost all duct applications have acoustic feedback; a phenomenon that can heavily decrease or even destroy the results of otherwise properly set-up control system [1, 2].

There are several methods for avoiding acoustic feedback in duct applications [2–6]. The best one that avoids acoustic feedback completely is to use nonacoustic reference sensor. Unfortunately, this usually limits the application to cancel the tonal sounds and does not allow for the reduction of broadband noise. Another approach to acoustic feedback is to internally process signal from the reference microphone in a way allowing to compensate for this effect [2, 4–6]. This technique, usually called "feedback neutralisation," uses a model of acoustic feedback path to filter the controller output and then subtract it from the reference signal. In the simplest case, the model is obtained offline and does not account for time variation of the feedback path. Moreover, the method requires a model of the acoustic feedback path and therefore is computationally more expensive.

The approach to acoustic feedback cancellation presented in this paper is called virtual unidirectional sound source (VUSS). The method, in authors opinion, has some advantages over well-known two loudspeaker active noise control system in duct applications. First, it clearly separates the subsystem responsible for neutralisation of undesired feedback from active noise control part. Second, its adaptive version can also be applied in case of varying acoustic path responses. Last, virtual unidirectional sound source can also be applied in more general active control of sound applications, not only in active noise control. The paper attempts to explain the theory behind VUSS as well as to give some results showing its excellent performance in case of ANC.

The paper is organised as follows. Section 2 summarises physical basics necessary to understand principles of VUSS operation and its advantage over one-loudspeaker applications. In Section 3, the idea of VUSS is explained together with the original detailed analysis of optimal (fixed) design (Section 3.1) and adaptive approach (Section 3.2). Finally, Section 4 gives the results of simulations and real

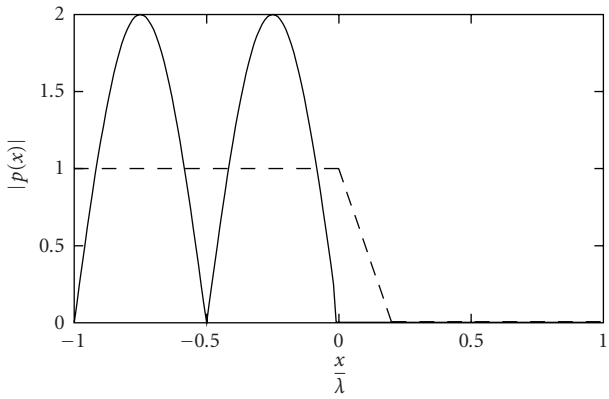

Figure 1: Acoustic pressure distribution in duct: one loudspeaker case (solid) and two loudspeaker case (dashed).

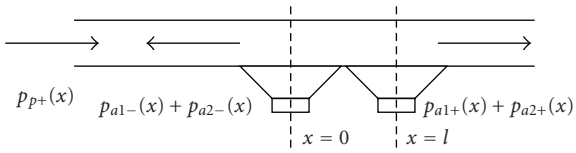

Figure 2: Acoustic duct with two active loudspeakers.

experiments of feedforward active noise control system using virtual unidirectional sound source.

2. ACOUSTICAL PHENOMENA IN DUCTS

The simplest solution to acoustic feedback cancellation problem in case where omnidirectional microphone must be used as the reference sensor is called feedback neutralisation [2, 4–6]. With this approach, only one loudspeaker is used, but the signal obtained from reference microphone is processed in the way allowing for compensation of its influence. If no compensation is performed, severe problems can result. In the simplest case of attenuation of one tone, the pressure distribution upstream secondary source [3] takes shape of standing wave, presented with solid line on Figure 1. If, for particular frequency of this tone, the reference microphone is placed in standing wave nodal point, it will give measurement equal to zero regardless of waves' actual magnitude.

Another situation occurs when two loudspeakers are used, as presented in Figure 2. Assume first loudspeaker is placed in the duct at position $x = 0$ and the second at position $x = l$. Denote $p_{p+}(x)$ as *the complex pressure* [3] at location x produced by primary source emitting tonal sound:

$$p_{p+}(x) = A\, e^{-\mathrm{i}kx}, \tag{1}$$

where A is the complex amplitude of the sound wave and where acoustic wave number k is equal to $k = \omega/c_0$, with ω being wave angular frequency and c_0 being the sound speed in air.

Assume the two loudspeakers on Figure 2 produce sound waves propagating upstream the duct, marked as $p_{a1-}(x)$ and $p_{a2-}(x)$, and sound waves propagating downstream the duct, marked as $p_{a1+}(x)$ and $p_{a2+}(x)$. Assume also that the sound wave produced by the primary source is propagating downstream the duct, as marked on the figure.

Assume that the complex pressure of sound wave generated by first "active" loudspeaker is given by

$$\begin{aligned} p_{a1+}(x) &= B\, e^{-ikx} \quad \text{for } x > 0, \\ p_{a1-}(x) &= B\, e^{ikx} \quad \text{for } x < 0, \end{aligned} \tag{2}$$

and the complex pressure of sound wave produced by the second "active" loudspeaker is given by

$$\begin{aligned} p_{a2+}(x) &= C\, e^{-ik(x-l)} \quad \text{for } x > l, \\ p_{a2-}(x) &= C\, e^{ik(x-l)} \quad \text{for } x < l, \end{aligned} \tag{3}$$

where B and C are the complex amplitudes of the sound waves.

In the situation described above it is possible to set another condition on the system regardless of primary sound source attenuation requirement. In the case of unidirectional sound source, it may be the requirement of self-cancellation of the secondary sound waves propagating upstream the duct:

$$p_{a1-}(x) + p_{a2-}(x) = 0 \quad \text{for } x < 0. \tag{4}$$

In this case, the secondary sources have to be driven in the way providing [3]

$$B = -C\, e^{-ikl}. \tag{5}$$

In the same time to achieve the main ANC goal, which is to cancel the primary sound downstream the second loudspeaker completely, it is necessary to set the complex amplitude:

$$C = \frac{-A}{2i\sin(kl)}. \tag{6}$$

The acoustic pressure level distribution for two loudspeakers case has been shown with dashed line on Figure 1. The figure shows that the sound pressure has been perfectly cancelled at coordinates $x > l$ while the absolute value of the pressure level has not been affected by the secondary sources at negative coordinates x. The zone between the secondary loudspeakers ($0 < x < l$) is a transient zone.

Although two-loudspeaker system offers significant improvement over one loudspeaker system, it has its drawbacks too. Specifically, the above control law says that for some frequencies for which $\sin(kl)$ is close to zero, both the secondary sources will have to produce sound waves with amplitude very large, compared with the amplitude A of the primary waveform. Consider, for example, the case where the loudspeakers are separated by the distance $l = 0.3$ m. In this case the sound waves of frequency 570 Hz and all its multiplies will result in $\sin(kl)$ equal to, or close to, zero, depending on the actual speed of sound, and thus on temperature, humidity, and so on. This fact will certainly influence the performance of ANC system trying to attenuate such sound waves (see, e.g., the drop in attenuation just below 600 Hz on Figure 10).

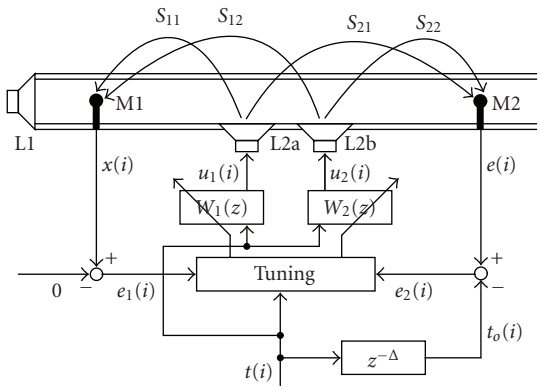

Figure 3: Block diagram of virtual unidirectional sound source.

3. VIRTUAL UNIDIRECTIONAL SOUND SOURCE

It is well known that introducing the second "active" loudspeaker allows to deal with many one-loudspeaker systems difficulties [4]. Moreover, the analysis outlined in Section 2 proves that it allows also for (hypothetically) perfect cancellation of the acoustic feedback. One of possible systems using two secondary loudspeakers is called virtual unidirectional sound source.

The idea of virtual unidirectional sound source (VUSS) is to use digital signal processing algorithm to drive *two* loudspeakers in such way that the sound produced by them propagates only downstream the duct [7]. In fact, although the sound generated by each loudspeaker propagates in both directions, the processing algorithm tries to assure that the sound waves propagating upstream the duct are actively cancelled by themselves while those propagating downstream the duct are amplified. The additional advantage of this approach is that it is sometimes possible to equalise the amplitude spectrum of the secondary path transfer function (transfer function between signals $t(i)$ and $e(i)$ on Figure 3) that plays very important role in active control of sound [4].

The block diagram of VUSS has been shown in Figure 3. The system contains two "active" loudspeakers, L2a and L2b, as well as two microphones: M1, generally called reference microphone, and M2 called error microphone (the names of the microphones correspond to the role they play in active noise control). The signal to be processed by VUSS is the set point value (or antinoise signal) $t(i)$ produced by ANC algorithm. It is filtered by two filters with transfer functions, $W_1(z)$ and $W_2(z)$, and sent to the loudspeakers, L2a and L2b, respectively. The error signals are obtained by comparing values acquired from the microphones M1 and M2 with their required values (set points). As the goal of VUSS system is to cancel the influence of the set point value $t(i)$ at the microphone M1 point, the signal $x(i)$ is compared with zero ($e_1(i) = x(i) - 0 = x(i)$). Similarly, as the desired signal at the microphone M2 point is the delayed set point value, the second error signal is calculated as $e_2(i) = e(i) - t_o(i)$. The need for delaying the set point value $t(i)$ comes from condition on causality of the system: no filtration can compensate for the delay time introduced by the acoustic path between the loudspeakers and the M2 microphone. The value of the delay ensuring causality of the algorithm should be chosen before running the algorithm. The error signals $e_1(i)$ and $e_2(i)$ are used by adaptive algorithm to update parameters of the transfer functions $W_1(z)$ and $W_2(z)$ (in case of optimal design they are used only for observing the performance of the system).

3.1. Optimal and suboptimal filter designs

In this subsection, an attempt to derive analytical optimal and suboptimal filter formulae will be made. The need for suboptimal formula will be explained and feasibility of both the solutions will be discussed.

3.1.1. Formulation using transfer functions

Suppose that the whole system presented in Figure 3 is *linear* and the signal to be cancelled is deterministic, or random *wide-sense stationary* [8]. Suppose that W_1 and W_2 are infinite impulse response (IIR) filters. Figure 3 shows that the control values $u_1(i)$ and $u_2(i)$ can be expressed as a filtration of set point value $t(i)$ by the W_1 and W_2 filters. Using the notation of difference equation, this filtration can be expressed as

$$\begin{aligned} u_1(i) &= W_1(z)\cdot t(i) = w_{1,0}t(i) + w_{1,1}t(i-1) + \cdots \\ &= \sum_{n=0}^{\infty} w_{1,n}t(i-n), \\ u_2(i) &= W_2(z)\cdot t(i) = w_{2,0}t(i) + w_{2,1}t(i-1) + \cdots \\ &= \sum_{n=0}^{\infty} w_{2,n}t(i-n), \end{aligned} \tag{7}$$

where

$$\begin{aligned} W_1(z) &= w_{1,0} + w_{1,1}z^{-1} + w_{1,2}z^{-2} + \cdots, \\ W_2(z) &= w_{2,0} + w_{2,1}z^{-1} + w_{2,2}z^{-2} + \cdots. \end{aligned} \tag{8}$$

In the above equation, $w_{1,n}$ and $w_{2,n}$ are nth elements of the W_1 and W_2 filter impulse response functions, and are also called filter coefficients. Using this notation, the z^{-1} is treated as discrete shift operator so that $z^{-n}t(i) = t(i-n)$.

From Figure 3 it also follows that the reference signal $x(i)$ due to the secondary sources measured by the M1 microphone can be expressed with the following difference equation:

$$x(i) = S_{11}(z)\cdot u_1(i) + S_{12}(z)\cdot u_2(i), \tag{9}$$

where $S_{11}(z)$ and $S_{12}(z)$ are impulse response functions of electroacoustical paths between the reference signal $x(i)$ and the $u_1(i), u_2(i)$ control values, including amplifiers, filters, loudspeakers, and others.

Similarly, the signal $e(i)$ measured by the microphone M2 due to the secondary sources can be given by

$$e(i) = S_{21}(z)\cdot u_1(i) + S_{22}(z)\cdot u_2(i). \tag{10}$$

Considering the above and the definitions of error signals given in the previous subsection, the error signals can be expressed as

$$\begin{aligned} e_1(i) &= S_{11}\cdot u_1(i) + S_{12}\cdot u_2(i), \\ e_2(i) &= S_{21}\cdot u_1(i) + S_{22}\cdot u_2(i) - t_o(i), \end{aligned} \tag{11}$$

where the dependence of S_{nn} transfer functions on z has been omitted to simplify the notation.

The goal of the tuning algorithm is to drive error signals to zero:

$$e_1(i) = 0, \qquad e_2(i) = 0. \tag{12}$$

Substituting (7) and (11) into (12), recognising that $t_o(i) = z^{-\Delta}t(i)$ gives for all $t(i) \neq 0$

$$\begin{aligned} S_{11}\cdot W_1(z) + S_{12}\cdot W_2(z) &= 0, \\ S_{21}\cdot W_1(z) + S_{22}\cdot W_2(z) &= z^{-\Delta}, \end{aligned} \tag{13}$$

where Δ samples delay time was introduced to assure causality of the system.

Solving the above equation set gives the transfer functions of optimal filters:

$$\begin{aligned} W_{1\text{opt}}(z) &= -z^{-\Delta}\frac{S_{12}}{S_{11}\cdot S_{22} - S_{12}\cdot S_{21}}, \\ W_{2\text{opt}}(z) &= z^{-\Delta}\frac{S_{11}}{S_{11}\cdot S_{22} - S_{12}\cdot S_{21}}. \end{aligned} \tag{14}$$

Unfortunately, (14) cannot be used in practise due to nonminimumphase nature of transfer functions S_{nn} leading to instability of VUSS filters. Moreover, even when all the transfer functions S_{nn} are minimumphase, the subtraction in denominator of (14) can still result in instability of the whole filter. This is referred to in the literature as "unconstrained controller" [3].

The suboptimal design of virtual unidirectional sound source can be performed after omitting the second condition from (12) set in mathematical derivations. In consequence, it means we do not expect the transfer function from set point value $t(i)$ to microphone M2 signal $e(i)$ to be pure delay, but we allow it to take more complex form. Furthermore, it means that the amplitude spectrum of this transfer function will not be flat over the frequency range under consideration. However, we still request cancellation of the secondary sources influence on the reference signal $x(i)$.

With control goal stated above, there are two equivalent solutions that will be called suboptimal, namely,

$$\begin{aligned} W_{1\text{sub}}(z) &= -S_{12}(z), \\ W_{2\text{sub}}(z) &= S_{11}(z), \end{aligned} \tag{15}$$

or

$$\begin{aligned} W_{1\text{sub}}(z) &= S_{12}(z), \\ W_{2\text{sub}}(z) &= -S_{11}(z). \end{aligned} \tag{16}$$

Moreover, assuming the S_{nn} transfer functions are of FIR type, the suboptimal solutions are also FIR type.

It is, however, important to notice that in case of suboptimal solution the secondary path transfer function (transfer function between signals $t(i)$ and $e(i)$ on Figure 3) is given by

$$\begin{aligned} S(z) &= -S_{12}\cdot S_{21} + S_{11}\cdot S_{22}, \text{ or} \\ S(z) &= S_{12}\cdot S_{21} - S_{11}\cdot S_{22}. \end{aligned} \tag{17}$$

(Again, the dependence of S_{nn} transfer functions on z has been omitted to clarify the notation.) This shows that in case of no demand for equalisation of the secondary path transfer function amplitude spectrum it can assume arbitrary shape, potentially "worse" than in case of single secondary source. This effect must be taken into account when estimating secondary path models required by active noise control algorithm (e.g., by using longer filters).

3.1.2. Formulation using reference signal matrix

The following subsection presents result obtained using the approach presented in [3, 9], which is based on impulse response of appropriate electroacoustic paths and on the use of filtered-reference signals. Using this approach, the lth error signal ($l = \{1, 2\}$ in this case) can be expressed as a sum of desired signals and contributions from m secondary sources (with $m = 2$ in this case) as:

$$e_l(i) = -d_l(i) + \sum_{m=1}^{2}\sum_{j=0}^{J-1} s_{lm}(j)u_m(i-j), \tag{18}$$

where $s_{lm}(j)$ is the jth coefficient of impulse response of electroacoustic path between the lth sensor and the mth actuator and $d_l(i)$ is desired value of the lth sensor signal. The length of impulse response can be arbitrary number J guaranteeing desired accuracy.

In the same manner, the signals driving actuators can be expressed as

$$u_m(i) = \sum_{n=0}^{N-1} w_{m,n}t(i-n), \tag{19}$$

where $w_{m,n}$ is the nth parameter of the Nth order w_m FIR filter impulse response.

Substituting (19) into (18) yields

$$e_l(i) = -d_l(i) + \sum_{m=1}^{2}\sum_{j=0}^{J-1}\sum_{n=0}^{N-1} s_{lm}(j)w_{m,n}t(i-j-n). \tag{20}$$

To derive a matrix formulation for the above equation it is necessary to reorganise the order of filtration of the set point value $t(i)$. To do this, it is necessary to assume that the filters s_{lm} and $w_{m,n}$ are time invariant. If the filtered reference signal is defined as

$$r_{lm}(i) = \sum_{j=0}^{J-1} s_{lm}(j)t(i-j), \tag{21}$$

the error signals can be written as

$$e_l(i) = -d_l(i) + \sum_{m=1}^{2} \sum_{n=0}^{N-1} w_{m,n} r_{lm}(i-n). \tag{22}$$

After defining

$$\mathbf{w}(i) = \begin{bmatrix} w_{1,i} \\ w_{2,i} \end{bmatrix}, \qquad \mathbf{r}_l(i) = \begin{bmatrix} r_{l1}(i) \\ r_{l2}(i) \end{bmatrix}. \tag{23}$$

Equation (22) can be expressed as

$$e_l(i) = -d_l(i) + \sum_{n=0}^{N-1} \mathbf{w}^T(n) \mathbf{r}_l(i-n). \tag{24}$$

Finally, the vector of two error signals can be defined as

$$\mathbf{e}(i) = \begin{bmatrix} e_1(i) & e_2(i) \end{bmatrix}^T \tag{25}$$

and the vector of two desired signals can be defined as

$$\mathbf{d}(i) = \begin{bmatrix} d_1(i) & d_2(i) \end{bmatrix}^T, \tag{26}$$

leading to the conclusive formula

$$\mathbf{e}(i) = -\mathbf{d}(i) + \mathbf{R}(i)\mathbf{W}, \tag{27}$$

where

$$\mathbf{R}(i) = \begin{bmatrix} \mathbf{r}_1^T(i) & \mathbf{r}_1^T(i-1) & \cdots & \mathbf{r}_1^T(i-N+1) \\ \mathbf{r}_2^T(i) & \mathbf{r}_2^T(i-1) & \cdots & \mathbf{r}_2^T(i-N+1) \end{bmatrix} \tag{28}$$

is called matrix of filtered reference signals, and

$$\mathbf{W} = \begin{bmatrix} \mathbf{w}^T(0) & \mathbf{w}^T(1) & \ldots & \mathbf{w}^T(N-1) \end{bmatrix}^T \tag{29}$$

is the vector containing all the coefficients of both W_1 and W_2 filters (the filters are time independent).

It is interesting to notice that in case of virtual unidirectional sound source the vector of desired signals can be instantiated as

$$\mathbf{d}(i) = \begin{bmatrix} 0 \\ t(i-\Delta) \end{bmatrix}. \tag{30}$$

Following the methodology presented in [9] the optimal filter solution can be expressed as

$$\mathbf{W}_{\text{opt}} = \left[E\{\mathbf{R}^T(i)\mathbf{R}(i)\}\right]^{-1} E\{\mathbf{R}^T(i)\mathbf{d}(i)\}, \tag{31}$$

where $E\{\cdot\}$ denotes expectation operator.

The matrix to be inverted is of dimension $N \times N$, where N is the filter length. Fortunately, it can be proved that the matrix is block Toeplitz matrix [3], so effective iterative methods can be applied for inversion. The expectation operator tells that statistical properties of filtered set point value $t(i)$ will be taken into account. The expression under the right-hand side expectation operator, in the above equation, takes particularly the simple form of

$$\mathbf{R}^T(i)\mathbf{d}(i) = \begin{bmatrix} \mathbf{r}_2^T(i) & \mathbf{r}_2^T(i-1) & \cdots & \mathbf{r}_2^T(i-N+1) \end{bmatrix}^T t(i-\Delta). \tag{32}$$

3.1.3. Formulation in frequency domain

Applying the Fourier transform to (7) and (11) and substituting the transformed (7) into (11) yields

$$\begin{aligned} E_1(e^{i\omega T_p}) &= S_{11}(e^{i\omega T_p}) W_1(e^{i\omega T_p}) T(e^{i\omega T_p}) \\ &\quad + S_{12}(e^{i\omega T_p}) W_2(e^{i\omega T_p}) T(e^{i\omega T_p}), \\ E_2(e^{i\omega T_p}) &= S_{21}(e^{i\omega T_p}) W_1(e^{i\omega T_p}) T(e^{i\omega T_p}) \\ &\quad + S_{22}(e^{i\omega T_p}) W_2(e^{i\omega T_p}) T(e^{i\omega T_p}) \\ &\quad - T_o(e^{i\omega T_p}) \end{aligned} \tag{33}$$

with $z = e^{i\omega T_p}$, where T_p is a sampling period.

The above equations can be expressed in more convenient matrix form as

$$\mathbf{e}(e^{i\omega T_p}) = -\mathbf{d}(e^{i\omega T_p}) + \mathbf{S}(e^{i\omega T_p}) \mathbf{W}(e^{i\omega T_p}) T(e^{i\omega T_p}), \tag{34}$$

where $\mathbf{e}(e^{i\omega T_p}), \mathbf{d}(e^{i\omega T_p})$, and $\mathbf{W}(e^{i\omega T_p})$ are transformed vectors defined by (25), (30), and (29), respectively, and the matrix of transfer functions is defined as

$$\mathbf{S}(e^{j\omega T_p}) = \begin{bmatrix} S_{11}(e^{i\omega T_p}) & S_{12}(e^{i\omega T_p}) \\ S_{21}(e^{i\omega T_p}) & S_{22}(e^{i\omega T_p}) \end{bmatrix}. \tag{35}$$

The unconstrained controller can be found by minimising the cost function equal to expectation of the sum of squared errors, independently at each frequency [3]:

$$J = E\{\mathbf{e}^H \mathbf{e}\} = \text{trace}\, E\{\mathbf{e}\,\mathbf{e}^H\}. \tag{36}$$

Thus, the optimal controller is equal to

$$\mathbf{W}_{\text{opt}}(e^{i\omega T_p}) = \mathbf{S}^{-1}(e^{i\omega T_p}) \mathbf{S}_{td}(e^{i\omega T_p}) \mathbf{S}_{tt}^{-1}(e^{i\omega T_p}), \tag{37}$$

where matrices of power and cross spectral densities are defined as

$$\begin{aligned} \mathbf{S}_{td}(e^{i\omega T_p}) &= E\{\mathbf{d}(e^{i\omega T_p})\, T^*(e^{i\omega T_p})\}, \\ \mathbf{S}_{tt}(e^{i\omega T_p}) &= E\{T(e^{i\omega T_p})\, T^*(e^{i\omega T_p})\}. \end{aligned} \tag{38}$$

Assume now that the set point value $t(i)$ used during VUSS learning phase is a sequence of white noise with expected value σ^2. The power spectral density matrix $\mathbf{S}_{tt}$ is then equal to

$$\mathbf{S}_{tt}(e^{i\omega T_p}) = \sigma^2, \tag{39}$$

independent on ω, and the cross spectral density matrix $\mathbf{S}_{td}$ is equal to

$$\mathbf{S}_{td}(e^{i\omega T_p}) = \begin{bmatrix} 0 \\ e^{-i\omega T_p \Delta} \sigma^2 \end{bmatrix}. \tag{40}$$

After evaluating inverse of transfer function block matrix $\mathbf{S}(e^{i\omega T_p})$, the optimal controller obtained with white noise excitation becomes

$$\mathbf{W}_{\text{opt}}(e^{i\omega T_p}) = \frac{e^{-i\omega T_p \Delta}}{S_{11}S_{22} - S_{12}S_{21}} \begin{bmatrix} -S_{12} \\ S_{11} \end{bmatrix}, \tag{41}$$

where the dependence of S_{nn} transfer function on $e^{i\omega T_p}$ has been omitted to clarify the notation.

The above equation is consistent with the result obtained in Section 3.1.1. It is, however, still the unconstrained form of the controller which is not feasible for practical implementation.

3.2. Adaptive filter solution

This subsection presents an alternative approach to optimal and suboptimal filter designs discussed above. Now we will try to develop an adaptive algorithm with the goal defined by set of (12). We will assume that $W_1(z)$ and $W_2(z)$ are in form of finite impulse response filters so the filter coefficients can be stored in a vector similar to this defined by (29), but now with coefficients varying slowly (compared to timescales of plant dynamics) in time.

Although there are many algorithms that can be used to tune filter coefficients [4], two-channel *filtered-x* LMS algorithm was chosen for the following derivation and experiments. Its advantages are simplicity and robustness, even if speed of convergence is not the best. Using two-channel FXLMS algorithm, the update equation is given by

$$\mathbf{W}(i+1) = \mathbf{W}(i) + \mu \mathbf{R}^T(i)\mathbf{e}(i), \tag{42}$$

where μ is step size and $\mathbf{R}(i)$ and $\mathbf{e}(i)$ are defined by (28) and (25), respectively.

The matrix of reference signals $\mathbf{R}(i)$ is generated by filtration of the set point value by electroacoustic path transfer functions $S_{11}(z)$ to $S_{22}(z)$. In practise, the latter can be only estimated yielding a matrix of estimated plant responses $\hat{\mathbf{R}}(i)$. The estimation must take place before running FXLMS algorithm and is usually done by separate identification procedure. The same procedure can also be turned on during active noise control phase after detecting substantial changes in plant dynamics (e.g., changes in air temperature).

To study convergence properties of the above algorithm, it is necessary to substitute (27) into (42) with estimated plant responses matrix, producing

$$\mathbf{W}(i+1) = \mathbf{W}(i) + \mu\left[-\hat{\mathbf{R}}^T(i)\mathbf{d}(i) + \hat{\mathbf{R}}^T(i)\mathbf{R}(i)\mathbf{W}(i)\right]. \tag{43}$$

If the adaptive algorithm is stable, it will converge to the solution setting the expectation value of the term in bracket to zero [3]. The steady-state vector of filter coefficients will therefore be equal to

$$\mathbf{W}_\infty = \left\{E\left[\hat{\mathbf{R}}(i)\mathbf{R}(i)\right]\right\}^{-1} E\left[\hat{\mathbf{R}}(i)\mathbf{d}(i)\right]. \tag{44}$$

The above result for the adaptive algorithm steady state is in coincidence with the optimal solution presented in Section 3.1.2 (31) if and only if the estimated matrix of reference signals $\hat{\mathbf{R}}$ is equal to the true matrix of reference signal. This validates, however, the methodology.

The precise consequences of nonperfect matching of true plant responses contained in the matrix of reference signals on adaptation process are still unknown. The strongest result has been shown by Wang and Ren [10], the sufficient condition for stability of adaptation. Nevertheless it is not a necessary condition and it has been obtained with the small step size assumption.

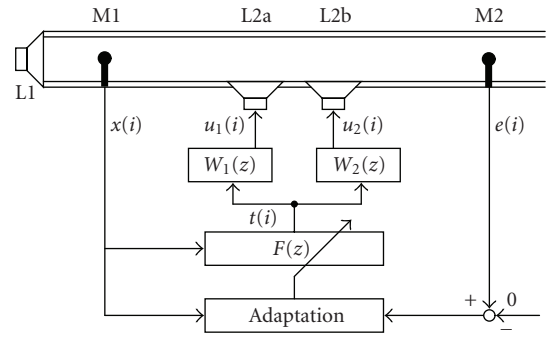

Figure 4: Active noise control system using virtual unidirectional sound source.

During this research it was useful to introduce an additional weight parameter $\beta \in (0,1)$ to specify which of the goals defined in (12) should have more bearing on adaptation process. For such case the definition of error vector $\mathbf{e}(i)$ was modified as follows:

$$\mathbf{e}'(i) = \begin{bmatrix} (1-\beta)e_1(i) \\ \beta e_2(i) \end{bmatrix} = \begin{bmatrix} (1-\beta) & 0 \\ 0 & \beta \end{bmatrix} \mathbf{e}(i) = \mathbf{B}\mathbf{e}(i). \tag{45}$$

When β is close to zero, the algorithm is better excited along the modes responsible for neutralisation of the acoustic feedback effect, while when β is close to one the algorithm puts more stress on equalising the secondary path transfer function.

Introducing the weight parameter β modifies the steady-state vector of filter coefficients giving

$$\mathbf{W}_\infty = \left\{E\left[\hat{\mathbf{R}}(i)\mathbf{B}\mathbf{R}(i)\right]\right\}^{-1} E\left[\hat{\mathbf{R}}(i)\mathbf{B}\mathbf{d}(i)\right]. \tag{46}$$

The maximum step size parameter, μ, assuring convergence of the whole algorithm is given by

$$0 < \mu < \frac{2\mathrm{Re}(\lambda_{\max})}{|\lambda_{\max}|^2}, \tag{47}$$

where $\lambda_{\max}$ denotes maximum eigenvalue of $\hat{\mathbf{R}}(i)\mathbf{B}\mathbf{R}(i)$ matrix rather than $\hat{\mathbf{R}}(i)\mathbf{R}(i)$ as was in the original solution [3]. The weight parameter β can therefore influence, to some degree, the eigenvalues of the matrix under consideration.

4. ACTIVE NOISE CONTROL WITH VUSS

4.1. Active noise control algorithms

Feedforward active noise control system using virtual unidirectional sound source has been shown in Figure 4. This system uses a finite impulse response filter as control filter with different adaptation algorithms. As in case of all feedforward algorithms, only the reference value $x(i)$ is used

by the control filter $F(z)$ to produce the set point value $t(i)$. The set point value is then processed by VUSS filters $W_1(z)$ and $W_2(z)$ to give two control values $u_1(i)$ and $u_2(i)$ that are amplified and sent to the loudspeakers (via amplifiers and reconstruction filters not shown on the figure). The adaptation algorithm on the other hand uses the reference signal $x(i)$ as well as the error signal $e(i)$ to tune the control filter coefficients.

The duct used in experiments described below was made out of wood. It was 4 m long, with 0.2×0.4 m rectangular section. One of the duct ends was terminated with noise generating loudspeaker, while the other was opened. The attenuating loudspeakers were of 0.16 m diameter and were situated approximately in the middle of the duct. The distance between the middles of the loudspeakers was equal to 0.3 m. The reference microphone was located 1.23 m from the middle of L2a loudspeaker, while the error microphone was separated from L2b loudspeaker by the distance of 0.23 m.

It should be emphasised that the goal of active noise control algorithm is in contradiction to the goal of the virtual unidirectional sound source adaptation algorithm [11]. The former tries to assure the compensation of sound waves from both the primary and secondary sources at the microphone M2 point without taking any notice of what happens at the microphone M1 point. The goal of the latter is to compensate sound waves from the secondary sources only at the microphone M1 point and try to assure the set point value appearing without any alternation at the microphone M2 point. This leads to a conclusion that both the algorithms should never operate at the same time. Indeed, the experiments show that when both the adaptation algorithms are in operation the whole system goes unstable. Therefore, the VUSS adaptation algorithm is usually run on the beginning of experiments and switched off after adaptation is completed. Next, only ANC algorithm is in use. Only when significant changes in the environment are detected (e.g., temperature change above some level), the ANC adaptation is temporarily frozen and the VUSS is retuned.

FXLMS algorithm

The first of ANC filter adaptation algorithms tested was Filtered-x LMS algorithm [4, 9]. Assume that the $F(z)$ is an FIR filter with coefficients (see Figure 4) in the ith sample of time stored in a form of a vector $\mathbf{f}(i)$. In that case, the FXLMS algorithm update equation is given by

$$\mathbf{f}(i+1) = \mathbf{f}(i) + \mu \cdot \mathbf{x}'(i) \cdot e(i), \tag{48}$$

where μ is the step size and $\mathbf{x}'(i)$ is the vector of reference signal $x(i)$ samples filtered by the secondary path transfer function estimate, that is, an estimate of the transfer function between set point value signal $t(i)$ and error signal $e(i)$.

If VUSS algorithm was working perfectly, the secondary path transfer function would be equal to simple time delay. Unfortunately, the study from Section 3.1 leads to a conclusion that such perfect situation is impossible: the VUSS algorithm has to "pay more attention" to neutralising acoustic feedback and secondary path equalisation is only its additional task.

RLS Algorithm

The second algorithm of ANC filter adaptation algorithms tested was recursive least squares (RLS) algorithm (see, e.g., [9]). RLS algorithm uses very similar update equation in the form

$$\mathbf{f}(i+1) = \mathbf{f}(i) + \mathbf{k}(i) \cdot e(i), \tag{49}$$

where $\mathbf{k}(i)$ is the gain vector showing how much the value of $e(i)$ will modify different filter coefficients. The gain vector is calculated as

$$\mathbf{k}(i) = \mathbf{P}(i) \cdot \mathbf{x}(i), \tag{50}$$

where $\mathbf{P}(i)$ is a matrix updated in each step according to the following equation:

$$\mathbf{P}(i) = \frac{1}{\lambda}\left(\mathbf{P}(i-1) - \frac{\mathbf{P}(i-1)\mathbf{x}(i-1)\mathbf{x}^T(i-1)\mathbf{P}(i-1)}{\lambda + \mathbf{x}^T(i-1)\mathbf{P}(i-1)\mathbf{x}(i-1)}\right). \tag{51}$$

The RLS algorithm usually converges faster than the LMS algorithm [12].

Because RLS algorithm needs to update $\mathbf{P}$ matrix of size equal to the number of filter coefficients in each adaptation step, it requires computational effort of N^2, whereas LMS algorithm requires computational effort of N only [13]. There is, however, a family of RLS algorithm implementations called fast RLS algorithms that allows to omit computation of $\mathbf{P}$ matrix and use a selection of row vector instead [13, 14]. This work used one of such fast algorithms, called *fast transversal filter* [15]. The algorithm was parametrised as follows. The initial value of the minimum sum of backward a posteriori prediction-error squares was equal to 1 and the exponential weighting factor was equal to 0.9999. The algorithm showed no stability issues, as it was expected on floating-point arithmetic platform.

Both the FXLMS and RLS algorithms were implemented in C programming language. Testing and debugging were performed using developed simulation platform for Linux operating system. The platform allowed to emulate DSP processor board behaviour and therefore the next step, moving the code onto Texas Instruments TMS320C31 processor board, was purely automatic. Another PC-computer program was used to tune various algorithm parameters and to acquire the results. The sampling frequency of 2 kHz was chosen as frequency band up to 1 kHz was of the author interest. It appeared that, due to hardware limitations, appliable filter lengths were up to 70 with this sampling frequency.

4.2. Testing sounds

The set of signals chosen for experiments is presented with dashed line on Figures 12–17. Testing signals N1 and N2

Table 1: The attenuation in simulations.

Signal	Analytical solution + FXLMS	Analytical solution + FXLMS	Analytical solution + RLS
N1	9 dB	15 dB	16 dB
N2	16 dB	30 dB	33 dB
N3	10 dB	15 dB	16 dB
N4	15 dB	22 dB	22 dB
N5	9 dB	17 dB	18 dB
N6	6 dB	9 dB	8 dB

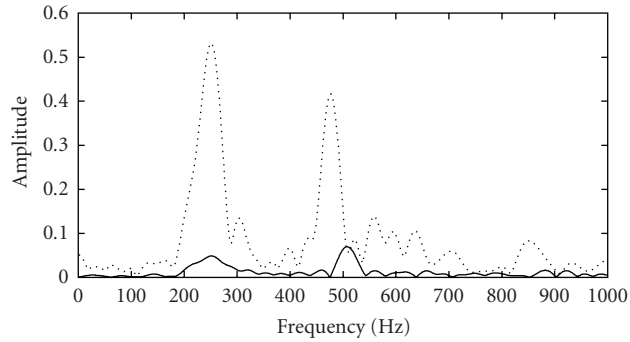

Figure 5: Amplitude spectrum of transfer function between set point value $t(i)$ and $x(i)$ (solid) and $e(i)$ (dotted).

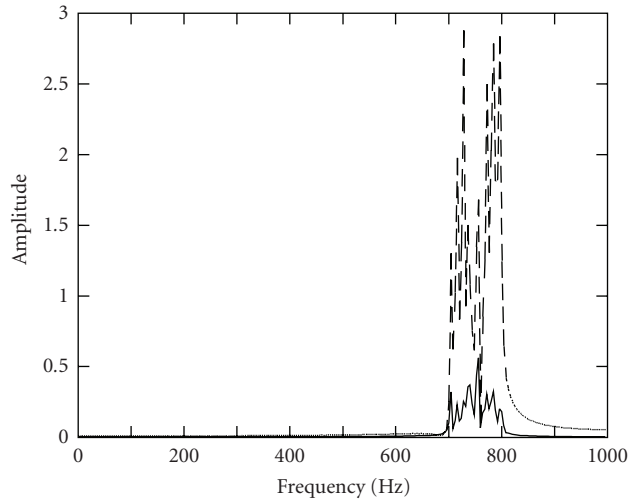

Figure 6: Noise N2 attenuation using analytical VUSS solution. — Spectrum with ANC, - - - spectrum without ANC.

were generated offline as white noise filtered with high-order bandpass filter. Bandpass was 200–300 Hz in case of N1 signal and 700–800 Hz in case of signal N2. The former was chosen to show low-frequency attenuation capabilities and the latter to show high frequency attenuation. The N3 is a signal acquired in close vicinity of a food processor. It has the dominant frequency of about 270 Hz, but with substantial amount of broadband noise. The N4 is a signal collected near a power transformer. It has all the harmonics of 50 Hz visible

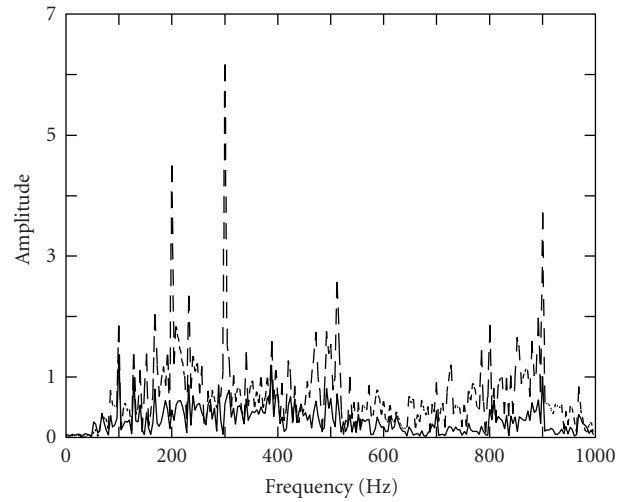

Figure 7: Noise N5 attenuation using analytical VUSS solution. — Spectrum with ANC, - - - spectrum without ANC.

with 250 Hz being the dominant. The N5 signal was recorded in water power plant turbine proximity. It has the harmonics of 100 Hz distinguishable among broadband noise. The last signal N6 was recorded in small bureau with an electric propeller fan turned on. It is similar to N5, but the dominant frequency is higher.

All the signals were filed using 1000 samples. This ensemble was repeated many times and (after amplification) sent to loudspeaker L2 (see Figure 4). The results of attenuation were measured with microphone M2 and calculated as

$$\mathcal{T} = 10 \log \left(\frac{\text{MSV of } e(i) \text{ without attenuation}}{\text{MSV of } e(i) \text{ with attenuation}} \right) \text{ [dB]}. \quad (52)$$

4.3. Simulation results

The simulations were performed using 150th order FIR filters models of the duct paths, identified offline using methodology presented in [16]. The algorithm for suboptimal VUSS filter solution described in Section 3.1 was tested first. As expected, it allowed for very effective acoustical feedback cancellation but at the cost of the secondary path being substantially degenerated. The amplitude spectrum of transfer function between set point value $t(i)$ and both the reference signal $x(i)$ and error signal $e(i)$ is presented on Figure 5.

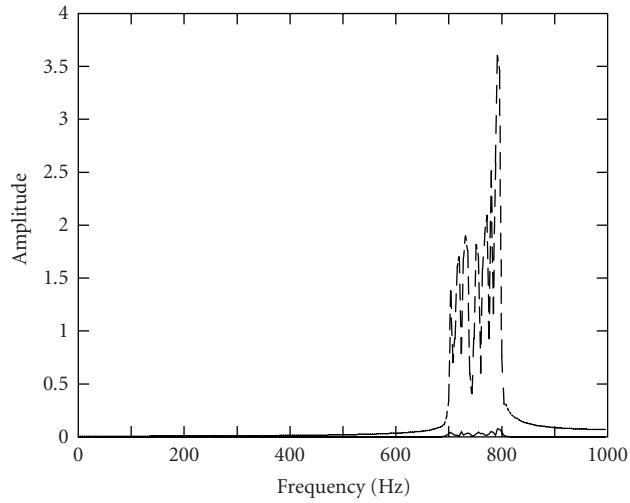

Figure 8: Noise N2 attenuation using adaptive VUSS solution. — Spectrum with ANC, - - - spectrum without ANC.

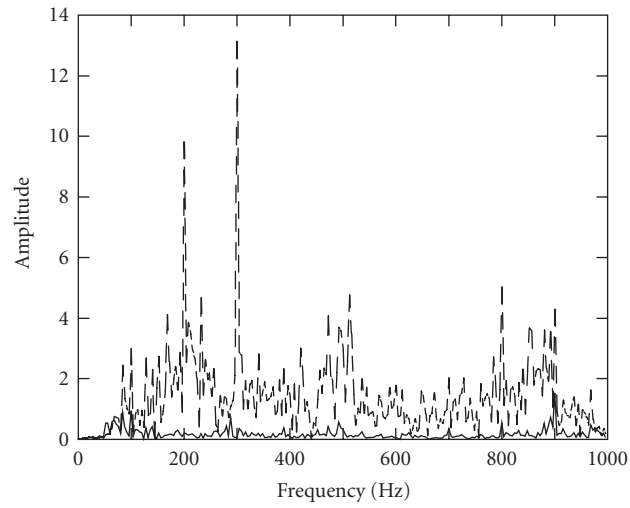

Figure 9: Noise N5 attenuation using adaptive VUSS solution. — Spectrum with ANC, - - - spectrum without ANC.

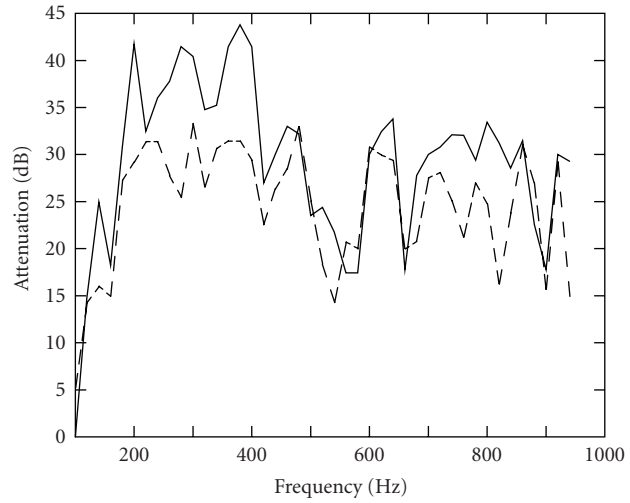

Figure 10: Attenuation (in dB) of tonal sounds for adaptive filter tuning. — RLS algorithm, - - - FXLMS algorithm.

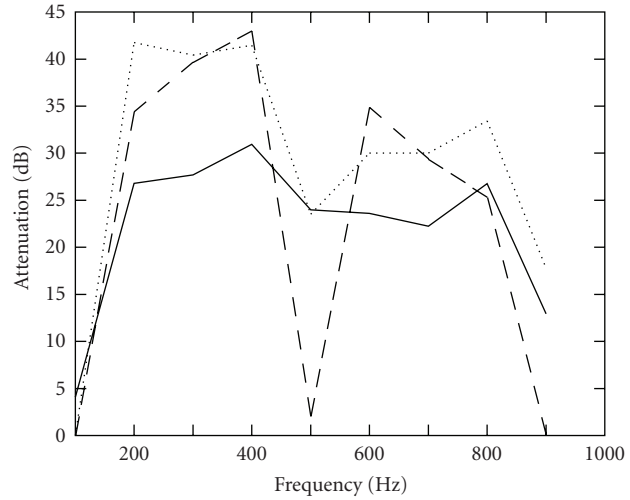

Figure 11: Comparison of attenuation of tonal sounds for analytical and adaptive VUSS filter tuning. — FXLMS algorithm with analytical tuning, - - - RLS algorithm with analytical tuning, ... RLS algorithm with adaptive tuning.

After tuning phase, the system was engaged to active noise control algorithms: FXLMS and Fast RLS. The ANC filter having 70 coefficients proved to be long enough to cancel out the noise in case of tonal sounds, so this was the chosen value. However, in case of N1–N6 signals attenuation was only (as for simulations of feedforward controller) 6–16 dB (with FXLMS algorithm, which proved to be better), see Table 1. The examples of spectra of the signals observed at the error microphone before and after attenuation have been presented on Figures 6 and 7.

In the following experiments, adaptive algorithm described in Section 3.2 was responsible for VUSS filters tuning. The value of the β parameter (see (45)) has been chosen as 0.5 to put the same effort into satisfying both the goals defined by (12). The attenuation of tonal sounds was also infinite in case of adaptive VUSS filters tuning. But the attenuation of testing signals was slightly better: 9–30 dB in case of FXLMS algorithm and 8–33 dB in case of RLS algorithm, see Table 1. The examples of spectra of the signals observed at the error microphone before and after attenuation have been shown on Figures 8 and 9. The difference in amplitude spectrum of the N2 and N5 signals without attenuation visible on these figures and on Figure 6 and 7 comes from the fact that this is the spectrum measured with the M2 microphone, not the spectrum of the signal driving the L1 loudspeaker.

Table 1 summarises the results obtained during simulations for broadband signals N1–N6. The simulation experiments proved adaptive VUSS filters tuning superiority over analytical suboptimal filter design.

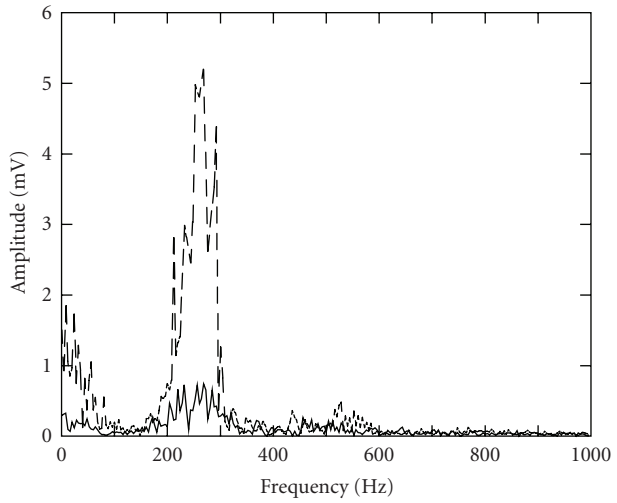

Figure 12: Noise N1 (broadband noise 200–300 Hz) attenuation. — Spectrum with ANC, - - - spectrum without ANC.

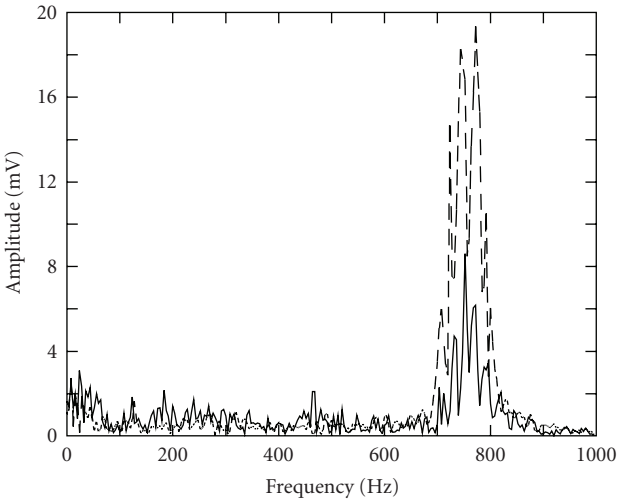

Figure 13: Noise N2 (broadband noise 700–800 Hz) attenuation. — Spectrum with ANC, - - - spectrum without ANC.

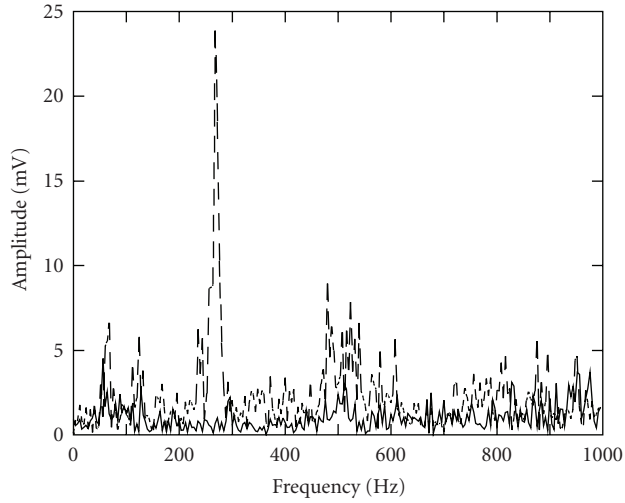

Figure 14: Noise N3 (food processor) attenuation. — Spectrum with ANC, - - - spectrum without ANC.

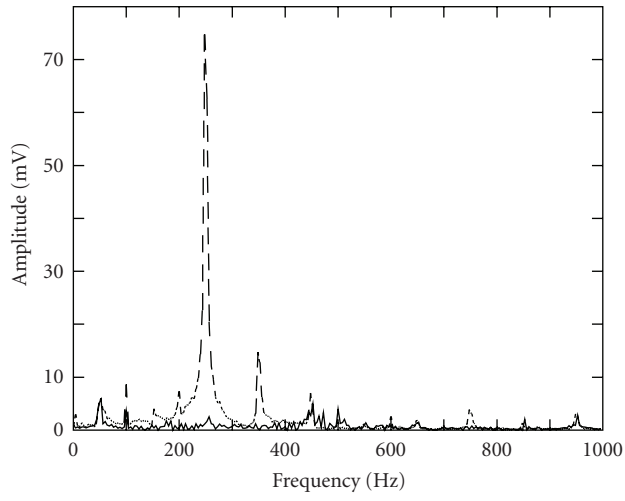

Figure 15: Noise N4 (power transformer) attenuation. — Spectrum with ANC, - - - spectrum without ANC.

4.4. Real experiments

To perform the real experiments using analytical filter design it was necessary to identify the models of electroacoustic paths $S_{11}(z) - S_{22}(z)$ (see Figure 3) first. The identification of FIR models of these paths was performed using LMS algorithm prior to each experiment. Moreover, in case of both the analytical and adaptive filter designs it was necessary to identify the model of the secondary path before the ANC. The identification of FIR model of this path was performed after VUSS was tuned by online identification procedure. The procedure, however, was disabled during the ANC.

The first ANC laboratory experiments used tonal sounds. The frequency range between 100 and 950 Hz has been checked with resolution of 20 Hz. The VUSS filter design was performed using adaptive method. The attenuation obtained during these experiments has been shown on Figure 10. The figure shows that in frequency range from 150 to 950 Hz the attenuation was between 14 and 33 dB (average 25 dB) for FXLMS ANC algorithm and between 15 and 44 dB (average 30 dB) for RLS ANC algorithm.

The drop in attenuation above a frequency of about 420 Hz, especially distinct in case of RLS algorithm, can be explained as the ducts first cut-on frequency appears at 425 Hz. The figure shows that the performances of both FXLMS and RLS algorithms above first cut-on frequency are similar. However, below a frequency of 400 Hz the performance of RLS algorithm is up to 14 dB better than in case of FXLMS algorithm.

The next step was to compare the performance of ANC system in case of analytical and adaptive filter design. During these experiments frequency range from 100 to 900 Hz was tested with resolution of 100 Hz. The results are shown on Figure 11. In all cases the efficiency of ANC algorithm with

Table 2: The attenuation in real experiments.

Signal	Adaptive solution + FXLMS	Adaptive solution + RLS
N1	12 dB	14 dB
N2	7 dB	7 dB
N3	4 dB	8 dB
N4	13 dB	16 dB
N5	3 dB	8 dB
N6	3 dB	5 dB

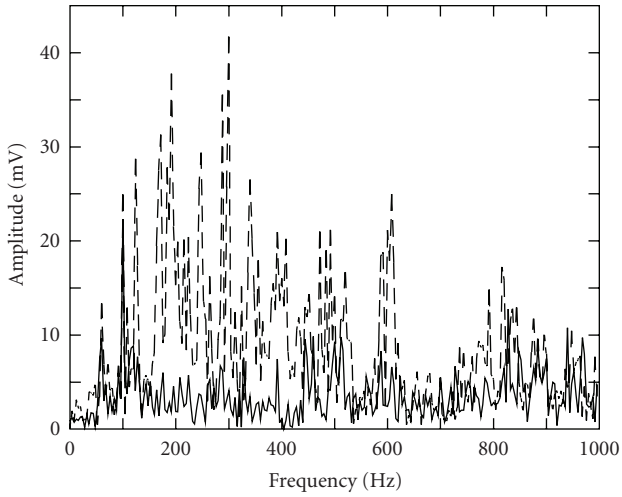

Figure 16: Noise N5 (power plant turbine) attenuation. — Spectrum with ANC, - - - spectrum without ANC.

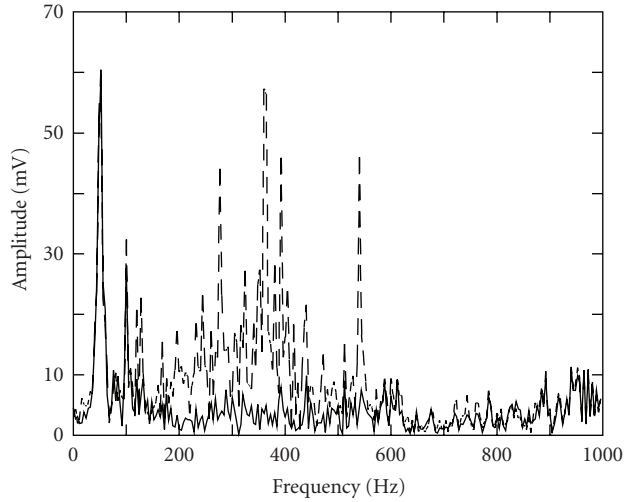

Figure 17: Noise N6 (electric propeller fan) attenuation. — Spectrum with ANC, - - - spectrum without ANC.

analytical VUSS tuning was worse than efficiency of the same algorithm with adaptive VUSS tuning. Therefore, only adaptive VUSS design was considered for the following tests.

Finally, the noise signals described in Section 4.2 were used in real experiments. Although both FXLMS and RLS ANC algorithms were checked for performance, the only spectra presented on Figure 12 through Figure 17 are those obtained with RLS algorithm, as this algorithm performance was superior to FXLMS in all experiments. The attenuation factors for both FXLMS and RLS algorithms are presented in Table 2.

5. CONCLUSIONS

The idea of virtual unidirectional sound source presented in this paper is based on theoretical study of wave propagation in duct. VUSS itself is a special case of two-reference, two-output system with a detailed analysis presented in Section 3. Its application to active noise control in an acoustic duct proved to be effective, resulting in 20–40 dB attenuation of tonal sounds and 5–16 dB attenuation of complex signals with broadband noise. The best results were obtained with adaptive VUSS design together with RLS active noise control algorithm. These results are comparable with similar results reported by other authors. The results, however, do not show one of the strengths of VUSS, the ability to adapt to time varying feedback paths.

REFERENCES

[1] D. Bismor, "Różnice pomidzy obiektami automatyki przemysłowej a obiektami akustycznymi w świetle doświadczeń identyfikacyjnych," in *Materiały XXV Zimowej Szkoły Zwalczania Zagrożeń Wibroakustycznych*, Gliwice-Ustroń, Poland, 1997.

[2] M. T. Akhtar, M. Abe, and M. Kawamata, "On active noise control systems with online acoustic feedback path modeling," *IEEE Transactions on Audio, Speech and Language Processing*, vol. 15, no. 2, pp. 593–600, 2007.

[3] S. Elliott, *Signal Processing for Active Noise Control*, Academic Press, London, UK, 2001.

[4] S. Kuo and D. Morgan, *Active Noise Control Systems*, John Wiley & Sons, New York, NY, USA, 1996.

[5] J. Poshtan, S. Sadeghi, and M. H. Kahaei, "An investigation on the effect of acoustic feedback in a single-channel active noise control system," in *Proceedings of the IEEE Conference on Control Applications (CCA '03)*, vol. 1, pp. 430–434, Istanbul, Turkey, June 2003.

[6] T. Habib, M. Akhtar, and M. Arif, "Acoustic feedback path modeling and neutralization in active noise control systems," in *Proceedings of the IEEE Multitopic Conference (INMIC '06)*, pp. 89–93, Islamabad, Pakistan, December 2006.

[7] V. Välimäki and S. Uosukainen, "Adaptive design of a unidirectional source in a duct," in *Proceedings of the 23th International Conference on Noise and Vibration Engineering (ISMA23 '98)*, vol. 3, pp. 1253–1260, Leuven, Belgium, September 1998.
[8] E. Wong, *Procesy Stochastyczne w Teorii Informacji i Układów Dynamicznych*, WNT, Warszawa, Poland, 1976.
[9] S. Haykin, *Adaptive Filter Theory*, Prentice-Hall, New York, NY, USA, 4th edition, 2002.
[10] A. K. Wang and W. Ren, "Convergence analysis of the multivariable filtered-X LMS algorithm
with application to active noise control," *IEEE Transactions on Signal Processing*, vol. 47, no. 4, pp. 1166–1169, 1999.
[11] D. Bismor, "Generation of effect of virtual undirectional source of sound using adaptive techniques," *Archives of Control Sciences*, vol. 13, no. 2, pp. 215–230, 2003.
[12] D. Bismor, "RLS algorithm in active noise control," in *Proceedings of the 6th International Congress on Sound and Vibration (ICSV '99)*, Lyngby, Denmark, July 1999.
[13] A. H. Sayed, *Fundamentals of Adaptive Filtering*, John Wiley & Sons, New York, NY, USA, 2003.
[14] L. Rutkowski, *Filtry Adaptacyjne i Adaptacyjne Przetwarzanie Sygnałów*, WNT, Warszawa, Poland, 1994.
[15] J. Cioffi and T. Kailath, "Fast, recursive-least-squares transversal filters for adaptive filtering," *IEEE Transactions on Acoustics, Speech and Signal Processing*, vol. 32, no. 2, pp. 304–337, 1984.
[16] D. Bismor, *Adaptive Algorithms for Active Noise Control in an Acoustic Duct*, Jacek Skalmierski Computer Studio, Gliwice, Poland, 1999.

Hindawi Publishing Corporation
Advances in Acoustics and Vibration
Volume 2008, Article ID 863603, 7 pages
doi:10.1155/2008/863603

Research Article

Noninvasive Model Independent Noise Control with Adaptive Feedback Cancellation

Jing Yuan

Department of Mechanical Engineering, Faculty of Engineering, The Hong Kong Polytechnic University, Hung Hom, Kowloon, Hong Kong

Correspondence should be addressed to Jing Yuan, mmjyuan@polyu.edu.hk

Received 12 November 2007; Accepted 2 February 2008

Recommended by Marek Pawelczyk

An active noise control (ANC) system is model dependent/independent if its controller transfer function is dependent/independent on initial estimates of path models in a sound field. Since parameters of path models in a sound field will change when boundary conditions of the sound field change, model-independent ANC systems (MIANC) are able to tolerate variations of boundary conditions in sound fields and more reliable than model-dependent counterparts. A possible way to implement MIANC systems is online path modeling. Many such systems require invasive probing signals (persistent excitations) to obtain accurate estimates of path models. In this study, a noninvasive MIANC system is proposed. It uses online path estimates to cancel feedback, recover reference signal, and optimize a stable controller in the minimum H_2 norm sense, without any forms of persistent excitations. Theoretical analysis and experimental results are presented to demonstrate the stable control performance of the proposed system.

1. INTRODUCTION

Most active noise control (ANC) systems are model dependent. Let $\hat{P}(z)$ and $\hat{S}(z)$ denote estimates of primary and secondary path transfer functions $P(z)$ and $S(z)$. Either $\hat{S}(z)$ or both $\hat{P}(z)$ and $\hat{S}(z)$ must be obtained by initial system identification for model-dependent ANC systems. Controller transfer function $C(z)$ of a model-dependent ANC system is either designed by minimizing $\|\hat{P}(z)+\hat{S}(z)C(z)\|$, or adapted with the aid of $\hat{S}(z)$ [1, 2]. If estimates $\hat{P}(z)$ and $\hat{S}(z)$ contain too much error, a model-dependent ANC system may generate constructive instead of destructive interference. This is mathematically equivalent to $\|P(z) + S(z)C(z)\| > \|P(z)\|$ even if $\|\hat{P}(z) + \hat{S}(z)C(z)\|$ is minimized. If phase error in $\hat{S}(z)$ exceeds 90° in some frequency, an ANC system adapted by the filtered-X least mean square (FXLMS) algorithm may become unstable [3–5]. An operator of a model-dependent ANC system must have the knowledge and skill to obtain accurate estimates of path models by initial system identification for each individual application.

During the operation of an ANC system, changes of environmental or boundary conditions may cause significant changes to path transfer functions $P(z)$ and $S(z)$. Since a model-dependent ANC system only remembers initial path estimates $\hat{P}(z)$ and $\hat{S}(z)$, variation of $P(z)$ and $S(z)$ may cause mismatch with initial estimates $\hat{P}(z)$ and $\hat{S}(z)$ to degrade ANC performance. In cases of severe mismatch between path transfer functions and their initial estimates, a model-dependent ANC system may generate constructive instead of destructive interference, or even become unstable.

Model-independent ANC (MIANC) systems depend on online path modeling or invariant properties of sound fields to update or design controllers [6–8]. These systems avoid initial path modeling and are adaptive to variations of environmental or boundary conditions of sound fields. Many adaptive MIANC systems require invasive persistent excitations to obtain accurate path estimates and ensure closed-loop stability [6, 7, 9, 10]. Noninvasive MIANC systems are able to ensure closed-loop stability without persistent excitations, which are possible by a recently developed algorithm, known as orthogonal adaptation [11, 12], if the primary noise signal is directly available as the reference signal.

In many real applications, the primary noise signal is not necessarily available and the reference signal must be recovered from the sound field [1, 2]. When an ANC system is

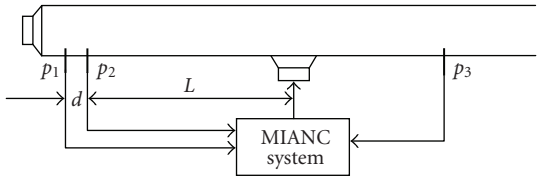

Figure 1: Configuration of the proposed MIANC system.

active, a measured signal is a linear combination of primary and secondary signals. Feedback of ANC signal in the measurement is mathematically modeled by a feedback transfer function $F(z)$ from the controller to the reference sensor. Accurate estimation of $F(z)$ is as important as accurate estimation of $P(z)$ or $S(z)$ [9, 13]. A complete noninvasive MIANC (CNMIANC) system must be able to suppress the noise signal without injecting probing signals for online modeling of $P(z)$, $S(z)$, and $F(z)$. Most available methods for adaptive feedback cancellation require persistent excitations [9, 13]. In this study, a new method is presented for adaptive feedback cancellation without persistent excitations.

It was proposed to use a pair of sensors to measure pressure signals in ducts, from which traveling waves are resolved [14, 15]. The outbound wave could be used directly as the reference signal without cancelling feedback signals if an infinite-impulse-response (IIR) controller could be implemented accurately [14, 15]. In reality, it is very difficult to implement a stable ideal IIR ANC controller [16]. Most practical ANC systems use finite-impulse-response (FIR) controllers. The outbound wave in a duct is a linear combination of primary noise and reflected version of feedback signal. Instead of using the outbound wave directly as the reference, the least mean square (LMS) algorithm is applied in this study to cancel feedback signals in the outbound wave before using it as the reference. Orthogonal adaptation is combined with the proposed ANC configuration to implement a CNMIANC system. Experimental result is presented to demonstrate the performance of the CNMIANC system.

2. SYSTEM CONFIGURATION AND MODEL

Figure 1 illustrates the configuration of the proposed ANC system. The primary source is represented by the upstream speaker and the secondary source is the midstream speaker. Cross-sectional area of the duct is small enough such that sound field in the duct can be modeled by a 1D sound field in the frequency range of interest. Three microphone sensors are installed in the duct, measuring signals p_1, p_2, and p_3, respectively. Since the primary noise signal is not available to the ANC system, the reference signal is recovered from p_1 and p_2, while p_3 is the error signal to be minimized by the ANC system.

Let d denote the axial distance between p_1 and p_2. The acoustical two-port theory [16, 17] has been applied by many ANC researchers for the design and analysis of ANC systems. It is adopted here as an analytical tool. An equivalent acoustical circuit is shown in Figure 2 to model the two-microphone system. The upstream part, from the primary source to location of p_1, is equivalent to an acoustical source with strength u_p and impedance Z_p. The downstream part, from location of p_2 to the outlet, is represented by another acoustical source with strength u_s and impedance Z_s. Characteristic impedance of the duct is represented by Z_o.

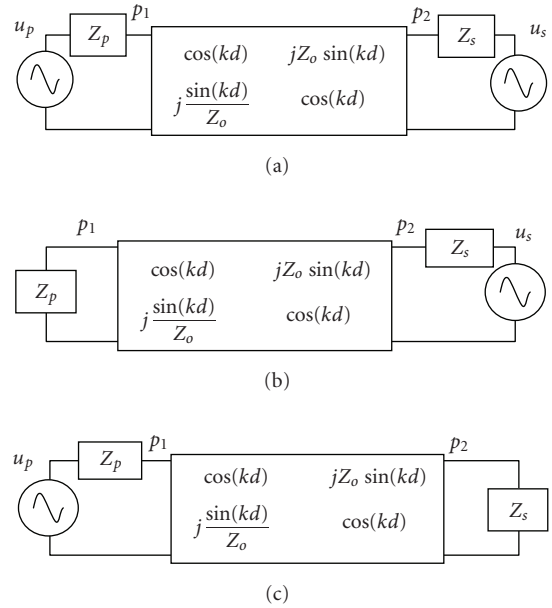

Figure 2: (a) Acoustical two-port circuit in the duct system, (b) contribution by controller, and (c) contribution by primary source.

The linear system theory allows one to solve p_1 and p_2 in Figure 2(a) by focusing on acoustical circuits of Figures 2(b) and 2(c) before adding two solutions together as the final solution of Figure 2(a). For the case of $u_p = 0$, which is represented by Figure 2(b), one obtains

$$\begin{aligned} p_2|_{u_p=0} &= \left[\cos(kd) + j\frac{Z_o}{Z_p}\sin(kd)\right] p_1|_{u_p=0}, \\ u_s - p_2|_{u_p=0} &= \left[\frac{Z_s}{Z_p}\cos(kd) + j\frac{Z_s}{Z_o}\sin(kd)\right] p_1|_{u_p=0}, \end{aligned} \tag{1}$$

where k is the wave number. One can solve, from (1),

$$p_2|_{u_p=0} = \frac{Z_o[Z_p\cos(kd) + jZ_o\sin(kd)]}{(Z_s+Z_p)Z_o\cos(kd) + j(Z_sZ_p + Z_o^2)\sin(kd)} u_s, \tag{2}$$

$$p_1|_{u_p=0} = \frac{Z_oZ_p}{(Z_s+Z_p)Z_o\cos(kd) + j(Z_sZ_p + Z_o^2)\sin(kd)} u_s. \tag{3}$$

Similarly, for the case of $u_s = 0$, which is represented by Figure 2(c), one obtains

$$\begin{aligned} p_1|_{u_s=0} &= \left[\cos(kd) + j\frac{Z_o}{Z_p}\sin(kd)\right] p_2|_{u_s=0}, \\ u_p - p_1|_{u_s=0} &= \left[\frac{Z_p}{Z_s}\cos(kd) + j\frac{Z_p}{Z_o}\sin(kd)\right] p_2|_{u_s=0}, \end{aligned} \tag{4}$$

from which one can solve

$$p_1|_{u_s=0} = \frac{Z_o[Z_s\cos(kd) + jZ_o\sin(kd)]}{(Z_s+Z_p)Z_o\cos(kd) + j(Z_sZ_p+Z_o^2)\sin(kd)}u_p, \tag{5}$$

$$p_2|_{u_s=0} = \frac{Z_oZ_s}{(Z_s+Z_p)Z_o\cos(kd) + j(Z_sZ_p+Z_o^2)\sin(kd)}u_p. \tag{6}$$

Adding (2) and (6), one may write

$$\begin{aligned} p_2 &= p_2|_{u_p=0} + p_2|_{u_s=0} \\ &= \frac{Z_o[Z_p\cos(kd) + jZ_o\sin(kd)]u_s + Z_oZ_su_p}{(Z_s+Z_p)Z_o\cos(kd) + j(Z_sZ_p+Z_o^2)\sin(kd)}. \end{aligned} \tag{7}$$

The same method is applicable to (3) and (5) for

$$\begin{aligned} p_1 &= p_1|_{u_p=0} + p_1|_{u_s=0} \\ &= \frac{Z_o[Z_s\cos(kd) + jZ_o\sin(kd)]u_p + Z_oZ_pu_s}{(Z_s+Z_p)Z_o\cos(kd) + j(Z_sZ_p+Z_o^2)\sin(kd)}. \end{aligned} \tag{8}$$

The next step is to use complex factor $\alpha = Z_o/((Z_s + Z_p)Z_o\cos(kd) + j(Z_sZ_p + Z_o^2)\sin(kd))$ to simplify (7) and (8). The results read

$$\begin{aligned} p_2 &= \alpha\{[Z_p\cos(kd) + jZ_o\sin(kd)]u_s + Z_su_p\}, \\ p_1 &= \alpha\{[Z_s\cos(kd) + jZ_o\sin(kd)]u_p + Z_pu_s\}. \end{aligned} \tag{9}$$

Since $\cos(kd) = 0.5(e^{jkd} + e^{-jkd})$ and $j\sin(kd) = 0.5(e^{jkd} - e^{-jkd})$, (9) can be written as

$$\begin{aligned} p_2 &= \alpha\left\{\left[\frac{Z_p+Z_o}{2}e^{jkd} + \frac{Z_p-Z_o}{2}e^{-jkd}\right]u_s \right. \\ &\qquad \left. + \left[\frac{Z_s+Z_o}{2} + \frac{Z_s-Z_o}{2}\right]u_p\right\}, \\ p_1 &= \alpha\left\{\left[\frac{Z_s+Z_o}{2}e^{jkd} + \frac{Z_s-Z_o}{2}e^{-jkd}\right]u_p \right. \\ &\qquad \left. + \left[\frac{Z_p+Z_o}{2} + \frac{Z_p-Z_o}{2}\right]u_s\right\}. \end{aligned} \tag{10}$$

Let

$$w_i = \alpha\left\{\frac{Z_s-Z_o}{2}u_p + \frac{Z_p+Z_o}{2}e^{jkd}u_s\right\} \tag{11}$$

$$w_o = \alpha\left\{\frac{Z_p-Z_o}{2}u_s + \frac{Z_s+Z_o}{2}e^{jkd}u_p\right\} \tag{12}$$

represent the in- and outbound waves in the duct. By comparing (10) with (11) and (12), one can see that (10) are equivalent to

$$p_2 = w_i + w_oe^{-jkd}, \qquad p_1 = w_ie^{-jkd} + w_o. \tag{13}$$

The in- and outbound waves can be resolved from p_1 and p_2 via

$$\begin{aligned} \begin{bmatrix} w_i \\ w_o \end{bmatrix} &= \begin{bmatrix} e^{-jkd} & 1 \\ 1 & e^{-jkd} \end{bmatrix}^{-1} \begin{bmatrix} p_1 \\ p_2 \end{bmatrix} \\ &= \frac{1}{1-e^{-2jkd}} \begin{bmatrix} -e^{-jkd} & 1 \\ 1 & -e^{-jkd} \end{bmatrix} \begin{bmatrix} p_1 \\ p_2 \end{bmatrix}. \end{aligned} \tag{14}$$

In a digital implementation of ANC system, it is recommended to select sampling interval δt such that its product with sound speed c satisfies $c\delta t = d$. As a result, the delay operator $\exp(-jkd) = z^{-1}$ becomes an exact one-sample delay for discrete-time ANC systems.

3. FEEDBACK CANCELLATION

It is indicated by (12) that the outbound wave contains feedback from u_s that must be cancelled to recover the reference signal. Let $R_1 = (Z_p - Z_o)/(Z_p + Z_o)$ denote the upstream reflection coefficient. By multiplying $e^{-jkd}R_1$ to (11), one obtains

$$e^{-jkd}R_1w_i = \alpha\left\{\frac{(Z_s-Z_o)(Z_p-Z_o)}{2(Z_p+Z_o)}e^{-jkd}u_p + \frac{Z_p-Z_o}{2}u_s\right\}. \tag{15}$$

A subtraction of (15) from (12) enables one to write

$$w_o - e^{-jkd}R_1w_i = n, \tag{16}$$

where

$$n = \frac{\alpha[(Z_s+Z_o)(Z_p+Z_o)e^{jkd} - (Z_s-Z_o)(Z_p-Z_o)e^{-jkd}]}{2(Z_p+Z_o)}u_p \tag{17}$$

is only contributed by the primary source u_p.

Using $\cos(kd) = 0.5(e^{jkd} + e^{-jkd})$ and $j\sin(kd) = 0.5(e^{jkd} - e^{-jkd})$, one can see that the common denominator of p_1, p_2, and all transfer functions in the duct is

$$\begin{aligned} &(Z_s+Z_p)Z_o\cos(kd) + j(Z_sZ_p+Z_o^2)\sin(kd) \\ &\quad = 0.5(Z_s+Z_o)(Z_p+Z_o)e^{jkd} - 0.5(Z_s-Z_o)(Z_p-Z_o)e^{-jkd}. \end{aligned} \tag{18}$$

Substituting (18) into the definition of α (immediately after (8)), one obtains

$$2Z_o = \alpha[(Z_s+Z_o)(Z_p+Z_o)e^{jkd} - (Z_s-Z_o)(Z_p-Z_o)e^{-jkd}]. \tag{19}$$

A further substitution of (19) into (17) leads to

$$n = \frac{Z_ou_p}{Z_p+Z_o}. \tag{20}$$

This is the reference signal to be recovered by the proposed ANC system.

A question to be answered here is why not recovering the reference signal from a pressure signal such as p_1. The hint is (8) that may be expressed as $p_1 = F(j\omega)u_s + B(j\omega)u_p$. In view of (8), the acoustical feedback transfer function is

$$F(j\omega) = \frac{Z_oZ_p}{(Z_s+Z_p)Z_o\cos(kd) + j(Z_sZ_p+Z_o^2)\sin(kd)}. \tag{21}$$

Since $F(j\omega)$ is a transfer function with resonant poles, it has an infinite impulse response (IIR). In many ANC systems, a

finite-impulse-response (FIR) filter $\hat{F}(j\omega)$ is used to approximate $F(j\omega)$. This means inevitable approximation errors in the first place.

Besides, all transfer functions in a duct are sensitive to values of Z_o, Z_s, and Z_p. In particular, Z_s is the impedance of the entire downstream segment from the location of p_2 to the duct outlet. Objects moving near the duct outlet could cause changes of Z_s. A fracture in any downstream part may also cause a significant change to Z_s as well. If initial estimate $\hat{F}(j\omega)$ is remembered by an ANC system, it is a stability issue how significant will $F(j\omega) - \hat{F}(j\omega)$ turn out as a result of a small variation of Z_s. An indicative answer might be

$$\frac{\partial}{\partial Z_s}F(j\omega) = \frac{-Z_oZ_p[Z_o\cos(kd) + jZ_p\sin(kd)]}{[(Z_s+Z_p)Z_o\cos(kd) + j(Z_sZ_p+Z_o^2)\sin(kd)]^2}. \tag{22}$$

The common denominator of p_1, p_2, and all transfer functions in the duct has an alternative form in (18), which is equivalent to

$$\begin{aligned} &0.5(Z_s+Z_o)(Z_p+Z_o)e^{jkd} - 0.5(Z_s-Z_o)(Z_p-Z_o)e^{-jkd} \\ &\quad = 0.5(Z_s+Z_o)(Z_p+Z_o)e^{jkd}\left[1-\frac{(Z_s-Z_o)(Z_p-Z_o)}{(Z_s+Z_o)(Z_p+Z_o)}e^{-2jkd}\right] \\ &\quad = 0.5(Z_s+Z_o)(Z_p+Z_o)e^{jkd}[1-R_1R_2e^{-2jkd}], \end{aligned} \tag{23}$$

where $R_2 = (Z_s - Z_o)/(Z_s + Z_o)$ represents the downstream reflection coefficient.

Since resonant frequencies of the duct are roots of the common denominator, it is suggested by (22) and (23) that all transfer functions in the duct, including the feedback transfer function $F(j\omega)$, are sensitive to variance of Z_s at the resonant peaks. The stronger the resonance, the more sensitive of transfer functions with respect to Z_s. If an ANC system recovers the reference signal from a pressure signal like p_1, a small online variation of Z_s may cause a significant mismatch between $F(j\omega)$ and initial estimate $\hat{F}(z)$. As a result, closed-loop stability is sensitive to possible variation of Z_s.

If the reference signal is recovered from traveling waves with (16), the situation will be different. In a discrete-time implementation, one may rewrite (16) to $n(z) = w_o - F_w(z)w_i$, where the acoustical feedback transfer function is a delayed version of upstream reflection coefficient $F_w(z) = z^{-1}R_1(z)$. Here, $R_1 = (Z_p - Z_o)/(Z_p + Z_o)$ is only sensitive to Z_p and Z_o. Characteristic impedance Z_o is a real constant depending on sound speed and cross-sectional area between p_1 and p_2. It seldom changes significantly in online ANC operations. As for Z_p, it is the impedance of the upstream portion from the primary source to the location of p_1. In most applications, p_1 and p_2 are measured as close as possible to the primary source. Impedance Z_p is deeply hidden in a very short segment of the duct. Its variation, if any, would be certainly not as significant as that of Z_s.

No matter how significant are the possible variations of Z_p or Z_o, the passive upstream reflection always has a limited magnitude $|R_1| < 1$. For each pair of fixed Z_p and Z_o, $|R_1(j\omega)|$ does not have sharp peaks or dips as a function of ω. In many cases, $|R_1|$ is constant for a pair of fixed Z_p and Z_o. Let $X(j\omega)$ denote the Fourier transform of $x(t)$, then $X(j\omega) = L\{x(t)\}$ and $x(t) = L^{-1}\{X(j\omega)\}$ share many similar properties. For example, if $x(t)$ is a low-frequency function of t, then the bandwidth of $X(j\omega)$ is narrow in terms of ω. Similarly, if $X(j\omega)$ is a "low-frequency" function of ω, then the time duration of $x(t)$ is short (a narrow bandwidth in terms of t). The fact that $|R_1|$ is a "low-frequency" function of ω for each pair of fixed Z_p and Z_o implies short impulse responses of $R_1(z)$. It is, therefore, reasonable to assume that $R_1(z) = \sum_{k=0}^{m} r_k z^{-k}$ can be approximated by a FIR transfer function with negligible errors (Assumption A1). If both Z_p and Z_o are constant, R_1 is a single constant. Resonant effects in the duct are hidden in wave signals w_i and w_o without affecting R_1. This is a major difference between recovering the reference signal from traveling waves and recovering the reference signal from a pressure signal.

Even if an estimate of $F_w(z)$ is obtained by initial identification, it is less likely that online variations of environmental or boundary conditions could cause significant mismatch between $F_w(z)$ and its initial estimate. The resultant ANC system is semimodel independent if its reference signal is recovered with (16) in combination with a MIANC adaptation algorithm such as orthogonal adaptation.

4. COMPLETE NONINVASIVE MIANC

Noninvasive model-independent feedback cancellation is possible by applying LMS to (16). With assumption A1, online estimate of the feedback transfer function is represented by polynomial

$$\hat{R}(z) = \sum_{k=0}^{m} \hat{r}_k(t)z^{-k}, \tag{24}$$

where $r_k(t)$ is the kth coefficient for the tth sample. An estimated version of (16) would be

$$\hat{n} = w_o - z^{-1}\hat{R}(z)w_i, \tag{25}$$

which has a discrete-time domain expression,

$$\hat{n}(t) = w_o(t) - \sum_{k=0}^{m} \hat{r}_k(t)w_i(t-k-1). \tag{26}$$

Coefficients of $\hat{R}(z) = \sum_{k=0}^{m} \hat{r}_k(t)z^{-k}$ are updated with the LMS algorithm as follows:

$$\hat{r}_k(t+1) = \hat{r}_k(t) + \mu\hat{n}(t)w_i(t-k-1), \tag{27}$$

where $\mu > 0$ is a small constant representing the LMS step size. Since $R_1(z) = \sum_{k=0}^{m} r_k z^{-k}$ by assumption A1, the discrete-time domain version of (16) is

$$n(t) = w_o(t) - \sum_{k=0}^{m} r_k w_i(t-k-1). \tag{28}$$

Subtracting (28) from (27), one obtains

$$\begin{aligned}\hat{n}(t) - n(t) &= \sum_{k=0}^{m} [r_k - \hat{r}_k(t)] w_i(t-k-1) \\ &= \sum_{k=0}^{m} \Delta r_k(t) w_i(t-k-1),\end{aligned} \tag{29}$$

where $\Delta r_k(t) = r_k - \hat{r}_k(t)$ is the estimation error of r_k. Let $\Delta r = [\Delta r_0, \Delta r_1, \ldots, \Delta r_m]^T$ and let $\varpi_i(t) = [w_i(t-1), w_i(t-2), w_i(t-m-1)]^T$. It is possible to express (29) in an inner product

$$\hat{n}(t) - n(t) = \Delta r^T \varpi_i(t). \tag{30}$$

Estimation residues of LMS algorithms are usually expressed as inner products like (30). It has been proven that the LMS algorithm is able to drive the convergence of these inner products towards zero.

If the primary noise signal u_p was available, mathematical model of the error signal may be expressed in the discrete-time z-transform domain as $e(z) = P(z)u_p(z) + S(z)u_s(z)$, where the actuation signal would be synthesized as $u_s(z) = C(z)u_p(z)$. Since u_p is actually not available, the ANC system has to recover $\hat{n}(z)$ from the outbound wave and then synthesize $u_s(z) = C(z)\hat{n}(z)$ instead. After the convergence of $\hat{n}(z) \to n(z)$, one may express the mathematical model of the error signal to

$$e(z) = \left\{ P(z)\left[1 + \frac{Z_p}{Z_o}\right] + S(z)C(z) \right\} n(z), \tag{31}$$

where (20) has been substituted. Let $H(z) = P(z)[1 + Z_p/Z_o]$, then (31) becomes

$$e(z) = [H(z) + S(z)C(z)]n(z). \tag{32}$$

It is mathematically equivalent to another ANC system whose primary source is available to the controller as $n(z)$, with primary path transfer function $H(z)$ and secondary path transfer function $S(z)$. Orthogonal adaptation is readily applicable to (32) to implement a noninvasive MIANC system.

It is assumed that $H(z)$ and $S(z)$ can be approximated by FIR filters with negligible errors (Assumption A2). Let $h^T = [h_0 \ h_1 \ \cdots \ h_m]$ and $s^T = [s_0 \ s_1 \ \cdots \ s_m]$ denote coefficients of $H(z)$ and $S(z)$, respectively, the discrete-time domain version of $e(z) = H(z)n(z) + S(z)u_s(z)$ is a discrete-time convolution:

$$e(t) = \sum_{k=0}^{m} h_k n(t-k) - \sum_{k=0}^{m} s_k u_s(t-k), \tag{33}$$

where $e(t)$, $n(t)$, and $u_s(t)$ denote samples of $e(z)$, $n(z)$, and $u_s(z)$, respectively. Introducing coefficient vector $\theta^T = [h^T \ s^T]$ and regression vector $\phi_t = [n(t) \ n(t-1) \cdots n(t-m), \ u_s(t) \ u_s(t-1) \cdots u_s(t-m)]^T$, one may rewrite (33) to

$$e(t) = \theta^T \phi_t. \tag{34}$$

Let $\hat{H}(z)$ and $\hat{S}(z)$ denote online estimates of $H(z)$ and $S(z)$. Path estimates $\hat{H}(z)$ and $\hat{S}(z)$ are obtained by minimizing estimation error as follows:

$$\varepsilon(z) = e(z) - \hat{H}(z)n(z) - \hat{S}(z)u_s(z) = \Delta H(z)n(z) + \Delta S(z)u_s(z), \tag{35}$$

where $\Delta H(z) = H(z) - \hat{H}(z)$ and $\Delta S(z) = S(z) - \hat{S}(z)$ are online modeling errors. Let $\hat{\theta}^T = [\hat{h}^T \ \hat{s}^T]$ denote online estimate of $\theta^T = [h^T \ s^T]$, then $\hat{h}^T = [\hat{h}_0 \ \hat{h}_1 \ \cdots \ \hat{h}_m]$ and $\hat{s}^T = [\hat{s}_0 \ \hat{s}_1 \ \cdots \ \hat{s}_m]$ represent the coefficients of $\hat{H}(z)$ and $\hat{S}(z)$, respectively. Similar to the equivalence between (34) and $e(z) = H(z)n(z) + S(z)u_s(z)$, (35) has a discrete-time domain equivalence

$$\varepsilon_t = e(t) - \hat{\theta}^T \phi_t = \Delta \hat{\theta}^T \phi_t, \tag{36}$$

where $\Delta\theta = \theta - \hat{\theta}$ is the online coefficient error vector. The entire CNMIANC system performs three online tasks that are mathematically represented by the minimization of three inner products. The first is inner product given in (30); the second one is given in (36); and the third one is $\hat{\theta}^T \phi_t$.

Equations (30) and (36) contain estimation errors Δr and $\Delta\theta$. Most available estimation algorithms, such as LMS and the recursive least squares (RLS), are very capable of driving inner products like (30) and (36) towards zero, or at least minimizing their magnitudes [18]. A difficult problem is how to force $\Delta r \to 0$ and $\Delta\theta \to 0$. Available solutions inject significant levels of "persistent excitations" (invasive probing signals) to the estimation system [6, 7, 9, 10, 13]. A unique feature of the proposed CNMIANC is no persistent excitations. The system works well without requiring $\Delta r \to 0$ and $\Delta\theta \to 0$.

For (30), minimizing the inner product in the right-hand side implies convergence of $\hat{n} \to n$ in the left-hand side. It would be great if $\Delta r \to 0$ as well. Otherwise, Δr may just converge to a FIR filter that filters out w_i from w_o. On the other hand, minimizing the inner product in (36) only implies $\varepsilon_t \to 0$. The question is what does it further implies? One may consider the equivalence between (34) and $e(z) = H(z)n(z) + S(z)u_s(z)$, which holds if one replaces $\theta^T = [h^T \ s^T]$, $H(z)$, and $S(z)$ with respective estimates $\hat{\theta}^T = [\hat{h}^T \ \hat{s}^T]$, $\hat{H}(z)$, and $\hat{S}(z)$. The equivalence is now between forcing $\hat{\theta}^T \phi_t \approx 0$ and forcing

$$\hat{H}(z)n(z) + \hat{S}(z)u_s(z) = [\hat{H}(z) + \hat{S}(z)C(z)]n(z) \approx 0. \tag{37}$$

The CNMIANC system uses online estimates of $\hat{H}(z)$ and $\hat{S}(z)$ to solve $C(z)$ that minimizes $\|\hat{H}(z) + \hat{S}(z)C(z)\|_2$. This is equivalent to forcing $\hat{\theta}^T \phi_t \approx 0$. One can obtain

$$\|e\| = \|\varepsilon_t + \hat{\theta}^T \phi_t\| \le \|\varepsilon_t\| + \|\hat{\theta}^T \phi_t\| \tag{38}$$

by adding $\hat{\theta}^T \phi_t$ to both sides of (36). As the CNMIANC system drives $\varepsilon_t = \Delta\hat{\theta}^T \phi_t \to 0$ and forces $|\hat{\theta}^T \phi_t| \approx 0$ ultimately, it implies ultimate convergence of $\|e\| \to 0$ even though $\Delta\theta$ does not necessarily converge to zero [11, 12].

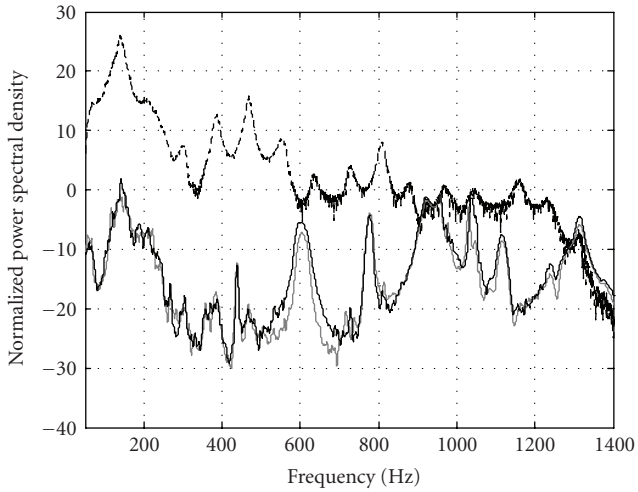

FIGURE 3: Normalized PSDs of $e(t)$ for (a) uncontrolled case (dashed-black), (b) controlled case with $u_p(t)$ available (solid-gray), and (c) controlled case with recovered $\hat{n}(t)$ (solid-black).

5. EXPERIMENTAL VERIFICATION

A CNMIANC system was implemented and tested in an experiment, with a configuration shown in Figure 1. Cross-sectional area of the duct was $12 \times 15\,\text{cm}^2$. Two microphones were placed 30 cm downstream from the primary speaker with a space of $d = 10\,\text{cm}$ between p_1 and p_2. The distance between p_2 and the secondary speaker is represented by L in Figure 1. To guarantee a causal ANC system, the value of L must satisfy $L > 2d$ such that the outbound wave is at least two samples ahead of sound propagation in duct. The sampling interval of the controller was 0.29 millisecond with a sampling frequency of 3.448 Hz, which satisfies $d = c\delta t$ with $c = 344\,\text{m/s}$ and $\exp(jkd) = z$. The cutoff frequency of antialias filters was chosen to be 1200 Hz. The in- and outbound waves were recovered from pressure signals with (14). The reference signal was recovered with (25). Coefficients of $\hat{R}(z)$ were adapted with (27). Another online modeling process used (34) to obtain coefficients of $\hat{H}(z)$ and $\hat{S}(z)$. The ANC transfer function was solved by online minimization of $\|\hat{H}(z) + \hat{S}(z)C(z)\|_2$. The CNMIANC system was implemented in a dSPACE 1103 board.

Error signal $e(t)$ and primary noise $u_p(t)$ were collected as vectors e and u_p for three cases. In case 1, there was no control action. In case 2, $u_p(t)$ was available as the reference signal for an ANC system to suppress noise in the duct. In case 3, $u_p(t)$ was not available and the CNMIANC system had to recover $\hat{n}(t)$ from p_1 and p_2 for controller synthesis. For each respective case, power spectral densities (PSD's) of $e(t)$ and $u_p(t)$ were computed with a MATLAB command called "pmtm()". Computational results are denoted as vectors $P_e = \text{pmtm}(e)$ and $P_p = \text{pmtm}(\text{u}_\text{p})$, where argument vectors e and u_p represent measurement samples of $e(t)$ and $u_p(t)$. The normalized PSD of $e(t)$ was calculated as $P_{ne} = 10\log(P_e/P_p)$ for all three cases.

Shown in Figure 3 are normalized PSD of $e(t)$ for the three cases. For case 1, normalized PSD of $e(t)$ is represented by the dashed-black curve. For case 2, normalized PSD of $e(t)$ is plotted with the solid-gray curve. For case 3, normalized PSD of $e(t)$ is represented by the solid-black curve. Both ANC systems were able to suppress noise with good control performance as seen in Figure 3. The proposed CNMIANC has slightly worse performance since its reference was the recovered signal $\hat{n}(t)$ instead of the true primary source $u_p(t)$. This is a small price to pay in case $u_p(t)$ is not available to the ANC system. The proposed CNMIANC system was stable and able to recover the reference and suppress noise without any persistent excitations.

The CNMIANC system was robust with respect to sudden parameter change in the duct. In the experiment, the duct outlet was changed from completely open to completely closed. Such a sudden change shifted all resonant frequencies in the duct. Path transfer functions also changed suddenly. The CNMIANC system remained stable and converged very quickly.

6. CONCLUSIONS

The primary source is not necessarily available as the reference signal for ANC systems in all practical applications. When the primary source is not available, the ANC system must recover the reference signal from a sound field to which ANC is applied. Feedback cancellation is an important issue in ANC systems that recover reference signals from sound fields. In most MIANC systems, persistent excitations are required for online modeling of feedback path model and adaptive feedback cancellation [9, 13]. In this study, a CNMIANC system is proposed that recovers reference signal from traveling waves without persistent excitations. The corresponding feedback path model is the upstream reflection coefficient and hence closer to an FIR filter than pressure feedback transfer functions (IIR path models in resonant ducts). Theoretical analysis and experimental results are presented to demonstrate the stable operation of the proposed CNMIANC system.

REFERENCES

[1] C. H. Hansen and S. D. Snyder, *Active Control of Noise and Vibration*, E & FN Spon, London, UK, 1997.

[2] P. A. Nelson and S. J. Elliott, *Active Control of Sound*, Academic Press, London, UK, 1992.

[3] M. A. Vaudrey, W. T. Baumann, and W. R. Saunders, "Stability and operating constraints of adaptive LMS-based feedback control," *Automatica*, vol. 39, no. 4, pp. 595–605, 2003.

[4] E. Bjarnason, "Analysis of the filtered-X LMS algorithm," *IEEE Transactions on Speech and Audio Processing*, vol. 3, no. 6, pp. 504–514, 1995.

[5] S. D. Snyder and C. H. Hansen, "The influence of transducer transfer functions and acoustic time delays on the implementation of the LMS algorithm in active noise control systems," *Journal of Sound and Vibration*, vol. 141, no. 3, pp. 409–424, 1990.

[6] L. J. Eriksson and M. C. Allie, "Use of random noise for online transducer modeling in an adaptive active attenuation system," *Journal of the Acoustical Society of America*, vol. 85, no. 2, pp. 797–802, 1989.

[7] M. Zhang, H. Lan, and W. Ser, "Cross-updated active noise control system with online secondary path modeling," *IEEE Transactions on Speech and Audio Processing*, vol. 9, no. 5, pp. 598–602, 2001.

[8] R. L. Clark and D. G. Cole, "Active damping of enclosed sound fields through direct rate feedback control," *Journal of the Acoustical Society of America*, vol. 97, no. 3, pp. 1710–1716, 1995.

[9] X. Qiu and C. H. Hansen, "An algorithm for active control of transformer noise with on-line cancellation path modelling based on the perturbation method," *Journal of Sound and Vibration*, vol. 240, no. 4, pp. 647–665, 2001.

[10] M. Zhang, H. Lan, and W. Ser, "A robust online secondary path modeling method with auxiliary noise power scheduling strategy and norm constraint manipulation," *IEEE Transactions on Speech and Audio Processing*, vol. 11, no. 1, pp. 45–53, 2003.

[11] J. Yuan, "Orthogonal adaptation for active noise control," *Journal of the Acoustical Society of America*, vol. 120, no. 1, pp. 204–210, 2006.

[12] J. Yuan, "Orthogonal adaptation for multichannel feedforward control," *Journal of the Acoustical Society of America*, vol. 120, no. 6, pp. 3723–3729, 2006.

[13] M. T. Akhtar, M. Abe, and M. Kawamata, "On active noise control systems with online acoustic feedback path modeling," *IEEE Transactions on Audio, Speech and Language Processing*, vol. 15, no. 2, pp. 593–600, 2007.

[14] J.-S. Hu, "Feedforward and feedback control strategy for active noise cancellation in ducts," *Journal of Dynamic Systems, Measurement and Control*, vol. 118, no. 2, pp. 372–378, 1996.

[15] J.-S. Hu, "Active sound attenuation in finite-length ducts using close-form transfer function models," *Journal of Dynamic Systems, Measurement and Control*, vol. 117, no. 2, pp. 143–154, 1995.

[16] M. R. Bai, Y. Lin, and J.-D. Wu, "Analysis and DSP implementation of a broadband duct ANC system using spatially feedforward structure," *Journal of Vibration and Acoustics*, vol. 123, no. 2, pp. 129–136, 2001.

[17] M. L. Munjal and L. J. Eriksson, "An analytical, one-dimensional, standing-wave model of a linear active noise control system in a duct," *Journal of the Acoustical Society of America*, vol. 84, pp. 1066–1093, 1988.

[18] G. C. Goodwin and K. S. Sin, *Adaptive Filtering, Prediction and Control*, Prentice-Hall, Englewood Cliffs, NJ, USA, 1984.

Hindawi Publishing Corporation
Advances in Acoustics and Vibration
Volume 2008, Article ID 253948, 8 pages
doi:10.1155/2008/253948

Research Article

Active Noise Cancellation for Ventilation Ducts Using a Pair of Loudspeakers by Sampled-Data $\mathcal{H}_\infty$ Optimization

Yasuhide Kobayashi[1] and Hisaya Fujioka[2]

[1] *Department of Mechanical Engineering, Faculty of Engineering, Nagaoka University of Technology, Nagaoka, Niigata 940-2188, Japan*
[2] *Department of Applied Analysis and Complex Dynamical Systems, Graduate School of Informatics, Kyoto University, Kyoto 606-8501, Japan*

Correspondence should be addressed to Yasuhide Kobayashi, kobayasi@vos.nagaokaut.ac.jp

Received 2 December 2007; Accepted 14 March 2008

Recommended by Marek Pawelczyk

We deal with the design of active noise control systems for ventilation ducts with a pair of loud-speakers based on sampled-data $\mathcal{H}_\infty$ optimization, in order to improve our previous study with a single loudspeaker. The resultant controller requires lower computational complexity for the implementation, compared to the standard time-varying adaptive controllers, since it is time-invariant and the order is comparable. Moreover, the effect of Swinbanks' source is automatically recovered by the $\mathcal{H}_\infty$ optimization. The benefit of the proposed method is also confirmed from experimental results for a real house, where the achieved noise attenuation level is about twice as much as that of the single loudspeaker case.

1. INTRODUCTION

Active noise cancellation (ANC) is to attenuate noise by the same sound but opposite phase. This technique has been practically used in air conditioning systems in large-scale buildings, aircraft cabins, and so on [1]. However, there are many fields such as ventilation ducts for small buildings where ANC is desired but has not been applied yet because the conventional adaptive algorithms for ANC require expensive implementation.

In the previous study [2], by assuming that temperature variation is small as in recent energy-efficient houses so that time-invariant controller can achieve sufficient performance, two types of time-invariant low-order controllers are compared: one is based on the conventional adaptive filter (the filtered-U recursive LMS algorithm) but the coefficients are fixed by the stationary values. Another is obtained by a robust control method (sampled-data $\mathcal{H}_\infty$ control). It has been shown that robust control design has advantage to implement inexpensive ANC system for ventilation ducts, because it gives a systematical way to design a controller which is robust against not only plant dynamics variation but also aliasing components of noise. However, further improvement of the sound attenuation is desired.

The method originally proposed by Swinbanks [3] is well known as an effective one for the improvement of the system performance, where an additional loudspeaker is attached to cancel out the upstream sound generated by a control source [4]. The method has been examined in detail under adaptive control setup [5]. However, the effect of Swinbanks' source under robust control setup has not been studied. Moreover, experimental results applied to actual ventilation systems installed in houses have not been reported.

In this paper, we examine robust control design of active noise control systems with a pair of loudspeakers in order to improve the system performance. By regarding the loudspeakers as two independent sources, a single-input-multiple-output (SIMO) controller is also designed to be compared with Swinbanks' source. The validity of robust control design is shown by experimental results using a ventilation duct installed in a real house.

It would be worth mentioning that there have been many studies that deal with the design problem for duct active noise control systems not only in the adaptive control framework [1, 6] but also in the robust control framework [7–10] under the simple duct setup, while the comparison of the adaptive and robust control with a real ventilation system has been firstly reported in [2]. Furthermore, robust

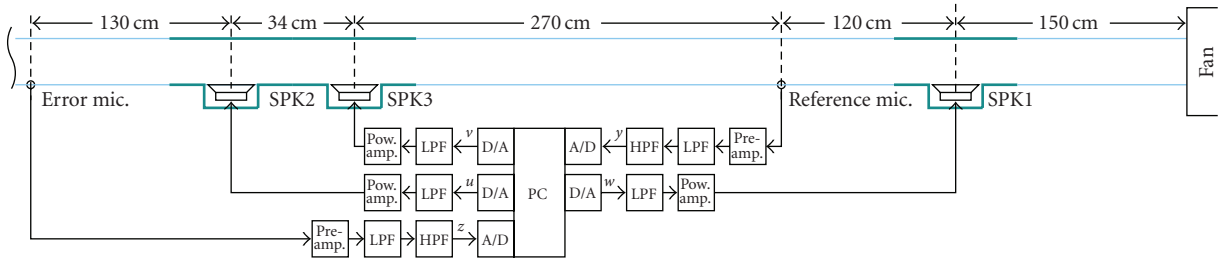

Figure 1: Experimental apparatus.

Table 1: Experimental instruments.

Ventilation fan	Kaneka corp. SV-200U (250 m^3/h, energy-recovery ventilation)
Loudspeaker (SPK1)	FOSTEX FW208N woofer speaker with wooden box enclosure
Loudspeaker (SPK2 & SPK3)	FOSTEX FW108N woofer speaker with PVC pipe enclosure
Microphones	Electlet condenser type
Sound-level meter	RION NL-20
Power amplifier	TOSHIBA TA8213K
High-pass filter	NF ELECTRONIC INSTRUMENTS FV-664 (2 ch, 80 Hz, 24 dB/oct)
Low-pass filter	500 Hz 4th-order Butterworth
PC	Dell Dimension 2200 (RT-Linux 3.2, kernel 2.4.22)
A/D, D/A	CONTEC AD12-16(PCI), DA12-4(PCI) (12 bit, ±5 V, 10 μs)

control system with Swinbanks' source has not been studied yet.

2. PROBLEM SETUP

Figure 1 and Table 1 show the block diagram and instalments of the experimental apparatus which are the same in [2] except that SPK3 and the corresponding D/A channel are attached so that Swinbanks' source is composed of the pair of loudspeakers, SPK2 and SPK3.

In addition, for simplicity of robust control design in this paper, SPK1 is used as a noise source in the modeling stage of robust control design to examine frequency response of the plant model, while in [2] actual fan noise is used.

Figure 2 shows the configuration of the ventilation system installed in a two-stored real house which is also the same as in [2]. The grilles are attached to the ceiling of each floor, and the ANC system is connected between fresh-air grilles and the ventilation fan.

In this paper, we examine the following cases to derive the control sources SPK2 and SPK3.

Case (a)—a single loudspeaker—by setting $v(t) = 0$, only SPK2 is used to generate control sound.

Case (b)—swinbanks' source [5]—by setting

$$v(t) = -u(t-\tau), \qquad \tau = \frac{d}{c_0}, \tag{1}$$

SPK3 is driven to cancel out the upstream sound generated by SPK2, where d is the distance between SPK2 and SPK3, and c_0 is the sound speed.

Case (c)—an array of two loudspeakers—by setting $v(t)$ free to $u(t)$, SPK2 and SPK3 are driven as independent sources.

Our primal motivation is to improve the performance by using a pair of loudspeakers (cases (b) and (c)) instead of a single loudspeaker (case (a)) in the robust control framework. In Swinbanks' source, the upstream loudspeaker is driven by a downstream one in an ad hoc way by (1). Hence our second motivation is to further improve the performance by giving more freedom to the upstream loudspeaker in case (c), although it has been reported in adaptive control framework that the performance is not improved if we replace the delay in case (b) by an adaptive filter to enlarge the design freedom [5].

In the experiments for case (b) below, (1) is approximately implemented as a real-time module of RTLinux that updates the signal $v(t)$ at every 0.1 millisecond which is considered to be short enough to avoid aliasing effect. In addition, by letting $d = 0.34$ m from Figure 1 and $c_0 = 344$ m/s from normal temperature environment, we use $\tau = 1$ millisecond which exactly corresponds to 10 times of the period of the real-time module mentioned above. Moreover, the cutoff frequency of HPF is determined by considering the frequency range of Swinbanks' source given as $[f_0, 5f_0]$, where $f_0 := d/12c_0$ [5]. The sampling period of controller is 1 millisecond throughout this paper.

3. ROBUST CONTROL DESIGN

The design procedure for case (a) is the same as in [10]. The detail of the design procedure for case (c) is omitted but it is

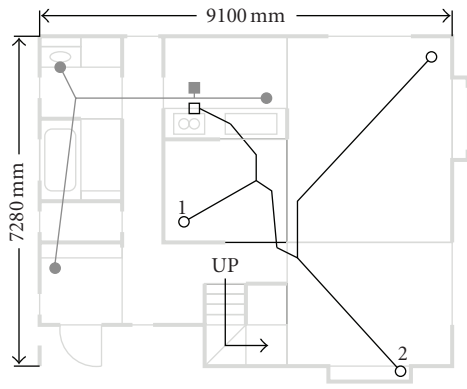

(a) 1st floor

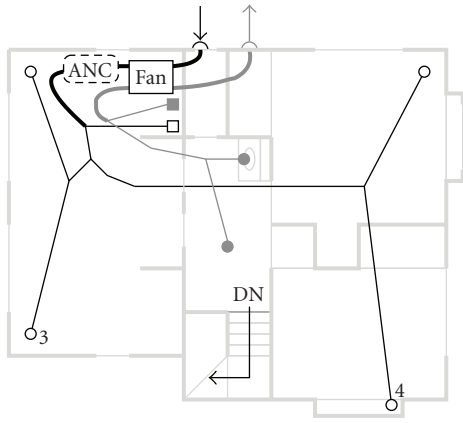

(b) 2nd floor

Figure 2: Ventilation system configuration.

done by simply replacing the signal $[\ u\ \ v\ ]^T$ to u to apply the design process of case (a).

3.1. Modeling

The plant models for Figure 1 are determined by frequency response experiment. The system from $[\ w\ \ u\ ]^T$ to $[\ z\ \ y\ ]^T$ is considered as the plant transfer function $G(s)$ for cases (a) and (b) as

$$G(s) := \begin{bmatrix} G_{zw}(s) & G_{zu}(s) \\ G_{yw}(s) & G_{yu}(s) \end{bmatrix}, \tag{2}$$

while for case (c) $G(s)$ is defined by

$$G(s) := \begin{bmatrix} G_{zw}(s) & G_{zu}(s) & G_{zv}(s) \\ G_{yw}(s) & G_{yu}(s) & G_{yv}(s) \end{bmatrix}, \tag{3}$$

where $G_{ab}(s)$ means the transfer function from the signal b to the signal a.

Figure 3 shows the frequency response of $G(s)$ and corresponding nominal plant obtained by subspace-based method where the order is 85. In the figures for $G_{zu}(s)$ and $G_{yu}(s)$, two frequency response results are shown in blue and yellow curves where the former corresponds to cases (a) and (c), while the latter corresponds to case (b). On the other hand, the frequency responses for $G_{zw}(s)$ and $G_{yw}(s)$ shown in blue curves are commonly used to determine nominal plant for all the cases.

In experimental results of case (a), the phase lag becomes larger in the order of G_{yw}, G_{zu}, G_{yu}, and G_{zw}, of which order coincides with that of the distance from corresponding microphone to speaker. In case (b), remarkable change on $G_{yu}(s)$ is observed compared with case (a): the gain is smaller in the whole frequency range, and the phase lag becomes larger, which can be considered as the result that the distance for sound traveling from the control source to reference microphone becomes larger. This implies that the separation of control input and measured output is improved so that the better performance is expected [11]. Although such remarkable change is not observed in $G_{zu}(s)$, the gain is slightly larger in the middle frequency range of Swinbanks' source, which is the nature of the source reported in [5].

In addition, in order to guarantee the closed-loop system stability against the modeling error of the nominal plant, additive uncertainty model is introduced for feedback-path transfer function. That is, for cases (a) and (b), $G_{yu}(s)$ is considered as

$$G_{yu}(s) = \overline{G}_{yu}(s) + W(s)\delta(s), \tag{4}$$

where $\overline{G}_{yu}(s)$ is the nominal plant for $G_{yu}(s)$, $\delta(s)$ is normalized modeling error whose $\mathcal{H}_\infty$ norm is less than or equal to 1, and $W(s)$ is a weighting function which is determined to cover the modeling error as shown in Figure 4. Similarly, for case (c) we define

$$\begin{bmatrix} G_{yu}(s) & G_{yv}(s) \end{bmatrix} = \begin{bmatrix} \overline{G}_{yu}(s) & \overline{G}_{yv}(s) \end{bmatrix} + W(s)\Delta(s), \tag{5}$$

where $\Delta(s)$ is 1×2 normalized modeling error. Note that the common weighting function is used for all cases as

$$W(s) = \frac{0.015\left(s^2 + 2\zeta_1\omega_1 s + \omega_1^2\right)\omega_2^2\omega_3^2}{\omega_1^2\left(s^2 + 2\zeta_2\omega_2 s + \omega_2^2\right)\left(s^2 + 2\zeta_3\omega_3 s + \omega_3^2\right)}, \tag{6}$$

where $\omega_1 = 200$, $\zeta_1 = 0.9$, $\omega_2 = 650$, $\zeta_2 = 0.7$, $\omega_3 = 2200$, $\zeta_3 = 0.6$.

3.2. Controller design

According to the preparation above, sampled-data $\mathcal{H}_\infty$ control synthesis [12] is applied to the following digital controller design problem: find a discrete-time controller $K_d(z)$ which maximizes positive scalar α so that the following conditions hold:

(i) the closed-loop system of Figure 5 is internally stable;
(ii) there exists positive scalar d such that $\mathcal{L}_2$ induced norm of the closed-loop system is less than 1,

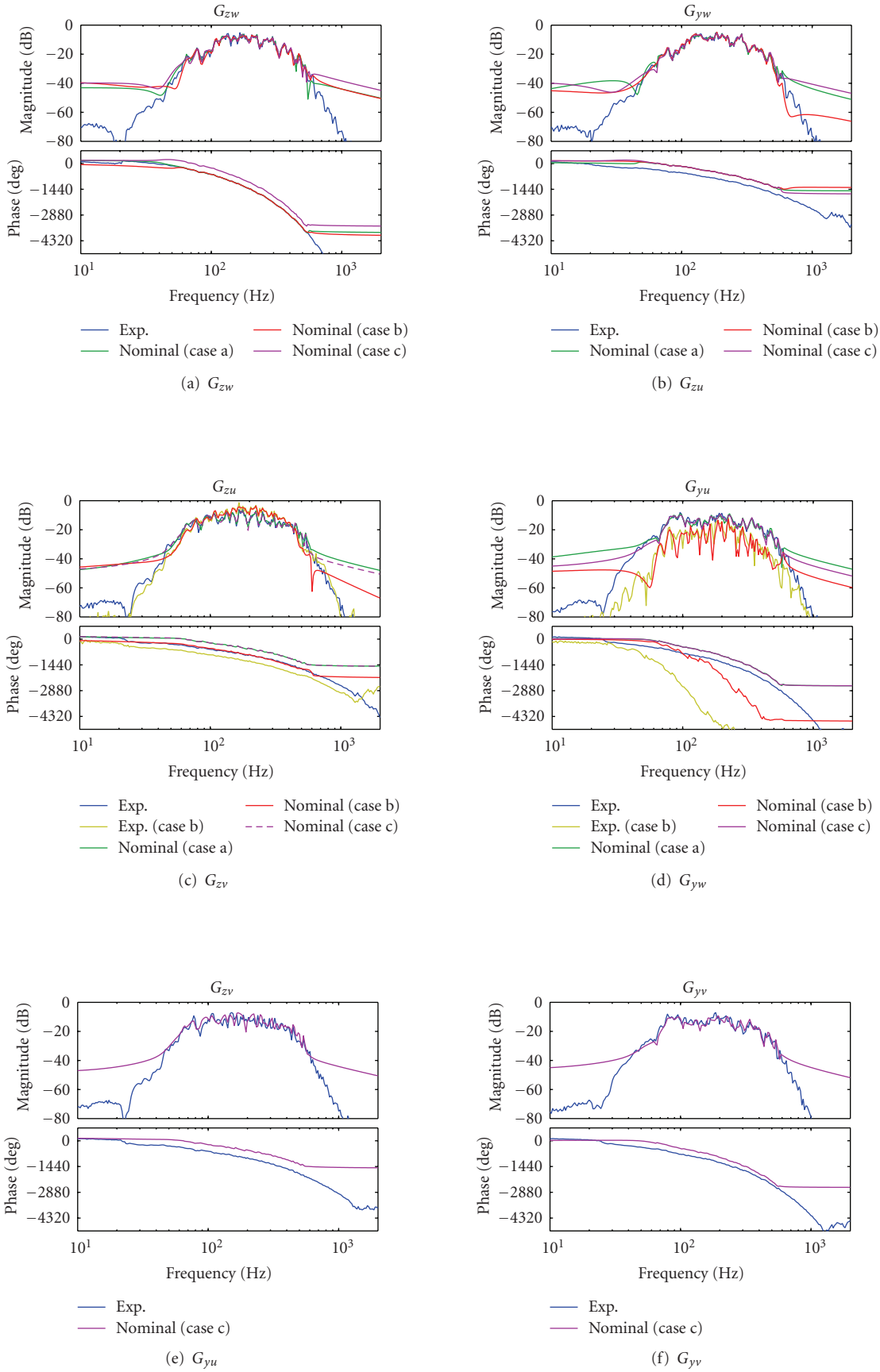

Figure 3: Frequency response of plant.

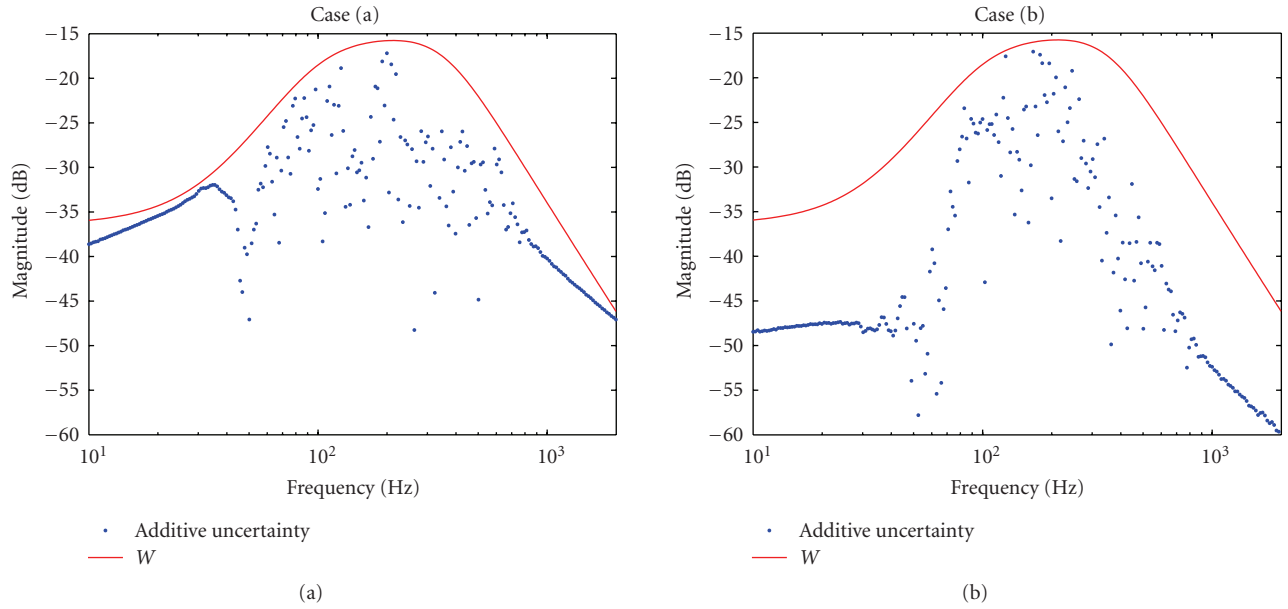

Figure 4: Additive uncertainty and weight.

Table 2: Sound pressure level at each grille.

Grille	Sound pressure level ($L_{Aeq,10\,s}$) [dB]			
	Without control	With control		
		Case (a)	Case (b)	Case (c)
No. 1	34.2	33.0 (−1.2)	32.5 (−1.7)	32.1 (−2.1)
No. 2	40.4	38.8 (−1.6)	37.4 (−3.0)	37.3 (−3.1)
No. 3	31.9	30.5 (−1.4)	28.9 (−3.0)	29.2 (−2.7)
No. 4	41.2	39.1 (−2.1)	37.1 (−4.1)	37.2 (−4.0)

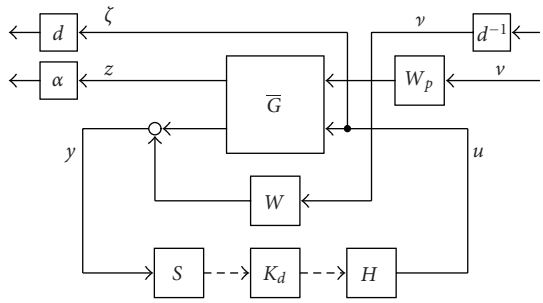

Figure 5: Robust performance problem with scalings.

where S is the sampler with sampling period $h = 1$ millisecond, H is the zeroth order hold, and $W_p(s)$ is a bandpass filter given by

$$W_p(s) = \left(\frac{s}{s+\omega_{p_1}}\right)^2 \left(\frac{\omega_{p_2}}{s+\omega_{p_2}}\right)^2, \quad \omega_{p_1} = 2\pi \times 80, \quad \omega_{p_2} = 2\pi \times 400. \tag{7}$$

Note that the closed-loop system gain is robustly minimized by maximizing α to improve control performance to attenuate fan noise.

The design results are as follows. The maximal $\alpha = 4.64$ was achieved for $d = 1.07$ for case (a), and the maximal $\alpha = 5.87$ was achieved for $d = 1.56$ for case (b), which implies that the closed-loop performance will be improved by Swinbanks' source. Furthermore, α was further improved by case (c) as $\alpha = 6.10$ for $d = 1.23$, because of the less conservative design. The order of $K_d(z)$ is 93.

4. COMPARISON OF CONTROLLERS

In this section, both adaptive and robust controllers are examined, where each adaptive controller for cases (a) and (b) is determined as a fixed 100th IIR filter by using the filtered-U RLMS method (see [2] for design process in detail), while the controller for case (c) is determined as a single-input-double-output fixed 100th IIR filter by using the multiple-channel filtered-U RLMS method [6].

Figure 6 shows adaptive and robust controllers for cases (a) and (b). It can be seen that for the adaptive controllers, the peak gains at about 60, 90, and 100 Hz become smaller when Swinbanks' source is used, while the similar phenomenon has been reported in [5]. The effect of Swinbanks' source is also observed for the robust controllers shown as the flat gain characteristic within the frequency range from

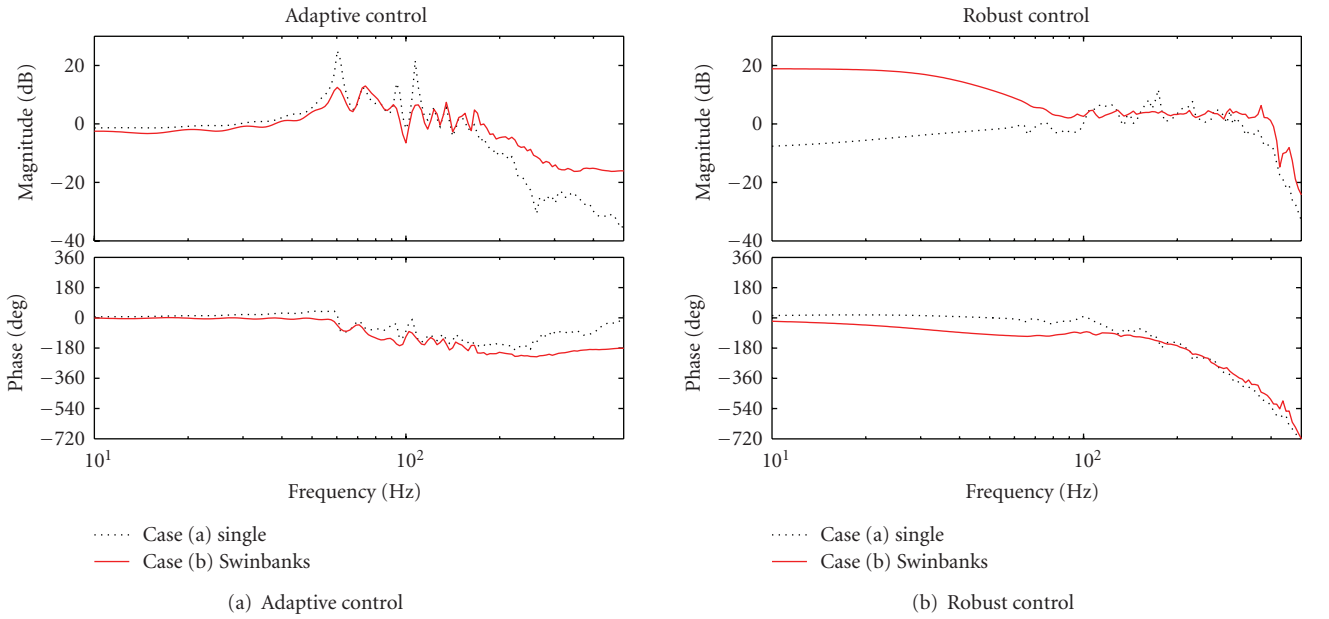

(a) Adaptive control (b) Robust control

Figure 6: Effect of Swinbanks' source.

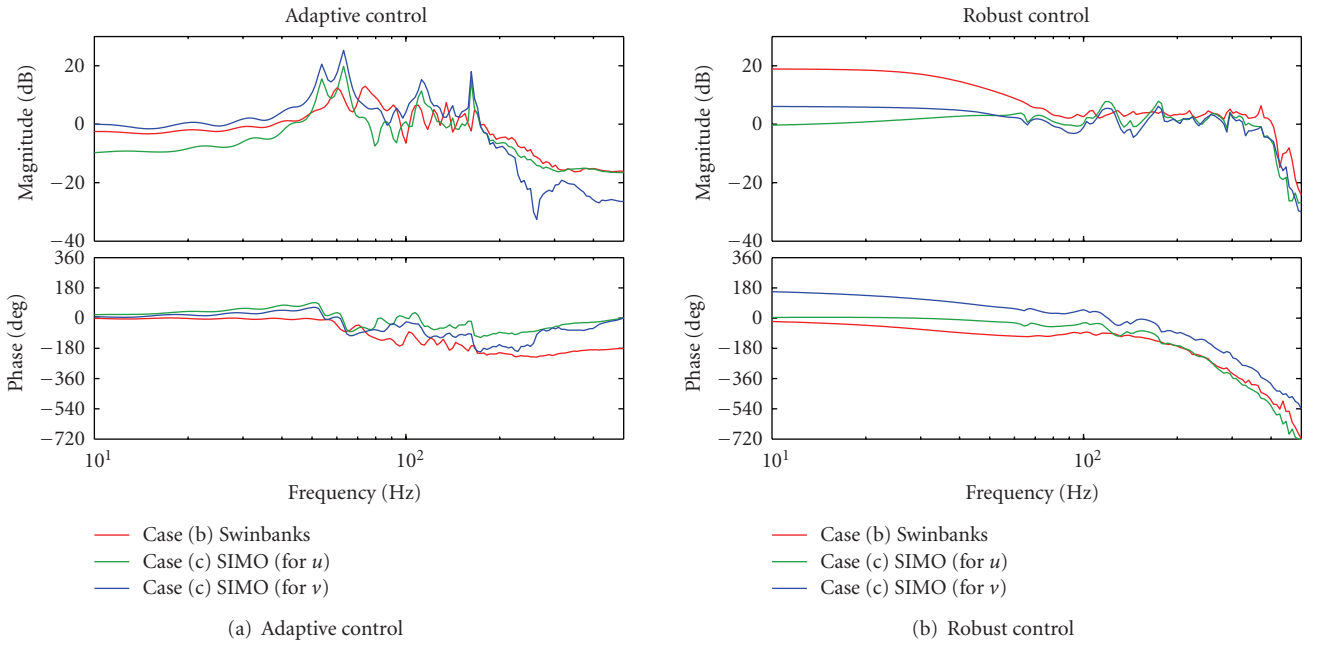

(a) Adaptive control (b) Robust control

Figure 7: Effect of SIMO design.

80 to 400 Hz, while for the case with a single loudspeaker, relatively large peak at about 180 Hz is appeared.

Figure 7 shows adaptive and robust controllers for cases (b) and (c). It can be seen for the robust controller of case (c) that Swinbanks' source characteristic is automatically obtained, since (i) the gain characteristics of both channels of the controller are similar and (ii) the phase difference is around 180 deg. Note that this fact is firstly reported in this paper. Furthermore, by examining the result in detail, advantages of robust control design with case (c) are observed. Firstly, from the gain characteristic, the controller for case (c) has relatively large peaks at about 120 and 170 Hz compared with case (b), which suggests that the flat gain characteristic of Swinbanks' source is not essential for performance improvement for actual ventilation system. Secondary, in the frequency range around 60 $\sim$ 400, the gain from y to v is slightly smaller than from y to u, which can be interpreted as the result of robust control design to compensate the attenuation of sound due to propagation. In contrast, it might be difficult to give such a reasonable interpretation for the adaptive controller of case (c).

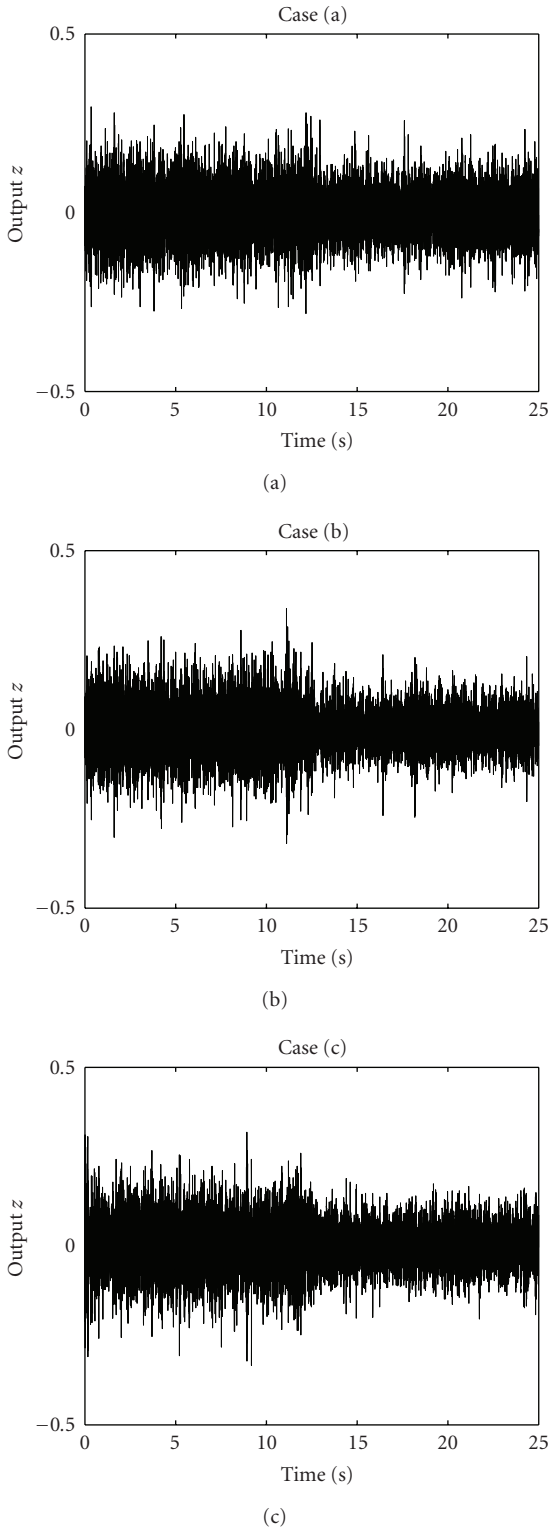

FIGURE 8: Time response of z.

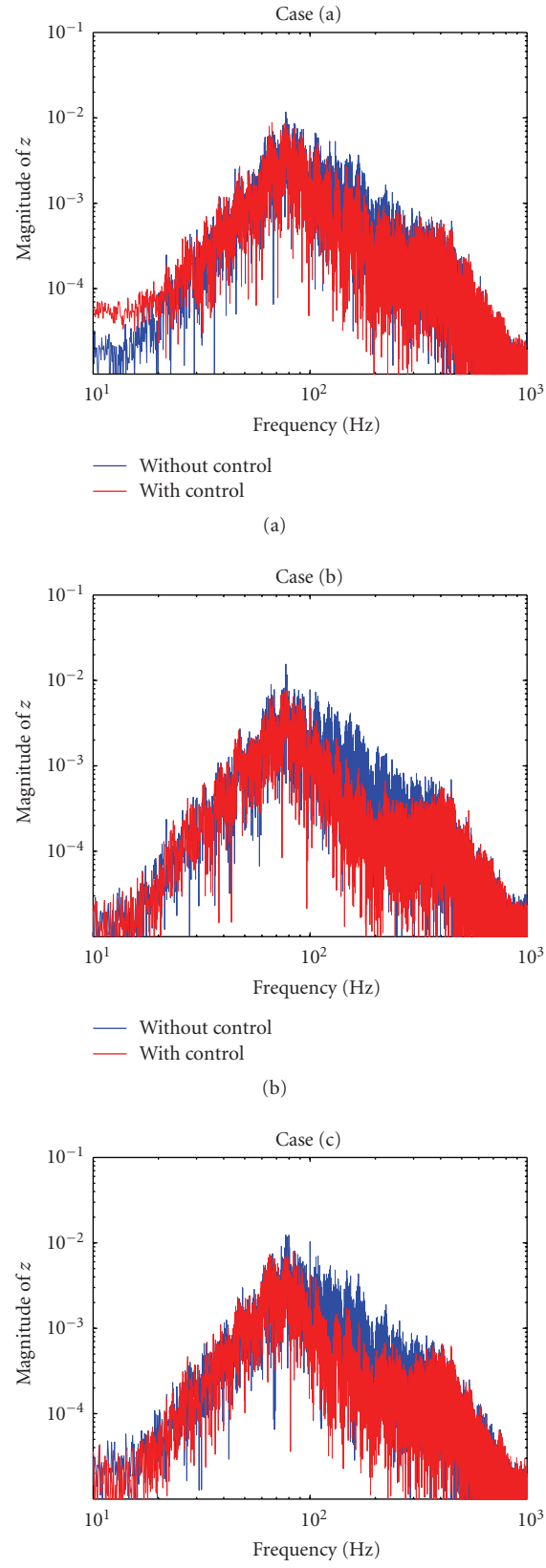

FIGURE 9: FFT analysis result of z.

5. CONTROL EXPERIMENTS

In this section, robust controllers designed so far are compared by control experiments.

Figure 8 shows time response of error microphone signal z, where the first 12.5 seconds are without control and the following 12.5 seconds are with control. The smaller sampling period (0.5 millisecond) is used for measurement to observe intersample behavior within the sampling period of the controller. It can be seen that cases (b) and (c) show better performance than case (a), while in [5] it has been reported by experimental result that the performances of cases (a) and (b) are similar. This might be caused since directional microphones are used in [5] but not used in this paper.

Figure 9 shows the FFT analysis result of Figure 8. It can be seen that the amplitude of z is reduced within 80 to 400 Hz.

It should be noted that the main frequency component of noise occurs around 100 Hz whose noise shape differs very much from the open-loop frequency response of G_{zw} shown in Figure 3. Therefore, it is expected that the system performance will be improved by setting the weight function $W_p(s)$ to consider the noise shape.

Table 2 shows sound pressure level measured below each grille. It can be seen that the attenuation level of case (b) is about twice the level of case (a), which shows the availability of robust control design for Swinbanks' source. On the other hand, the advantage of case (c) could not be shown (i.e., the attenuation level is similar to case (b)). It is not what we expect from the design results with larger α. The reason of this phenomenon is currently under study. One may pose a conjecture that it is from the modeling error. We have considered the modeling error from the control input to the measured output, however, other modeling errors are not reflected in the design. Especially the error of the transfer function from v to z could greatly affect the experimental result of case (c). Indeed, the gain characteristic in Figure 3 shows that there is a relatively large difference between the experimental result and the nominal plant compared with the other transfer functions. Hence we are working on the improvement of the modeling for utilizing the potential advantage of the design setup in case (c), by accounting the modeling error and/or by setting the nominal plant order higher in control design. We could report the results in the future.

6. CONCLUSIONS

In this paper, we have examined a robust control design of active noise control systems with a pair of loudspeakers, and the validity of the design method has been shown experimentally by using a ventilation system installed in a real house. The results are summarized as follows.

(i) Firstly, by using Swinbanks' source as a pair of loudspeakers, it has been confirmed that the controller designed by robust control method has flat gain characteristic which has been reported in adaptive control literature as an advantage of using Swinbanks' source.

(ii) Secondly, by considering the pair of loudspeakers as two independent actuators, it has been shown that the controller designed by robust control method is more acceptable than the one designed by adaptive control method, since the similar effect of Swinbanks' source was automatically obtained by the former design but not by the latter one.

(iii) Finally, by comparing the resultant noise attenuation levels of robust controllers with both a single loudspeaker and a pair of loudspeakers, the improvement has been shown by the latter case (i.e., the attenuation level was up to 4 dB while it was up to 2 dB for the former case).

Therefore, we conclude together with the result of [2] that the robust control design is useful to implement inexpensive active noise control systems with a pair of loudspeakers for ventilation ducts.

REFERENCES

[1] S. J. Elliott, *Signal Processing for Active Control*, Volume in the Signal Processing and Its Applications Series, Academic Press, New York, NY, USA, 2000.

[2] Y. Kobayashi and H. Fujioka, "Inexpensive implementation of active noise control systems for one-dimensional duct with application to a ventilating system," in *Proceedings of the 13th International Congress on Sound and Vibration (ICSV '06)*, Vienna, Austria, July 2006.

[3] M. A. Swinbanks, "The active control of sound propagating in long ducts," *Journal of Sound and Vibration*, vol. 27, pp. 411–436, 1973.

[4] S. Kijimoto, H. Tanaka, Y. Kanemitsu, and K. Matsuda, "Howling cancellation for active noise control with two sound sources," *Transactions of the Japan Society of Mechanical Engineers, Series C*, vol. 67, no. 656, pp. 52–57, 2001, (Japanese).

[5] J. Winkler and S. J. Elliott, "Adaptive control of broadband sound in ducts using a pair of loudspeakers," *Acustica*, vol. 81, no. 5, pp. 475–488, 1995.

[6] S. M. Kuo and D. R. Morgan, *Active Noise Control Systems: Algorithms and DSP Implementations*, John Wiley & Sons, New York, NY, USA, 1996.

[7] I. R. Petersen, H. R. Pota, and M. R. S. Jahromi, "System identification, uncertainty modelling and actuator placement in the robust control of an acoustic duct," in *Proceedings of International Conference on Information, Decision and Control*, pp. 41–46, Adelaide, Australia, February 2002.

[8] R. S. Erwin and D. S. Bernstein, "Discrete-time H_2/H_∞ control of an acoustic duct: δ-domain design and experimental results," in *Proceedings of the 36th IEEE Conference on Decision and Control (CDC '97)*, vol. 1, pp. 281–282, San Diego, Calif, USA, December 1997.

[9] Q.-F. Fan, K. Nonami, and M. Nakano, "Active noise control of one-dimensional exhaust duct using H^∞ control theory," *Transactions of the Japan Society of Mechanical Engineers, Series C*, vol. 62, no. 597, pp. 1805–1810, 1996.

[10] Y. Kobayashi and H. Fujioka, "Active noise control of one-dimensional duct via sampled-data $\mathcal{H}_\infty$ control," in *Proceedings of the 42nd IEEE Conference on Decision and Control (CDC '03)*, vol. 4, pp. 3900–3904, Maui, Hawaii, USA, December 2003.

[11] D. S. Bernstein, "What makes some control problems hard?" *IEEE Control Systems Magazine*, vol. 22, no. 4, pp. 8–19, 2002.

[12] T. Chen and B. Francis, *Optimal Sampled-Data Control Systems*, Springer, New York, NY, USA, 1996.

Hindawi Publishing Corporation
Advances in Acoustics and Vibration
Volume 2008, Article ID 791050, 12 pages
doi:10.1155/2008/791050

Research Article

Genetic Algorithm Applied to the Eigenvalue Equalization Filtered-x LMS Algorithm (EE-FXLMS)

Stephan P. Lovstedt,[1] Jared K. Thomas,[2] Scott D. Sommerfeldt,[1] and Jonathan D. Blotter[2]

[1] *Department of Physics and Astronomy, College of Physical and Mathematical Sciences, N283 ESC, Brigham Young University, Provo, UT 84602, USA*
[2] *Department of Mechanical Engineering, Ira A. Fulton College of Engineering and Technology, 435 CTB, Brigham Young University, Provo, UT 84602, USA*

Correspondence should be addressed to Scott D. Sommerfeldt, scott_sommerfeldt@byu.edu

Received 12 December 2007; Accepted 7 March 2008

Recommended by Marek Pawelczyk

The FXLMS algorithm, used extensively in active noise control (ANC), exhibits frequency-dependent convergence behavior. This leads to degraded performance for time-varying tonal noise and noise with multiple stationary tones. Previous work by the authors proposed the eigenvalue equalization filtered-x least mean squares (EE-FXLMS) algorithm. For that algorithm, magnitude coefficients of the secondary path transfer function are modified to decrease variation in the eigenvalues of the filtered-x autocorrelation matrix, while preserving the phase, giving faster convergence and increasing overall attenuation. This paper revisits the EE-FXLMS algorithm, using a genetic algorithm to find magnitude coefficients that give the least variation in eigenvalues. This method overcomes some of the problems with implementing the EE-FXLMS algorithm arising from finite resolution of sampled systems. Experimental control results using the original secondary path model, and a modified secondary path model for both the previous implementation of EE-FXLMS and the genetic algorithm implementation are compared.

1. INTRODUCTION

The most common control approach control (ANC) is the filtered-x least mean squares (FXLMS) algorithm [1, 2]. One of the limitations of the FXLMS algorithm is that it exhibits frequency-dependent convergence behavior that can lead to a significant degradation in the overall performance of the control system. Two types of noise will be discussed as they relate to this limitation.

(1) A single tone with time-varying frequency, such as engine noise, where the engine firing frequency changes along with the speed of the engine in revolutions per minute (rpm) during operation. It is assumed that the signal power of the tone in the reference remains the same, independent of frequency. This type of noise will be referred to as "swept tone noise."

(2) Noise containing multiple quasistationary tones, such as helicopter cabin noise, where multiple rotating parts contribute strong tones that do not vary significantly in frequency during normal operation. This type of noise will be referred to as "multiple tone noise."

Various adaptations to the FXLMS algorithm have been developed in an effort to overcome the performance loss due to its frequency-dependent convergence behavior. The normalized FXLMS algorithm [3] has a variable convergence parameter that changes with the power of the input for noise containing a single tone. Clark and Gibbs and Lee et al. [4, 5] developed a method to process tonal components of a multiple tone noise problem separately allowing for a different convergence parameter for each tone. More uniform convergence and increased overall attenuation of all tones are achieved at the expense of more computational complexity. Kuo et al. improved convergence for multiple tone noise by optimizing the magnitude of internally generated reference signals as the inverse of the secondary path magnitude [6]. This approach requires that the user have control over the reference tone amplitudes. The drawback of most of these approaches is that they increase the computational burden of the algorithm, increase the algorithm's complexity, or are not applicable to one of the two types of noise considered here.

Elliot and Cook preconditioned the input to the LMS update by using a second filter that was the inverse of the minimum phase part of the secondary path estimate, thus "whitening" the input and making convergence independent of resonances in the secondary path [7].

Prior research by the authors proposed the eigenvalue equalization filtered-x least mean squares (EE-FXLMS) algorithm [8]. This algorithm improves performance without increasing the computational burden or complexity of the algorithm. The development of the algorithm came from focusing on the eigenvalues of the autocorrelation matrix of the filtered-x signal, which relate to the dynamics or time constants of the modes of the system. Typically, there is a large spread in the eigenvalues of this matrix, corresponding to fast and slow modes of convergence. If the variance in the eigenvalues of the autocorrelation matrix is minimized, convergence properties will be more uniform and controller parameters could be optimized for all frequencies leading to increased performance (faster convergence speed and additional noise attenuation) of the controller.

For the EE-FXLMS algorithm, adjustments to the secondary path estimate are made in the frequency domain. The phase of the original secondary path transfer function estimate is preserved while the magnitude coefficients are adjusted to have the inverse trend of tones in the reference signal. The new magnitude coefficients are combined with the original phase response and transformed back into the time domain, giving a new FIR estimate of the secondary path to filter the reference signal. This is intended to equalize the power of tonal components in the filtered-x signal, which in turn would equalize the eigenvalues of the filtered-x autocorrelation matrix.

Previously, the EE-FXLMS was implemented for swept tone noise by making each secondary path transfer function coefficient flat (equal amplitude) over frequency because, as noted, the power of the reference signal was independent of frequency. For multiple tones, the trend of the magnitude coefficients was made to be the inverse trend of the amplitudes of the tones in the reference signal. For both cases, this led to more uniform eigenvalues (of the filtered-x autocorrelation matrix), faster convergence times, and additional attenuation at the error sensor [8].

This paper revisits the EE-FXLMS implementation to modify the magnitude coefficients as motivation for investigating improved methods of adjusting the magnitude coefficients. In this work, a genetic algorithm is used to find the optimal magnitude coefficients for a limited frequency range, swept tone noise, and for a specific set of reference tones for multiple tone noise. Experimental results for ANC in a mock cabin enclosure for these control implementations are presented and compared.

2. BACKGROUND

The FXLMS algorithm involves adaptively filtering a reference signal taken from the noise source to create a control signal that attenuates the unwanted noise. The LMS update is used to change the control filter coefficients such that the measured residual noise is minimized. The measured residual is called the error signal and for this research, it will be utilized to minimize a squared pressure (SP) quantity. The mean squared error is a quadratic function of the filter coefficients with a unique global optimum. The LMS update is a gradient descent search method. It follows the path of steepest descent on the error surface toward the optimum filter weights. A block diagram for a single-channel implementation of the FXLMS algorithm is shown in Figure 1. In Figure 1, and in all equations presented, the variable t is a discrete time index and the variable z a discrete frequency domain index.

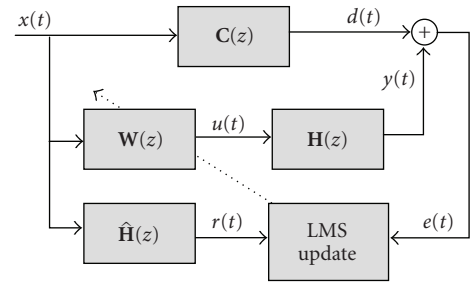

$d(t)$: Desired signal
$u(t)$: Control signal
$y(t)$: Output signal
$x(t)$: Reference signal
$e(t)$: Error signal
$r(t)$: Filtered-x signal
$\mathbf{C}(z)$: Plant
$\mathbf{W}(z)$: Adaptive filter
$\mathbf{H}(z)$: Actual secondary path
$\hat{\mathbf{H}}(z)$: Secondary path estimate

Figure 1: Block diagram of the FXLMS algorithm.

2.1. Secondary path transfer function

The FXLMS algorithm derives its name from the filtered-x signal, $r(t)$, which is the convolution of the reference signal $x(t)$, with $\hat{\mathbf{h}}(t)$, a finite impulse response (FIR) estimate of the secondary path transfer function. The secondary path transfer function (shown in Figure 1 as $\mathbf{H}(z)$) includes the effects of digital-to-analog and analog-to-digital converters, filters, audiopower amplifiers, loudspeakers, the acoustical transmission path, error sensors, and other signal conditioning.

The secondary path model, $\hat{\mathbf{H}}(z)$, is estimated through a process called system identification (SysID). The SysID process is performed offline (before ANC is started) for the fastest convergence of the algorithm where the secondary path does not change significantly during operation of the system. Band-limited white noise is played through the control speaker(s) and the output is measured at the error sensor(s). The measured impulse response is obtained as an FIR filter, $\hat{\mathbf{h}}(t)$, that represents $\hat{\mathbf{H}}(z)$. The coefficients of $\hat{\mathbf{h}}(t)$ are stored and used to prefilter the input signal to the LMS update to run control. While inclusion of $\hat{\mathbf{H}}(z)$ is necessary for stability, the FXLMS algorithm is robust to errors in its estimation. The algorithm will converge (slowly) as long as phase errors are less than 90° [1] and phase errors less

than 40° do not significantly affect convergence [9]. The gain applied to the reference signal by filtering it with $\hat{\mathbf{h}}(t)$ does not affect the stability of the algorithm and is usually compensated for by modifying the convergence parameter μ.

2.2. FXLMS convergence and eigenvalues of filtered-x autocorrelation matrix

The time constants for the modes of convergence of the ANC system are determined by the eigenvalues of the autocorrelation matrix of the filtered-x signal [10]. While the convergence parameter, μ, can be optimized to give fast convergence for one mode, others will converge more slowly. For swept tone noise, μ can be optimized for a given frequency in the range of the sweep, but not for all frequencies in the range. When the algorithm is controlling a tone at a frequency other than that for which it was optimized, convergence will be slower and attenuation less. For multiple tone noise, the algorithm will be able to attenuate portions of the total noise quickly while other tones in the noise will linger and take longer to converge.

The properties of the filtered-x signal, and hence the autocorrelation matrix, are a function of the magnitude response of $\hat{\mathbf{H}}(z)$ and the spectrum of the reference signal. The autocorrelation matrix of the filtered-x signal is defined as

$$\mathbf{R} = E[\mathbf{r}(t)\mathbf{r}^T(t)], \tag{1}$$

where $E[\cdot]$ denotes the expected value of the operand which is the filtered-x signal vector, $\mathbf{r}(t)$, multiplied by the filtered-x signal vector transposed $\mathbf{r}^T(t)$. In general, it has been shown that the FXLMS algorithm (or any of its variations) will converge (in the mean) and remain stable as long as the chosen μ satisfies the following equation [9]:

$$0 < \mu < \frac{2}{\lambda_{\max}}, \tag{2}$$

where $\lambda_{\max}$ is the maximum eigenvalue of the autocorrelation matrix.

In practice, it is computationally demanding to obtain a real-time estimate of the autocorrelation matrix, so the optimal μ is often selected through experimentation. In this work, the structure of the eigenvalues of a given ANC problem is explored using an offline estimate of the autocorrelation matrix. This is done in a numerical analysis program by taking an actual $\hat{\mathbf{h}}(t)$ model from a mock cabin enclosure, convolving this with a reference signal for the given noise application, computing the autocorrelation matrix, and getting the eigenvalues. If a single frequency reference signal is used, $\lambda_{\max}$ can be computed for that frequency. If the simulation is repeated over a range of frequencies, $\lambda_{\max}$ for a single tone at each frequency in that range can be found. For control of a single tone, $\lambda_{\max}$ is the only eigenvalue of interest since it will determine the convergence of the algorithm for that frequency. Figure 2 (solid line) shows an offline simulation using an actual $\hat{\mathbf{h}}(t)$ from the mock cabin enclosure, and equal amplitude tonal inputs from 0–300 Hz. The disparity in $\lambda_{\max}$ over frequency shows how the convergence of the algorithm will change as it controls a single tone swept through this range. The range of interest from 0–300 Hz was selected because the experimental hardware was set with a cutoff frequency at 400 Hz. The eigenvalues in the figure have been normalized to the largest eigenvalue in the range.

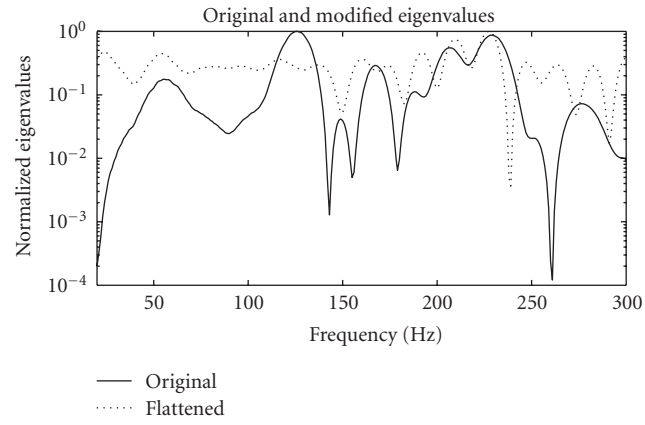

Figure 2: Plot of normalized maximum eigenvalues over frequency for original and modified (flat magnitude) eigenvalues.

The largest eigenvalue for a single tone occurs at about 125 Hz. This location corresponds to the largest μ that is stable for the entire frequency range from 0–400 Hz as given by (2). All other frequencies have a smaller eigenvalue and could use a larger μ, and still be stable, if just that particular frequency was targeted for control. Frequencies at the valleys of the solid line in Figure 2 have the smallest eigenvalues and could use the largest μ's and still be stable, again if they were the only frequencies targeted for control. The larger μ's are especially desirable for nonstationary noise as they lead to faster convergence and increased attenuation.

For multiple tone noise that is stationary, the eigenvalues are not computed for individual tones as before, but for the composite reference signal containing all tones to be controlled. In this case, the disparity among all of the nonzero eigenvalues, not just $\lambda_{\max}$, gives information about how different spectral components of multiple tone noise will converge.

3. EIGENVALUE EQUALIZATION—PRIOR METHODS

If the variance in the eigenvalues of the autocorrelation matrix was minimized, a single-convergence parameter could then be chosen that would be nearly optimal for all frequencies targeted for control and the algorithm would converge at nearly the same rate at all frequencies or for all modes of convergence. Additionally, "misadjustment" errors that prevent the algorithm from converging to the true optimal solution depend on the eigenvalues of the autocorrelation matrix. Misadjustment error is larger when there is large disparity in the eigenvalues [11]. Misadjustment (and hence attenuation) can be improved by making these eigenvalues equal.

As previously stated, the autocorrelation matrix is directly dependent on the filtered-x signal, which is computed by filtering the input reference signal, $x(t)$, with $\hat{\mathbf{H}}(z)$. Any attempt at equalizing the eigenvalues must be done by altering either the reference signal or the secondary path model. Adjusting the power of the reference signal has been shown to be an effective way of doing this [6]; however, in many applications this amount of control over the reference signal is not feasible. We focus on making changes to $\hat{\mathbf{H}}(z)$ only. The span, defined as $\lambda_{\max}$ divided by $\lambda_{\min}$, is used as a metric to quantify any improvement in the eigenvalue disparity. This ratio is the most important property, as any change in the actual magnitude of the eigenvalues is compensated for by making a complementary adjustment to the magnitude of the convergence parameter μ.

3.1. Eigenvalue equalization applied to swept tone noise

For swept tone noise, it has been shown that flattening the magnitude coefficients of $\hat{\mathbf{H}}(z)$, while preserving the phase reduces the variance in the eigenvalues [8]. Figure 2 shows both the original eigenvalues (solid line) and the modified eigenvalues (dotted line) when the magnitude coefficients of $\hat{\mathbf{H}}(z)$ are flattened. In the figure, the eigenvalues for both the original and modified cases have been normalized by the largest of the original eigenvalues. The span for the original eigenvalues in this range (0–400 Hz on the plot) is 1.385×10^5 and the span for the flattened magnitude $\hat{\mathbf{H}}(z)$ is 162.3. These modifications to $\hat{\mathbf{H}}(z)$ make a noticeable improvement in the performance of the algorithm [8]. The more uniform rate of convergence of all modes of the system is beneficial as it speeds up the overall convergence of the error signal. For dynamic signals, this increased rate of convergence equates to greater attenuation, as it also results in more rapid tracking.

The eigenvalues are much more uniform, but still not perfectly uniform. This is due to the finite resolution of the digital system and of the sampled secondary path estimate. The shape of the magnitude response, $\hat{\mathbf{H}}(z)$, can only be constrained to some value at its respective frequency bins; there is no guarantee that the response of $\hat{\mathbf{H}}(z)$ is also flat between frequency bins. As an example, a 128 coefficient $\hat{\mathbf{H}}(z)$ model sampled at 2000 Hz will have a frequency resolution of 15.625 Hz. For swept tone noise, the system may be excited at any frequency in the range of the application. An estimate of the "analog" or continuous response of $\hat{\mathbf{H}}(z)$ between frequency bins can be made by zero padding the 128-coefficient model before computing the fast Fourier transform (FFT). The original, flattened, and zero-padded flattened magnitude coefficients of $\hat{\mathbf{H}}(z)$ from a mock cabin are shown in Figure 3. The discrete magnitude response is indeed flat at the frequency bin values, but the zero-padded model shows that the true response deviates from flat in between bins. This magnitude variation between frequency bins in $\hat{\mathbf{H}}(z)$ contributes to the residual variation seen in the modified eigenvalues for the range.

Another source of variation may come from frequency leakage when the reference signal gets downsampled before being convolved with $\hat{\mathbf{h}}(t)$. Before being convolved with $\hat{\mathbf{h}}(t)$, the reference signal is downsampled with the same sampling frequency as was used to find $\hat{\mathbf{h}}(t)$; for this example, 2000 Hz was used. In addition, only n number of samples are kept of the reference signal at a given time, where n is the number of coefficients in $\hat{\mathbf{h}}(t)$; for this example, 128 was used. This downsampling process causes amplitude estimation error in the frequency domain due to leakage. Thus if the original reference signal is assumed to be equally weighted at each frequency, as was done to create the eigenvalue simulations shown in Figure 2, the actual reference signal used in those simulations is no longer equally weighted over frequency. This also contributes to residual variation in the eigenvalues.

3.2. Eigenvalue equalization applied to multiple tone noise

When multiple noise sources are present, a reference signal may be obtained from each and combined into a single-reference signal. In some cases, the reference signal will contain a fundamental frequency and harmonics from a single-noise source. In either case, the combined tones in the reference signal will in general have different amplitudes. This weighting of the reference tones will be specific to each application and depends on how the reference signals are conditioned and combined. This frequency-dependent weighting of the reference tones as well as the gain applied by the secondary path estimate contributes to the eigenvalue disparity for multiple tone noise. For multiple tone noise in this research, an arbitrary (but specific, for consistency) weighting was applied to the reference tones. The amplitude of the reference signal tones was defined by

$$\text{Tonal Amplitude} = -0.0036^{*}(\text{Tonal Frequency}) + 1.18. \tag{3}$$

This gave a decreasing trend in amplitude for increasing frequency that ranged from 1.0 at 50 Hz to 0.1 at 300 Hz. All tones used for the multiple tone noise were in this range.

To equalize the eigenvalues for this case, a trend line connecting the peaks of the tones (on a power spectrum plot) in the reference is drawn. The inverse of this line gives the desired trend for the magnitude coefficients in $\hat{\mathbf{H}}(z)$, which here corresponds to the inverse of (3). Since the tonal amplitudes for the test case were specified, obtaining the inverse trend line was straightforward. In actual implementation, an offline "Ref ID" process would also be required. This would entail recording the reference signal under normal operating conditions for the system at the sampling frequency used by the controller. The desired magnitude trend for the modified Sys ID filter could be obtained from the fast Fourier transform (FFT) or power spectrum plot of the reference.

This type of modified $\hat{\mathbf{H}}(z)$ is designated as an "X-inverse" model. Figure 4 shows the trend line for the amplitude of tones in the reference as given by (3), the desired magnitude response for $\hat{\mathbf{H}}(z)$, and the zero-padded response of the 256 coefficients X-inverse model. All curves have been normalized in the figure. As before, the response of the filter between bins deviates from the trend assigned

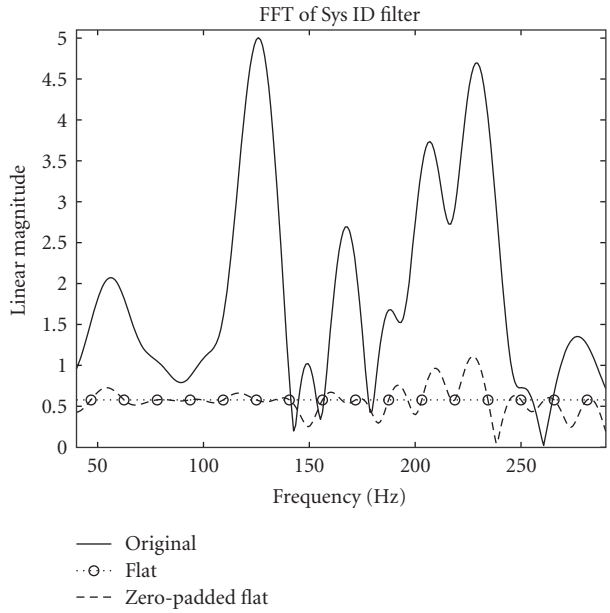

Figure 3: Plot of original-, flattened-, and zero-padded flattened magnitude coefficients of $\hat{\mathbf{H}}(z)$.

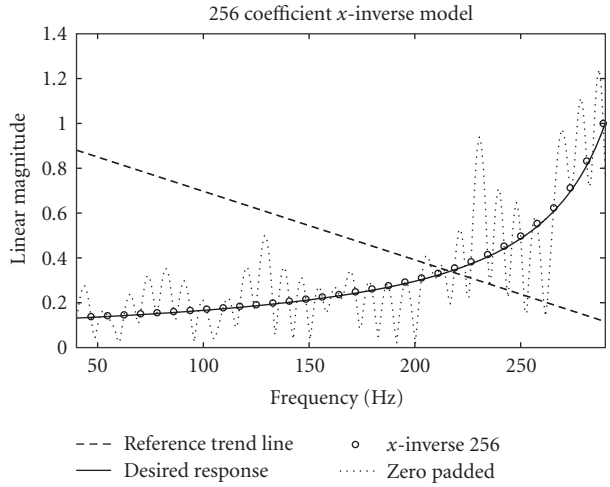

Figure 4: Reference tone amplitude trend line for multiple tone noise signals with desired trend and zero-padded X-inverse model magnitude responses.

the coefficients. Increasing the coefficients from 128 to 256 makes the magnitude response match the desired curve at more points, but does not improve the variation between bins. The same is true for the phase response.

This method will reduce the eigenvalue variation only for some cases. If the tones in the reference are chosen to correspond exactly to frequency bin values, the eigenvalues are much more uniform using the X-inverse model than using the original model. However, if the tones lie off these frequency bin values, the eigenvalue span can be worse than for the unmodified $\hat{\mathbf{H}}(z)$.

Table 1: Comparison of eigenvalue span for original and X-inverse models for multiple tones with frequencies on and off frequency bin values.

	Sys ID length	Original	X-inverse
Tones on bin values	128	4350	2.0
	256	2162	2.0
Tones off bin values	128	217	16
	256	239	991

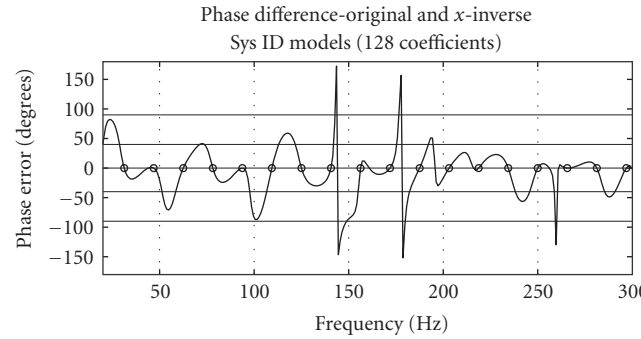

Figure 5: Phase difference between 128-coefficient original and X-inverse models with reference tones off frequency bin values. Dashed lines indicate tonal frequencies.

Two reference signals containing six tones were made for comparison; one with all six tones on frequency bins (62.5, 93.75, 125, 171.875, 203.125, and 296.875 Hz) and the other with these tones shifted slightly to lie between bin values (50, 100, 130, 180, 200, and 280 Hz). The length of the FIR filter model of $\hat{\mathbf{H}}(z)$ was increased from 128 to 256 to double the resolution in an attempt to constrain the magnitude response between bins to follow more closely the desired trend. The eigenvalue span for these reference signals with the original and X-inverse $\hat{\mathbf{H}}(z)$ models of different lengths were calculated. The results of these comparisons are shown in Table 1. When the tones lie on the frequency bins, the X-inverse model gives a significant improvement in the eigenvalue span. For offbin frequencies the X-inverse model is better than the original for the 128-coefficient filter, but not as good as when the tones are on bins. When the filter length is increased to 256, the span for the X-inverse model was worse than the original model for offbin tones. The span for the X-inverse model with 256 coefficients went from 239 to 991 likely because the magnitude response of the X-inverse model goes almost to zero at 200 Hz (see Figure 4). Increasing the resolution by using a longer filter does not (at least in some cases) improve the eigenvalue span. This gives the desired magnitude response at a larger number of points, but the deviation from the desired trend in between these points is not necessarily improved.

The eigenvalue span for the 128-coeffficient X-inverse model and tones at offbin frequency values was reduced significantly over the original model from 217 to 16. However, Figure 5 shows that the phase errors introduced exceed stability limits near several tones in the reference.

Horizontal lines mark 40° and 90° of phase error between the original and modified phase response and vertical dashed lines show the positions of offbin reference tones. Phase errors introduced into regions where no tonal components of the noise are being controlled will not affect the stability or performance of the system. For helicopters, the tones in the noise are very stable and do not shift in frequency significantly, however, phase errors very near those tonal frequencies are potentially problematic for both stability and overall performance of the ANC system.

In this case, even though the eigenvalue span was improved, the X-inverse model would not work well if used in ANC since instability and poor performance would result from the phase issues. This is another reason the X-inverse method is inadequate.

The inability to control the magnitude and phase response of the secondary path estimate in between frequency bin values and the unpredictable changes that occur in each when the magnitude coefficients of the original model are modified make the X-inverse method of eigenvalue equalization inadequate. A genetic algorithm approach was developed to optimize the magnitude coefficients, and which can overcome these difficulties for multiple tone noise.

4. EIGENVALUE EQUALIZATION—GENETIC ALGORITHM

A genetic algorithm was used to investigate the possibility of getting more uniform eigenvalues over narrow bands of frequencies for swept tone noise and for specific multiple tone noise cases. Optimizing the magnitude coefficients of $\hat{\mathbf{H}}(z)$ in ways other than those described previously may lead to improved eigenvalue span, but are not intuitive. Genetic algorithms (GAs) [12, 13] have gained considerable popularity in recent years for their ability to solve problems with a large number of design variables, multiple local minima and maxima, nondifferentiable functions, or some combinations of these. They can work well for both discrete- and real-valued problems. GA's mimic the natural selection process found in nature that allows individuals with the best "fitness" to survive. Parents are chosen from the most fit individuals of a population of randomly generated designs. These parents are then sent through a reproduction process to exchange and pass on genetic information to new designs (children). As in nature, mutations are introduced occasionally to provide for random variation. Parents and children compete to be included in the next generation. As the generations progress, the random designs converge to a design that has the best fitness.

4.1. Genetic algorithm cycle

The genetic algorithm cycle used to optimize the magnitude coefficients of $\hat{\mathbf{H}}(z)$ can be broken down into nine steps. A brief description of each step is now given. It should be noted that other GA's with different cost functions could be investigated. The purpose of this work is to present one such GA and compare the results to other easily implemented techniques.

(1) Determine a coding for the design

Each design in a GA consists of a number of independent variables chosen by the designer. Each independent variable is called a "gene," a set of genes giving one design, or "chromosome." As the desired result of the algorithm was to obtain an optimized impulse response model, $\hat{h}(t)$, that could be used in physical experimentation, a 128 or 256 coefficient $\hat{h}(t)$ for the mock cabin described in Section 6 was obtained by the SysID process described in Section 2.1. The FFT of $\hat{h}(t)$ was then taken, and the phase information of $\hat{H}(z)$ was preserved in a vector. The magnitude information of $\hat{H}(z)$ was discarded, as the GA was implemented to find the optimal magnitude coefficients by making each unknown magnitude coefficient a gene. Each design then contained 64 or 128 genes, which were the unknown 128 or 256 magnitude coefficients of $\hat{H}(z)$ (since they are mirrored about the Nyquist frequency).

(2) Generate an initial population

Once the coding scheme for a single design was established, a population of N designs was randomly generated. This was done by randomly assigning a value between a minimum value of 0.01 and a maximum of 10 for each gene (magnitude coefficient) in the design. This range was chosen based on some trial and error. If the minimum was set to zero, the GA would make all the magnitude coefficients zero giving a trivial solution of all zero eigenvalues. The maximum value was set to 10 so that the generated designs were close to the overall magnitude values for the original model. The process was repeated N times to generate the entire population. In general, designs with many genes require large population sizes to maintain adequate diversity. The population size was 500.

(3) Calculate fitness for each design

After the initial population was randomly generated, each design was evaluated and assigned a fitness value. Each randomly generated set of magnitude coefficients was recombined with the stored phase information, and the inverse FFT was taken to get a new unique model for the impulse response, $\hat{\mathbf{h}}(t)$. This new model was used to compute the eigenvalues of the filtered-x autocorrelation matrix in the same manner as explained in Section 4. For swept tone noise, the eigenvalues were computed over a specified frequency range and then normalized by the largest of the eigenvalues. As the ideal normalized eigenvalue at each frequency would be one, the fitness value was chosen as a sum of the squared errors between the actual value of each eigenvalue in the frequency range and one, as shown in (4):

$$\text{fitness} = \sum_{f_{\text{start}}}^{f_{\text{end}}} (1 - \lambda_k)^2. \tag{4}$$

The fitness value for multiple tone noise was simply the span ($\lambda_{\max}$ divided by $\lambda_{\min}$) of all nonzero eigenvalues.

In addition, a penalty was applied to any design whose phase response was in error by more than 40° in a range of +/− 5 Hz around each of the tonal frequencies in the multiple tone noise. This was done to decrease the design's sensitivity to tonal frequencies shifting. Constraining the phase in this way ensures that the algorithm will remain stable for small changes in the tonal frequencies. Designs whose performance would be hindered by the phase error introduced by altering the magnitude response were assigned a poor fitness value.

(4) Selection of parents

A tournament selection process was used to choose parent designs from the population. A specified number of designs were randomly selected to compete in the tournament. The design with the best fitness wins the tournament and was made a parent design. This process was repeated until enough parents had been selected to make N children; a set of two parent designs producing a single-child design.

(5) Perform crossover

A process called crossover exchanged traits from each parent design and created children designs. In this way, new designs were made that had traits from each parent. For this work, blend crossover was used. In blend crossover, genes from both parents are blended to make two new children genes. This occurs gene by gene. First, a random number between zero and one is chosen for each gene to determine whether crossover will occur. If the random number is larger than the user defined crossover probability, no crossover occurs. The genes for the children, c_1 and c_2, are equal to the parent genes, p_1 and p_2, respectively, so that if no crossover occurs for any genes in the design, the children will be identical to the parents. If the random number is less than the user specified crossover probability, another random number is chosen. If it is <0.5, the blend parameter, a, is calculated by

$$a = \frac{(2r)^{1/\eta}}{2}, \tag{5}$$

and if the random number is ≥0.5, the blend parameter is

$$a = 1 - \frac{(2 - 2r)^{1/\eta}}{2}. \tag{6}$$

The children genes c_1 and c_2 are created from the parent genes p_1 and p_2 by

$$\begin{aligned} c_1 &= (a)p_1 + (1 - a)p_2, \\ c_2 &= (1 - a)p_1 + (a)p_2. \end{aligned} \tag{7}$$

The value of η is chosen by the user. As $\eta \to 0$, the crossover becomes uniform, meaning that $c_1 = p_2$ and $c_2 = p_1$. As $\eta \to \infty$, $a \to 1/2$ and the children's genes are the average of the parent's gene values.

The crossover probability was chosen to be 50% and η was 0.5.

(6) Perform mutation

After crossover, some of the genes in the children designs are mutated. Mutation provides for diversity and occasionally introduces new beneficial information into a design. Higher mutation probability maintains more diversity in the designs as the generations progress and can help the algorithm avoid converging on a local optimum in the design space. Mutation can be made dynamic allowing for high diversity initially, keeping the algorithm from settling prematurely in a local optimum. In later generations, mutation is constrained allowing the algorithm to randomly make fine adjustments to the design once it is near what is hoped to be the global optimum. Initially, mutation can cause the gene to become any value in the allowable range for that gene. By the last generation, when mutation occurs the new value for the gene is only allowed to have a new value that is very close to the original. The probability of mutation occurring does not change, only how different the mutated gene is allowed to be from its premutation value. This is done by introducing a dynamic mutation parameter α:

$$\alpha = \left(1 - \frac{n - 1}{N}\right)^{\beta}, \tag{8}$$

where n is the current generation number and N is the total number of generations. The exponent, β, is a user defined parameter that weights the dynamic function of α. If $\beta = 0$, α will always be one and the amount of mutation allowed will be uniform for all generations. If β is greater than zero, the amount of mutation allowed decreases as the generation number increases.

A random number is chosen to determine whether mutation will occur for each child gene. If the random number is less than the user-specified mutation probability, another random number, c_{mut}, is chosen within the allowable range for that gene. If c_{mut} is less than the current value for the gene, the new gene value is

$$c_{\text{new}} = c_{\min} + \left(c_{\text{mut}} - c_{\min}\right)^{\alpha}\left(c - c_{\min}\right)^{(1-\alpha)}, \tag{9}$$

and if c_{mut} is greater than the current value for the gene, the new gene value is

$$c_{\text{new}} = c_{\max} - \left(c_{\max} - c_{\text{mut}}\right)^{\alpha}\left(c_{\max} - c\right)^{(1-\alpha)}. \tag{10}$$

The mutation probability was chosen to be 50% and β was set to 0.5.

(7) Measure fitness of children

Once all of the children were created through crossover and mutation, the fitness value of each child was computed in the same way as described in Step 3.

(8) Perform elitism

Once each child design has a fitness value, parents are made to compete with children in a process called elitism. All of the parents and children are sorted by their fitness value, and the N number of designs with the best fitness value becomes the starting generation for the next iteration of the algorithm.

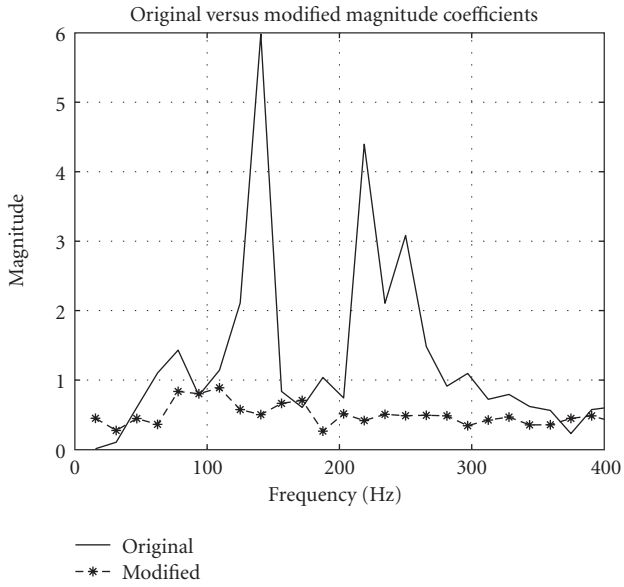

Figure 6: Original and modified magnitude coefficients of $\hat{H}(z)$ for genetic algorithm run from 60–90 Hz.

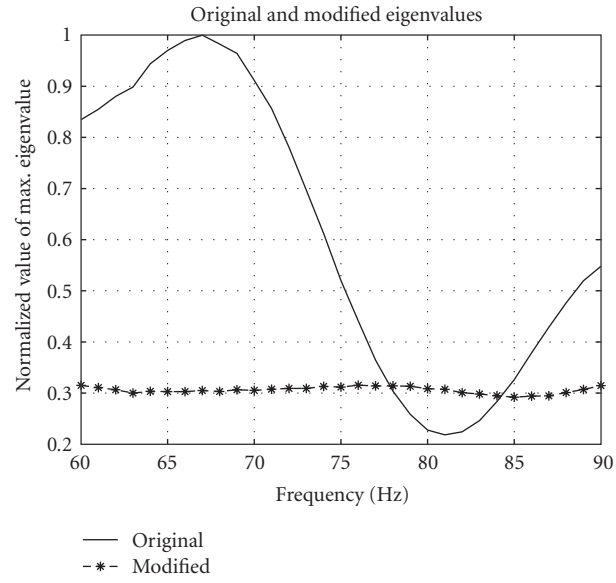

Figure 7: Normalized original and modified eigenvalues for genetic algorithm run from 60–90 Hz.

(9) Repeat Steps 4–8 for M number of generations

Steps 4–8 were repeated for M number of generations. The number of generations needed to be large enough to allow the algorithm to converge on an optimum design. For the work reported here, M was chosen to be in the range of 50–200.

The optimization performed by the genetic algorithm is all done offline as part of the setup of the ANC system after the offline system identification routine. It is not run in real-time and so is currently limited to use with systems where the secondary path does not change significantly and can be characterized offline.

4.2. Genetic algorithm results

(1) Swept tone noise

The GA was unable to produce a design that had lower eigenvalue span than the flattened magnitude design when optimizing for the entire range of frequencies from 0–400 Hz. There were not enough degrees of freedom in the design variables to get a better result. The frequency range for swept tone noise was reduced to a much smaller range to see if the genetic algorithm could improve the span of the eigenvalues in a smaller range. The GA was run for swept tone noise in the range 60–90 Hz with 128 filter coefficients. The results for 60–90 Hz are shown in Figures 6 and 7. Figure 6 shows the original- and new-modified magnitude coefficients, and Figure 7 shows the resulting eigenvalues. As before, the eigenvalues in both the original and modified case have been normalized by the largest of the original eigenvalues. The eigenvalues from the genetically optimized magnitude coefficients are more uniform. The eigenvalue span for the genetic algorithm model approach was 1.08,

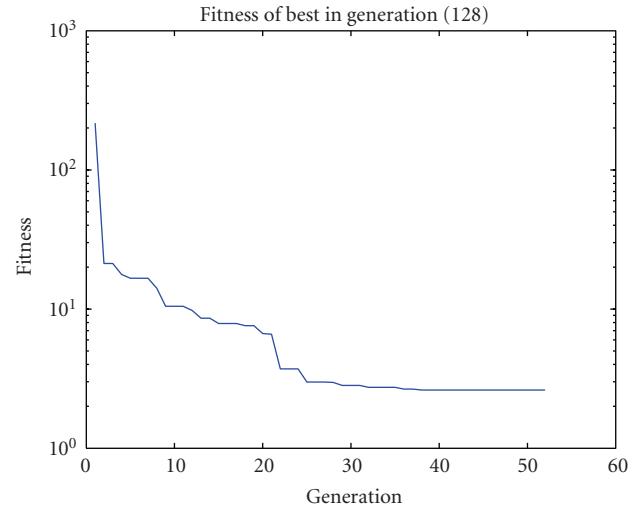

Figure 8: Fitness history for genetic optimization of 128-coefficient Sys ID model.

which is improved over both the eigenvalue span of 4.578 and 2.45 from the original and the flattened models, respectively.

(2) Multiple tone noise

The GA was also run for the reference signal containing six offbin tones, as described in Section 4.2, for 128 and 256 filter coefficients. The genetic algorithm was able to find a magnitude response that is unlike the X-inverse model and reduces the eigenvalue span to 5.8 for 128 coefficients and 5.3 for 256 coefficients. These values can be compared to the results for the other methods shown in Table 1, which have span values typically several orders of magnitude higher. Figure 8 shows the fitness history of the best design in each

Table 2: Comparison of eigenvalue span for original and GA magnitude coefficients for offbin tones shifted in frequency from the values for which the GA optimized the model.

	f shift	−10	−6	−4	−2	0	2	4	6	10
Original model	128 span	193.5	209.3	217.5	220.7	216.8	213	201.1	202.2	392.7
	256 span	64.4	265.5	444.0	361.7	238.5	169.6	174.8	500.0	1240.1
Genetic model	128 span	9.0	5.1	4.3	5.0	5.8	7.6	9.9	12.8	24.4
	256 span	23.9	11.3	28.2	13.0	5.3	12.9	51.4	132.0	1309.2

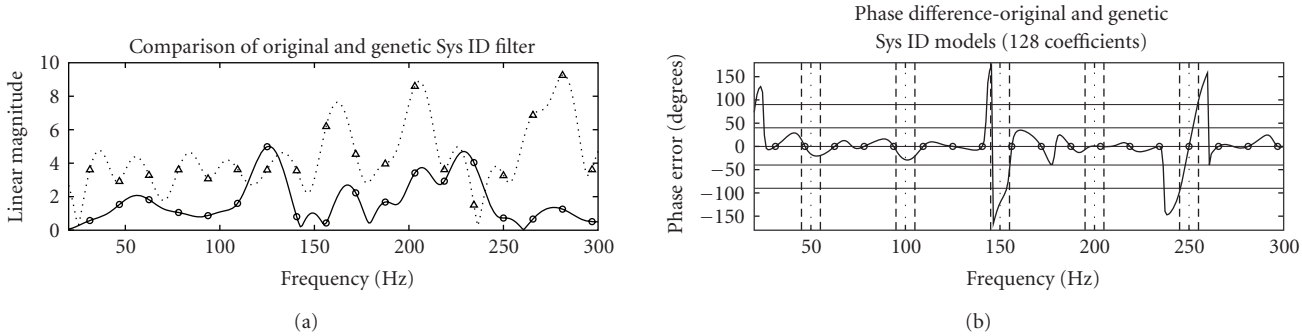

Figure 9: Magnitude of original and genetic 128-coefficient models along with the phase error in the genetic model.

generation of the 128-coefficient optimization and gives an idea of the dynamics of the genetic optimization. The fitness is the span plotted on a logarithmic scale.

The optimized magnitude coefficients found by the genetic algorithm are specific to the noise problem given to the genetic algorithm. If the tones shift in frequency or change in amplitude, the result is no longer guaranteed to be an optimum result. To see how sensitive the genetic algorithm model is to shifts in the tonal frequencies, the eigenvalue span for reference signals with all tones shifted by +/− 2 Hz up to +/− 10 Hz was calculated. This is compared to the original model in Table 2. In general, the farther the tones get from the frequencies for which the magnitude was optimized, the worse the span gets. It is difficult to predict how sensitive a genetic model will be for any given application without first performing the optimization. The sensitivity will depend on how much the magnitude response of the genetic model varies near the frequencies for which it was optimized. The phase is guaranteed to be within acceptable error +/− 5 Hz from the tonal frequencies by the GA and so the design remains robust in terms of stability for changes within this range. Where more shift in the tones is anticipated the GA can be constrained accordingly. The magnitude of both the original and genetic 128-coefficient models is plotted together in Figure 9 along with the phase error in the genetic model (difference between the two).

5. EXPERIMENTAL RESULTS

Experiments were performed to verify that the reduction in eigenvalue span demonstrated in Section 4 also leads to better ANC performance. First, the experimental setup will be explained, then ANC results for swept sine noise over the three ranges (60–90 Hz, 90–120 Hz, and 120–150 Hz) and for multiple tone noise (at offbin frequencies) will be shown.

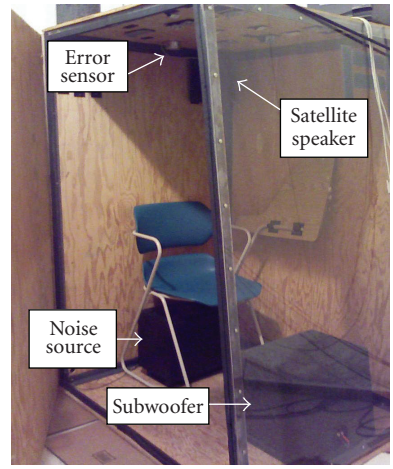

Figure 10: Photo of inside of mock cab.

5.1. Experimental setup

The experiments were conducted inside a mock cabin enclosure with nominal dimensions of 1.0 m × 1.5 m × 1.1 m. The cabin has a steel frame, 0.01 m thick plywood sides, and a 0.003 m thick Plexiglas front panel. A speaker placed under a chair served as the primary sound source, and two loudspeakers were setup in a single channel control configuration. A crossover circuit routed the low-frequency content (below 90 Hz) to a subwoofer on the floor of the cab, and the high-frequency content (above 90 Hz) to a satellite

Table 3: Comparison of control performance using original, flattened, and genetic $\hat{h}(t)$ models for swept tone noise.

Frequency range	Type of $\hat{h}(t)$ model	μ ($0.1^{*}\mu_{\max}$)	Error Mic avg. reduction (dB)	Reproducibility (dB)	Additional reduction compared to original (in dB)
60–90 Hz	Original	1e-8	14.8	0.16	
	Flattened	3e-8	21.9	0.37	7.1
	Genetic	5e-8	20.8	0.17	6.0

speaker mounted in the top corner of the cab, near the back. An error microphone was placed on the ceiling near where an operator's head would be. The performance of the algorithms will be reported at the error sensor. Figure 10 shows the cab, error sensor, and speakers.

The adaptive control filter consisted of 32 taps for swept tone noise and 100 taps for multiple tone noise. Secondary path transfer functions were modeled with either 128 or 256 taps. The convergence coefficient, μ, was determined experimentally by finding the largest stable value for the noise signal under test and then scaling it back by a factor of ten to ensure stability. All input channels were simultaneously sampled at 2 kHz, and all input and output signals had 16 bits of resolution. Fourth-order Butterworth low-pass filters (400 Hz cutoff) provided antialiasing and reconstruction of input and output signals, respectively.

5.2. Experimental results—swept tone noise

Each $\hat{h}(t)$ model was tested for swept tone noise over the frequency ranges 60–90 Hz, 90–120 Hz, and 120–150 Hz. A test signal was created for each frequency range that consisted of a sine wave being swept up and down over the frequency range at a rate of 2 Hz/sec. The time-averaged sound pressure level (SPL) over the entire duration of the test signal was measured with and without control running. Each measurement was performed three times for computation of an average and to give a sense of the measurement's reproducibility. The attenuation (the difference in SPL with control off and on) using all three $\hat{h}(t)$ models is shown in Table 3. The "reproducibility" shown in Table 3 was calculated in the same manner as a standard deviation, although it is recognized that the small sample size precludes referring to the result as a statistically valid standard deviation.

In the range from 60–90 Hz, the SPL before running control was about 95 dB (computed over the entire frequency range) and about 73 dB with control for the flattened magnitude model. Figure 11 shows a plot of the frequency spectrum for both control on and control off for the 60–90 Hz range.

The data show that control with the genetic and the flattened models significantly outperformed control with the original $\hat{h}(t)$ model. For the range 60–90 Hz, control with the genetic and flattened models outperformed the original control by 6-7 dB, with control with the flattened model providing 1 dB more control than the genetic model. Experiments for other frequency ranges were also done with similar results.

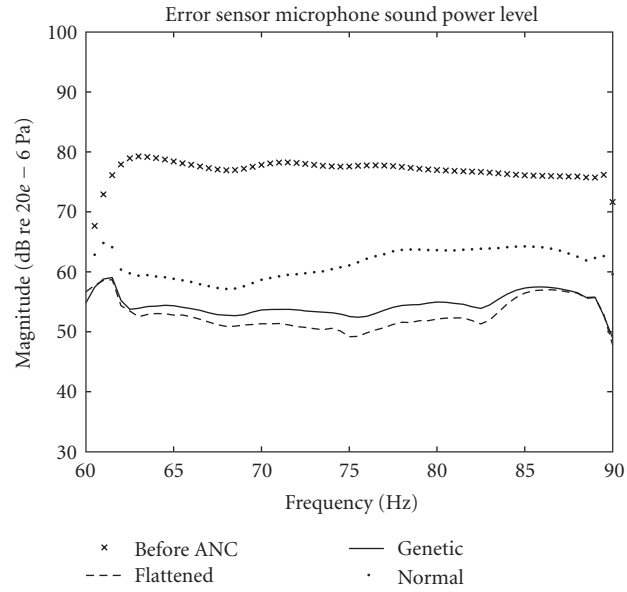

Figure 11: Sound pressure level (SPL) at the error sensor for 60–90 Hz.

5.3. Experimental results—multiple tone noise

Multiple tone noise ANC experiments in the mock cab were done using 128 and 256-coefficient original, X-inverse, and genetic secondary path models with the reference signal consisting of multiple offbin frequency tones, as described in Section 4.2. For these tests, three 10-second time records of the error signal were taken as follows:

(1) stationary error signal with control off;

(2) converging error signal from the time control was turned on;

(3) stationary error signal after the algorithm had converged to its eventual steady state level.

The measured performance for each test case was the eventual amount of attenuation (in dB) at the error sensor, calculated from the first and third time records and the convergence time in seconds from the second-time record. The convergence time was taken to be a measure of how long it took the error signal, from the time that control was enabled, to reach $1/e$ of its initial value (about 9 dB attenuation), where e is the base of the natural logarithm. The reason for choosing this was that the convergence time essentially becomes a measure of the rate of attenuation,

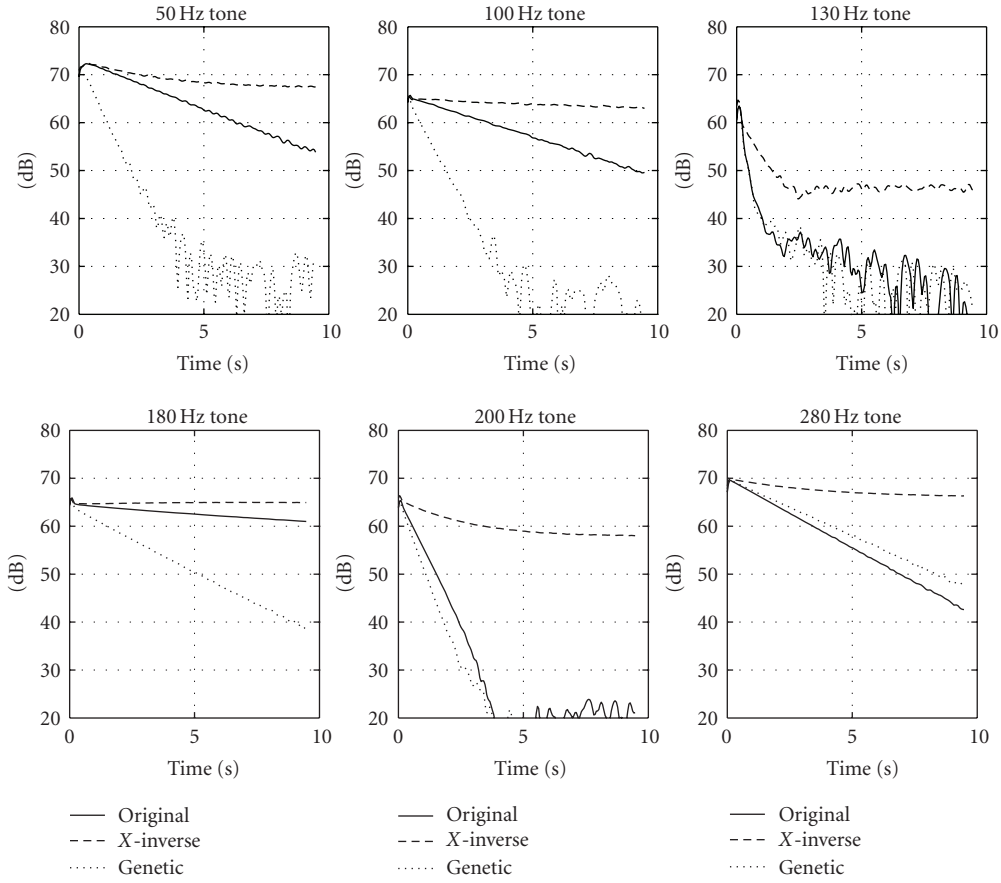

Figure 12: Learning curves for individual tones of multiple noise test case for 128-coefficient original, X-inverse, and genetic models.

Table 4: Comparison of control performance using original, X-inverse, and genetic $\widehat{h}(t)$ models for multiple tone noise.

Sys ID type	Convergence time (sec)	Eventual reduction (dB)	Eignvalue span
Normal 128	3.9	−19.5	217
Normal 256	6.3	−16.9	239
X-inverse 128	10+	−4.6	16
X-inverse 256	10+	−2.6	991
Genetic 128	1	−25.9	2.3
Genetic 256	2.2	−26.1	2.4

which was felt to be useful when comparing cases where the overall level of attenuation may be significantly different. These results are summarized in Table 4. When a signal did not converge to $1/e$ of its initial value during the second-time capture, it is reported as 10+ seconds. The actual convergence time for these measurements was not calculated. The genetic models for both 128 and 256 coefficients were better than both the original and X-inverse models for both measures of performance. Models that gave lower eigenvalue span performed better with the exception of the 128-coefficient X-inverse model whose performance was worse than expected.

Based on the eigenvalue span, the 128 coefficient X-inverse model should have been a significant improvement over the original model. The reason for the poor performance is a result of phase errors introduced by modifying the magnitude values. As for the magnitude coefficients, preserving the phase coefficients guarantees the phase response will be the same at frequency bins, but changing the magnitude coefficients does have an influence on the response in between these bins. As noted previously, as long as the phase response modeled by the secondary path estimate is within 90° of the true phase response, the algorithm will be stable. Comparing the zero-padded phase response for the original 128-coefficient model and the X-inverse model reveals that the phase difference between the two at 100 Hz (one of the tonal frequencies) approaches that limit. While the errors in the original model of the secondary path are not known, it is assumed that it is a better estimate and the X-inverse model deviating from it by close to 90° is the cause for the poor performance.

Figure 12 shows learning curves for the individual tones in the multitone test case for the 128-coefficient model. These are slices along tonal frequencies from a spectrogram of the converging error signal. These plots show the different rates of convergence for the individual tones in the noise. The genetic model converges faster and to a lower level than the other models at all tones except 280 Hz where performance is similar for the original model. This is the fastest converging mode for the algorithm for all secondary path models. The

X-inverse model shows that the 180 Hz tone is diverging due to the >90° phase error at that frequency (see Figure 5).

6. CONCLUSIONS

Use of a genetic algorithm to find optimum values for the magnitude coefficients of the secondary path estimate for the FXLMS algorithm while preserving the phase of $\hat{\mathbf{H}}(z)$ has been shown to reduce the variation in the eigenvalues of the filtered-x autocorrelation matrix.

ANC in a mock cab using control with both the flattened and genetic $\hat{\mathbf{h}}(t)$ models provided as much as 6-7 dB additional attenuation over control with the original $\hat{\mathbf{h}}(t)$ model. For these specific swept tone noise tests, the genetically optimized $\hat{\mathbf{h}}(t)$ algorithm did not provide any additional benefit over the flattened model, even though the eigenvalues were more uniform. It is possible that the improved eigenvalues resulting from the genetically optimized model could lead to better performance in other applications.

When considering the more general case for multiple tone noise, with tonal frequencies not corresponding exactly to frequency bins, control with the X-inverse $\hat{\mathbf{h}}(t)$ models performed worse than the original $\hat{\mathbf{h}}(t)$ model. Genetic $\hat{\mathbf{h}}(t)$ models were shown to give 6–9 dB additional attenuation with faster convergence times.

Use of a genetic algorithm as an optimization method in implementing the EE-FXLMS algorithm extends its utility and increases the potential benefit of its use over the FXLMS algorithm. With this method, the eigenvalue disparity can be reduced while assuring performance limiting phase errors are not introduced.

The optimization performed on the secondary path estimate in the EE-FXLMS algorithm in this paper is limited to applications where the secondary path model (at least the phase response) is relatively stable since the secondary path is only characterized and optimization performed as part of the setup of an ANC system. Further work could be done to implement the EE-FXLMS with genetic optimization for a changing secondary path with an online Sys ID routine [14]. The secondary path can be characterized online periodically and the eigenvalue equalization performed in the background while control is running. Everytime a newly optimized secondary path model becomes available, it can be updated and used to run control. The time it would take to get a new-optimized model for the secondary path estimate would be set by the time it takes for the genetic algorithm to execute.

REFERENCES

[1] D. R. Morgan, "An analysis of multiple correlation cancellation loops with a filter in the auxiliary path," *IEEE Transactions on Acoustics, Speech, and Signal Processing*, vol. 28, no. 4, pp. 454–467, 1980.

[2] J. C. Burgess, "Active adaptive sound control in a duct: a computer simulation," *Journal of the Acoustical Society of America*, vol. 70, no. 3, pp. 715–726, 1981.

[3] S. M. Kuo and D. R. Morgan, "Adaptive transversal filters," in *Active Noise Control Systems: Algorithms and DSP Implementations*, J. G. Proakis, Ed., pp. 33–35, chapter 2, John Wiley & Sons, New York, NY, USA, 1996.

[4] R. L. Clark and G. P. Gibbs, "A novel approach to feedforward higher-harmonic control," *Journal of the Acoustical Society of America*, vol. 96, no. 2, pp. 926–936, 1994.

[5] S. M. Lee, H. J. Lee, C. H. Yoo, D. H. Youn, and I. W. Cha, "An active noise control algorithm for controlling multiple sinusoids," *Journal of the Acoustical Society of America*, vol. 104, no. 1, pp. 248–254, 1998.

[6] S. M. Kuo, X. Kong, S. Chen, and W. Hao, "Analysis and design of narrowband active noise control systems," in *Proceedings of the IEEE International Conference on Acoustics, Speech and Signal Processing (ICASSP '98)*, vol. 6, pp. 3557–3560, Seattle, Wash, USA, May 1998.

[7] S. J. Elliott and J. G. Cook, "A preconditioned LMS algorithm for rapid adaptation of feedforward controllers," in *Proceedings of the IEEE International Conference on Acoustics, Speech and Signal Processing (ICASSP '00)*, vol. 2, pp. 845–848, Istanbul, Turkey, June 2000.

[8] J. K. Thomas, S. P. Lovstedt, J. D. Blotter, and S. D. Sommerfeldt, "Eigenvalue equalization filtered-x algorithm for the multi-channel active noise control of stationary and non-stationary signals," submitted to *Journal of the Acoustical Society of America*.

[9] C. C. Boucher, S. J. Elliott, and P. A. Nelson, "Effect of errors in the plant model on the performance of algorithms for adaptive feedforward control," *IEE Proceedings F*, vol. 138, no. 4, pp. 313–319, 1991.

[10] S. J. Elliott and P. A. Nelson, "Active noise control," *IEEE Signal Processing Magazine*, vol. 10, no. 4, pp. 12–35, 1993.

[11] B. Widrow and S. D. Stearns, *Adaptive Signal Processing*, Prentice-Hall, Englewood Cliffs, NJ, USA, 1985.

[12] L. Davis, *Handbook of Genetic Algorithms*, Van Nostrand Reinhold, New York, NY, USA, 1991.

[13] D. Goldberg, *Genetic Algorithms in Search, Optimization, and Machine Learning*, Addison-Wesley, Reading, Mass, USA, 1989.

[14] S. M. Kuo and D. R. Morgan, "On-line secondary path modeling techniques," in *Active Noise Control Systems: Algorithms and DSP Implementations*, J. G. Proakis, Ed., pp. 213–240, chapter 7, John Wiley & Sons, New York, NY, USA, 1996.

Hindawi Publishing Corporation
Advances in Acoustics and Vibration
Volume 2008, Article ID 574806, 8 pages
doi:10.1155/2008/574806

Research Article

Design and Calibration Tests of an Active Sound Intensity Probe

Thomas Kletschkowski and Delf Sachau

Department of Mechanical Engineering, Faculty of Mechatronics, Helmut-Schmidt-University/University of the Federal Armed Forces Hamburg, Holstenhofweg 85, 22043 Hamburg, Germany

Correspondence should be addressed to Thomas Kletschkowski, kletsch@hsuhh.de

Received 22 November 2007; Revised 4 February 2008; Accepted 13 March 2008

Recommended by Marek Pawelczyk

The paper presents an active sound intensity probe that can be used for sound source localization in standing wave fields. The probe consists of a sound hard tube that is terminated by a loudspeaker and an integrated pair of microphones. The microphones are used to decompose the standing wave field inside the tube into its incident and reflected part. The latter is cancelled by an adaptive controller that calculates proper driving signals for the loudspeaker. If the open end of the actively controlled tube is placed close to a vibrating surface, the radiated sound intensity can be determined by measuring the cross spectral density between the two microphones. A one-dimensional free field can be realized effectively, as first experiments performed on a simplified test bed have shown. Further tests proved that a prototype of the novel sound intensity probe can be calibrated.

1. INTRODUCTION

Noise pollution of enclosed interiors (e.g., aircraft cabins) results in a limitation of human comfort. If noise reduction techniques will be applied in such situations with success, the sound sources at the interior wall that surrounds a standing wave field have to be identified. Especially the localization of low-frequency hot spots in weakly damped enclosures requires the application of advanced measurements techniques. Several noise source localization methods have been established. The methods range from simple sound pressure or sound intensity measurements to more sophisticated methods as beamforming [1] and acoustic holography [2, 3]. A drawback in applying these techniques is that free-field conditions are required. Even though the free field requirement does not have to be met using the inverse boundary element method [4] or the inverse finite element method [5], a well-validated numerical model of the interior is needed, if these techniques will be applied with success.

To avoid the time and cost consuming processes of realizing artificial free-field conditions by introducing passive damping to the interior (which in addition changes the global characteristic of the investigated enclosure) or the need of sophisticated numerical models, a prototype of a new mechatronic sound intensity probe with an active free field (SIAF), see [7], that only influences the local impedance was developed. The fundamental idea is to generate acoustic free-field conditions by active noise control. As shown in Figure 1 (left), the three-dimensional sound field in front of the interior wall is reduced to one dimension by a mechanical device with sound-hard walls. This device is terminated by a loudspeaker. The integrated microphone pair is used to separate the remaining one-dimensional sound field inside the device into its incident and the reflected components. The reflected wave is cancelled by active noise control, as shown in Figure 1 (right). In contrast to common active noise control (ANC) techniques for ducts (e.g., [8, 9]) or common sound tubes with standing wave fields that are used to determine material properties, see [10], the application of the SIAF-approach allows sound intensity measurements in (global) standing wave fields using the local free field of the device.

In a sound field consisting of a free field and a reverberant part, the real part of the time averaged sound intensity determines the free field part. This part vanishes in a purely diffuse, reverberant sound field, and in a plane standing

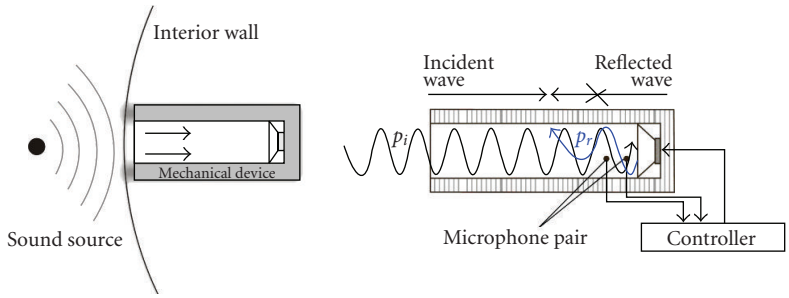

Figure 1: (left) Application and (right) functional principle of an intensity probe with an active free field [6].

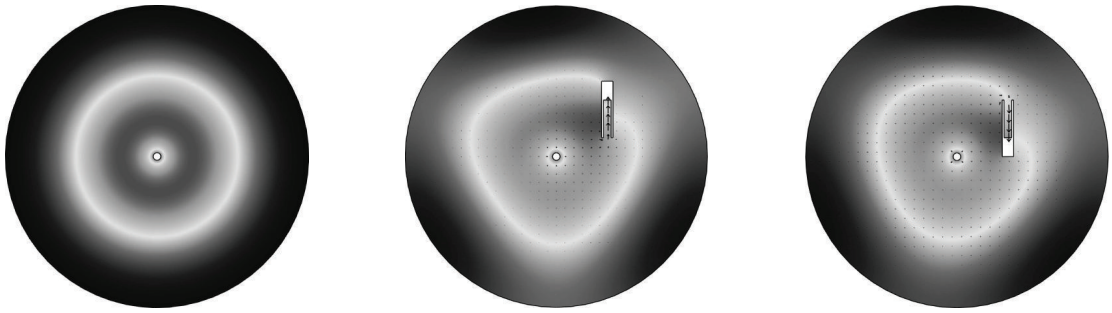

Figure 2: (a) Standing wave field with inactive SIAF and (b) and (c) intensity flow into active SIAF.

wave propagating inside a rigidly terminated enclosure, as shown in [11]. If a spherical wave impinges on the sound soft boundary of a common (passive) sound tube, parts of its energy are reflected in amplitude and phase. In this case, a source is not characterized correctly. A conventional sound tube (without active control) that is placed directly in front of the interior wall would change the impedance of the area of investigation. The resulting impedance could be determined by standard methods, see [10], but this value would vary from point to point. In contrast to this unwanted situation, the SIAF-approach enables both the energy transport from the source into the mechanical device as well as its quantification under comparable boundary conditions inside the mechanical device. Because of the free field inside the probe, the SIAF acts as a local sound absorber. For this reason, the effect of the device on a source would be reduced. A SIAF can therefore be applied for sound source localization, especially in weakly damped interior noise fields at low frequencies. This would—in general—not be possible, if a standing wave field without any energy transport would remain inside the mechanical device. Only the active free field ensures that every acoustic hot spot on the investigated interior wall may radiate into the local free field.

If a SIAF would be used in a standing wave field, but not directly in front of the interior wall, it would still act as a local sound absorber enabling an energy flow into the mechanical device due to active control. This situation is illustrated in Figure 2. Here, the (qualitative) sound pressure distribution as well as the intensity flow (symbolized by black arrows) was determined by two-dimensional time-harmonic ($f = 300\,\text{Hz}$) finite element simulations for an enclosure with sound hard boundaries. The sound source was placed in the center of the cavity. The SIAF is placed top right. The results shown in Figure 2(a) prove that no intensity flow can be measured if the SIAF is inactive. If the inner termination of the SIAF is described by a free-field impedance boundary condition ($Z = 428.75\,\text{kgm}^{-2}\,\text{s}^{-1}$), see Figures 2(b) and 2(c), an energy flow into the mechanical device is enabled. The direction of this energy flow varies with the spatial orientation of the probe, as shown in Figure 2. Therefore, inside the mechanical device it would only be possible to measure the local intensity in longitudinal direction which is—in general—not the magnitude of the intensity vector. Obviously, the localization of a single acoustic hot spot would be impossible, if the SIAF acts as a local absorber in the middle of the sound field. To identify a local source, the SIAF has to be used close to the interior boundary as shown in Figure 1 (left). The minimum working distance should be chosen in such a way that contact between the SIAF and the interior wall is excluded. The maximum working distance has to be small enough to ensure that an energy flow into the SIAF results only from a source that is located on the investigated part of the boundary. Assuming an upper frequency limit of 1kHz, due to the area of application of ANC, the maximum working distance should be lower than ten percent of the minimum wave length (e.g., 3 cm).

This paper is divided into four parts. The first explains the calculation of the reflected wave and the control concept. Furthermore, experimental results of tests that were performed on a simplified test bed are reported. The second part

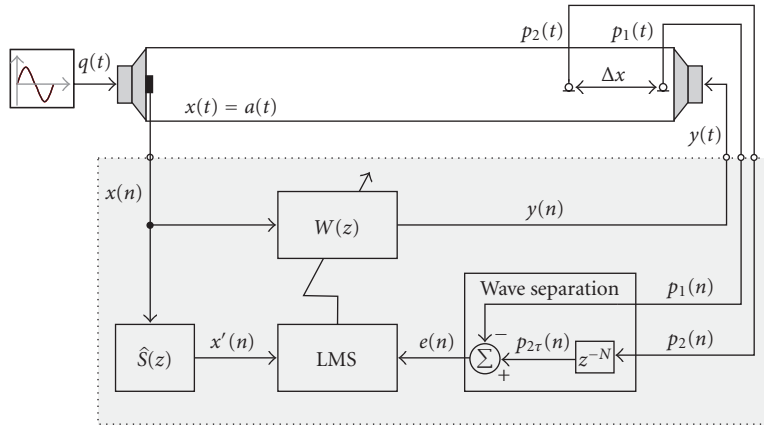

Figure 3: Block-diagram for SIAF-approach based on wave separation in time domain.

presents the results of calibration tests that were performed on a SIAF-prototype. A short summary is given in the third part of the paper.

2. CONTROL STRATEGY AND PROOF OF CONCEPT

To realize free-field conditions, the sound field inside the mechanical device has to be separated into its incident and reflected components. This separation can be performed in frequency as well as in time domain. As wave separation in frequency domain requires a frequency domain control algorithm, it was not applied. Instead, a time domain approach was used for time-discrete adaptive control, as illustrated in Figure 3.

As shown in [12], the reflected wave component of a one-dimensional standing wave field can be determined by employing two microphones and a time-delay. One of the SIAF microphones has to be placed in front of the canceling loudspeaker at $x = 0$, the other at a distance Δx. Assuming plane wave propagation, the total pressure at the discrete time step n picked up at the microphones is given by

$$\begin{aligned} p_1(n) &= p_i(0,n) + p_r(0,n), \\ p_2(n) &= p_i(\Delta x, n) + p_r(\Delta x, n) \\ &= p_i(0, n+N) + p_r(0, n-N), \end{aligned} \tag{1}$$

where the continuous time delay $\tau = T_s N = \Delta x/c$ is given by the separation distance Δx, the sample time T_s, the number of delayed time steps N, and the speed of sound c. If $p_2(n)$ is delayed by τ, the delayed sound pressure is defined as

$$p_{2\tau}(n) = p_2(n-N) = p_i(0,n) + p_r(0, n-2N), \tag{2}$$

and the error signal $e(n)$ that is calculated as follows

$$e(n) = p_{2\tau}(n) - p_1(n) = p_r(0, n-2N) - p_r(0,n) \tag{3}$$

represents the reflected wave only. As shown in [12], the calculation of the error signal fails, if the distance between the microphones equals a multiple of one half of the wave length, if (3) is analyzed for tonal excitation $p_r(0,n) = A\sin[2\pi f(nT_s - x/c)]$. As shown in [6], the time delay number N is limited by Shannon's law $1 \le N < T_{\min}/2T_S$, there $T_{\min}$ represents the periodic time of the highest frequency of interest $f_{\max}$.

As shown in Figure 3, the filtered reference least mean square (FxLMS) algorithm was used to update the coefficients of the adaptive finite impulse response (FIR) filter $W(z)$. These coefficients are used to generate the driving signal $y(n)$ for the canceling loudspeaker. The acceleration of the interior wall that in the simplest case is represented by the membrane on the noise source was used as reference signal $x(n)$ that is required for adaptive feed foreword control. A feedback controller would be independent of a reference signal. But, in contrast to an adaptive control scheme based on FIR filters, a feedback controller based on infinite impulse response (IIR) filters is not unconditionally stable, see [13]. Offline plant modeling based on the common least mean square algorithm was applied to identify the secondary path model $\hat{S}(z)$. As shown in [13], the single-channel leaky FxLMS algorithm can be summarized as follows.

(1) Adaptive filtering

$$y(n) = \mathbf{w}^T(n)\mathbf{x}(n), \tag{4}$$

where $y(n)$ is the controller output at the discrete time step n, $\mathbf{w}(n)$ is the $L \times 1$ column matrix of the filter coefficients for a FIR filter of length L, and $\mathbf{x}(n)$ is the $L \times 1$ column matrix of the buffered reference signal $\mathbf{x}(n)$.

(2) Single-channel prefiltering

$$\mathbf{x}'(n) = \sum_{i=0}^{I-1} \hat{s}_i(n)\mathbf{x}(n-i), \tag{5}$$

where I is the order of the FIR filter $\hat{S}(z)$.

(3) Weight vector update

$$\mathbf{w}(n+1) = \nu\mathbf{w}(n) + \mu\mathbf{x}'(n)e(n), \tag{6}$$

where ν is the leakage factor, μ is the convergence factor, and $e(n)$ is the error signal at the discrete time step n.

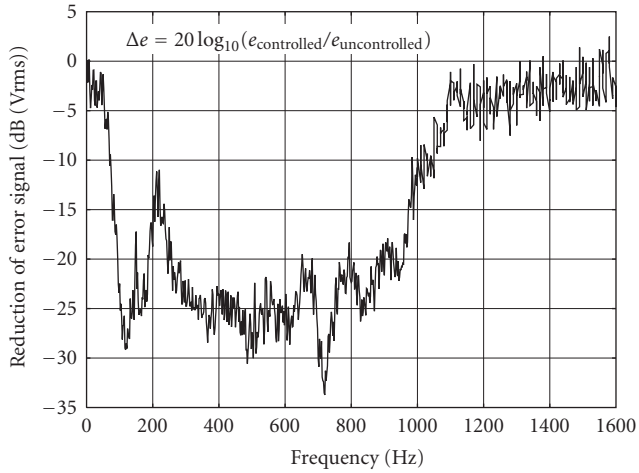

Figure 4: Broadband noise reduction obtained by SIAF approach applied to a sound tube.

The choice of a proper filter length L depends on parameters such as the characteristics of the error signal (e.g., tonal or broadband), the impulse response of the secondary path, and the computing power of the applied signal processor. For tonal excitation, a filter length of $L = 2$ would be sufficient to determine amplitude and phase of the control signal as well as to model the secondary path. In practice, however, a filter length of $L = 4$ can be advantageous, because of the nonideal transfer behavior of many electro-dynamic loudspeakers at very low frequencies. If broadband disturbances have to be controlled using a certain sampling frequency, the number of filter taps must be high enough to model the impulse response of the secondary path in the analyzed frequency band but small enough to guarantee causality.

To test the performance of the SIAF approach, the algorithm was implemented on a real time processor (type: dSpace DS1103). The time delay number was set to $N = 2$. As motivated by Figure 3, a sound tube with a square cross-section (edge length $a = 92$ mm) and upper frequency limit $f_u \approx 1864$ Hz (according to [10, equation (2)]) terminated by electro-dynamical loudspeakers (type: SPEAKA MT 60/80) was used as a simplified test bed for first experiments. Two microphones (type: Ono Sokki MI-1233) were used. Microphone 1 was placed in front of the canceling loudspeaker and microphone 2 in a distance of $\Delta x = 13.7$ cm. In compliance with [10, equation (4)], the upper frequency limit was reduced to $f_{\text{ured}} \approx 1152$ Hz for this reason. An accelerometer (type: B&K 4374) that was amplified by a signal conditioner (type: B&K Nexus 2692) was used to detect the reference signal. Furthermore, several analogue high- and low-pass filters, respectively, (type: Kemo VBF21) were applied to avoid aliasing. A multichannel FFT analyzer (type: Ono Sokki DS2100) was used for data analysis.

The reduction of the reflected waves was analyzed for a broadband disturbance with $f_{\max} < f_{\text{ured}}$. The system was excited by frequency-banded white noise ($50\,\text{Hz} \leq f \leq 1\,\text{KHz}$). Therefore, a filter length of $L = 128$ was used for the adaptive weight vector $\mathbf{w}(n)$ as well as for the secondary path model $\hat{S}(z)$. The sampling frequency was set to $f_S = 5$ kHz. The results shown in Figure 4 prove that the controller cancels a reflected wave, if and only if the associated frequency is detected by the reference sensor. A total reduction of -16.2 dB was achieved in the analyzed frequency band. The SIAF-control-strategy was applied successfully. Sound intensity was not determined during this test.

3. DESIGN OF A PROTOTYPE AND CALIBRATION TESTS

A first realization of a SIAF that is based on commercial components is shown in Figure 5(a). It consists of a sound source (type: B&K 4295) and a self-made cylindrical adapter (inner diameter $d = 38$ mm). Two phase-matched microphones (type: B&K 4295) were integrated into this adapter. A portable FFT analyzer (type: B&K 3560B with a phase match of $\pm 0.017°$ at 50 Hz using B&K sound intensity probes) was used for data processing. The microphone spacing was set to $\Delta x = 10$ cm. According to [10, equation (4)], the upper frequency is given by $f_{\text{ured}}^{\text{SIAF}} \approx 1543$ Hz.

An anechoic chamber was used to test the possibility of calibrating the SIAF prototype. The experimental setup is shown in Figure 5(b). An electro-dynamical loudspeaker (type: PAB-8MK2) was used as the acoustic source, and a free-field microphone (type: B&K 4188) was applied to measure the sound pressure level at a fixed reference point. An accelerometer (type: B&K 4374), amplified by a signal conditioner (type: B&K Nexus 2692), was used to assure a precise reproduction of the excitation and to detect the reference signal. The radiated sound intensity was measured for the third-octave band center frequencies between 80 Hz and 500 Hz. First reference data were collected by a conventional sound intensity probe (type: B&K 3595 with microphone pair 4197 using a spacer of 12 mm). The measurements were then repeated using the SIAF prototype. Signal processing was performed on a power computer (type: dSpace DS1103). Tonal disturbances were used to test the SIAF prototype. Therefore, a filter length of $L = 4$ was used for the adaptive weight vector $\mathbf{w}(n)$ as well as for the secondary path model $\hat{S}(z)$ which was remodeled for every frequency. The time delay number was set to $N = 2$, and a sampling rate of $f_S = 10$ kHz was used for these tests.

The results shown in Figure 6(b) prove that the controller was capable of reducing the reflected wave for all analyzed frequencies. Only minor sound pressure deviations between the SIAF microphones were measured. The results presented in Figure 6(b) also confirm sound propagation in a plane wave field, because the same amount of energy was determined at the two measurement points. For this reason and because of the fact that the distance between the loudspeaker membrane and the front side microphone of the SIAF was smaller than the triple diameter of the tube, compare with [10], additional corrections for the losses along the boundaries of the tube (needed for higher frequencies, $f > 500$ Hz) were not taken into account.

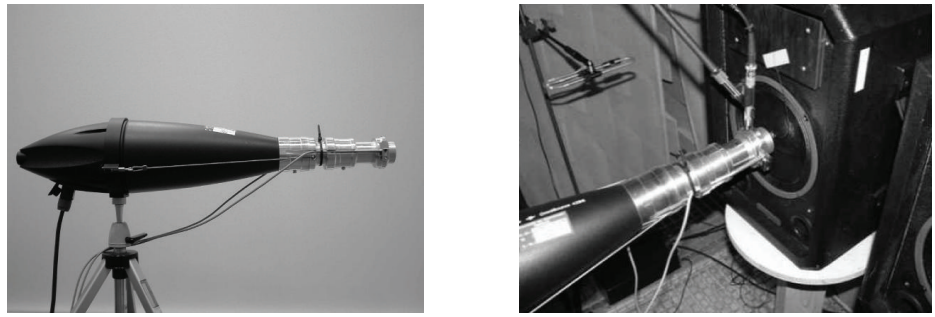

(a) (b)

Figure 5: (a) SIAF prototype, see [6], and (b) experimental setup for calibration tests.

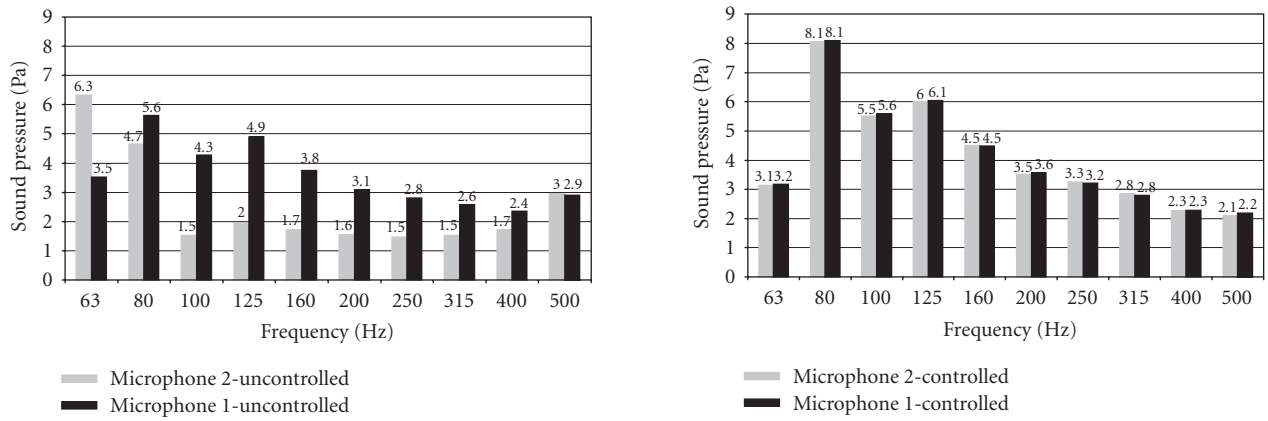

(a) (b)

Figure 6: Sound pressure at the SIAF microphones: (a) uncontrolled and (b) controlled.

As proposed in [11], the sound intensity was calculated from the imaginary part of the cross-spectral density $G_{12}(f)$ between the two SIAF microphones (*p-p* probe):

$$I(f) = -\frac{1}{2\pi f \rho \Delta x} \mathrm{Im}[G_{12}(f)], \tag{7}$$

where ρ is the density of the fluid. An alternative approach is given by the application of the combined sound-pressure, particle-velocity probe (*p-u* probe) that is described in [14]. This probe consists of a small electret condenser microphone and a particle velocity transducer. The latter is based on the technique of the acoustic intensity meter that was proposed in [15]. Particle velocity measurements using transducers that were analyzed in [16] were only possible by using a small fan to generate a permanent air flow. Because of the nonlinearities of these transducer types, the permanent air flow is needed to define the working point of the sensor. The *p-u* probe, presented in [14], is independent of a permanent air flow, and its application, especially in plane standing wave fields, ensures that at least one of the transducers is not located at a nodal point. If, however, the sound pressure level exceeds the upper sound level—110 dB, see [17]—of the electret microphone, the pressure sensor of the *p-u* probe can cause nonlinearities, as shown in [18]. This operating mode must be avoided, if a linear controller is applied. As shown in [14], the application of a *p-u* probe is advantageous, if the influence of background noise—coming from sources outside the measurement plane—on the phase mismatch between the sensors has to be reduced. In contrast to the phase mismatch between the two microphones of a *p-p* probe, the *p-u* phase mismatch is exacerbated in strongly reactive sound fields (e.g., in a plane standing wave), see [14]. Furthermore, it is more difficult to calibrate a *p-u* probe than a *p-p* probe, as concluded in [14].

The SIAF approach requires a wave separation in the time domain that is based on two microphones. Therefore, sound intensity measurement was performed according to (7). This procedure enables a direct comparison between the sound intensity that is measured using the SIAF approach and the sound intensity that is determined by a conventional *p-p* probe. The measurement limitations of this approach for sound intensity measurement are summarized in [11]. Neglecting errors coming from off-axis measurements, the quality of the results is determined by the phase mismatch error, the finite difference approximation error, and the near field error.

The phase mismatch between the two channels in the analyzing system determines the "low-frequency limit," see [11]. As written in [11], the maximum phase mismatch might be $\pm 0.3^\circ$ for a good probe and analyzer combination.

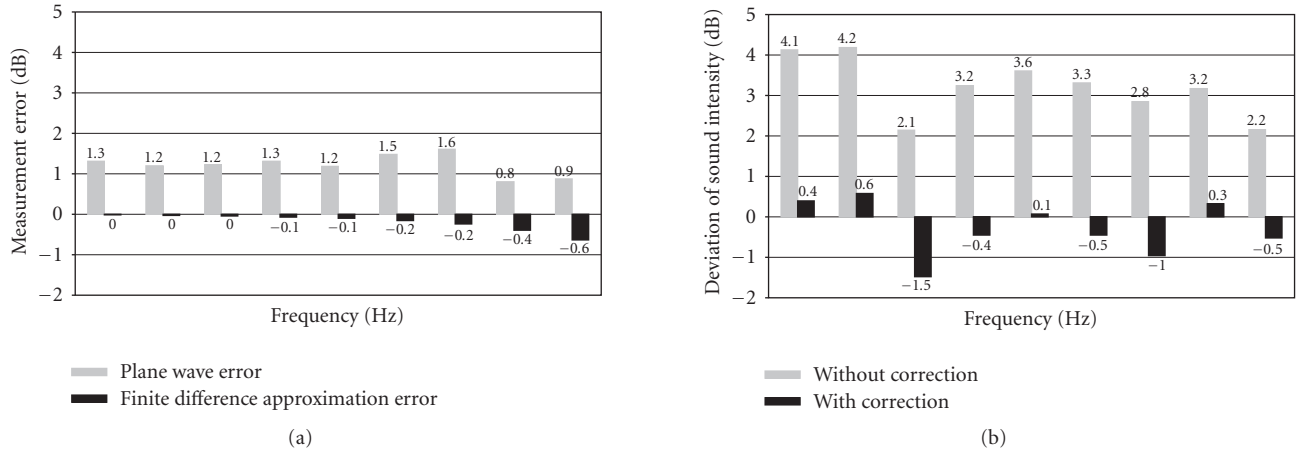

Figure 7: Effect of errors (a) on sound intensity measurement and (b) deviation in sound intensity.

The calibration tests were performed using phase matched microphone-analyzer combinations. In this case, the phase mismatch at low frequencies depends only on the microphone spacing. Using a 12 mm spacer for the conventional sound intensity probe and a spacing of 10 cm for the SIAF, the change of phase over the spacer is given by $\pm 1^\circ$ and $\pm 8.4^\circ$ for the SIAF and for the lowest analyzed frequency, respectively. Hence, phase mismatch errors were not taken into account during the calibration tests. If the SIAF concept is applied using a microphone-analyzer combination that is not perfectly calibrated in phase, phase calibration (e.g., by a procedure based on switching the microphones as described in [10]) is required. As also outlined in [11], the finite difference approximation error of an ideal two-microphone sound intensity probe in a plane wave of axial incidence is given by

$$E_{\mathrm{FD}}(f) = 10\log_{10}\frac{\sin k\Delta x}{k\Delta x}, \quad \text{with } k = \frac{2\pi f}{c}. \tag{8}$$

This error determines the "high-frequency limit" of a *p-p* probe. It has to be taken into account that, because the pressure gradient that is needed to calculate the particle velocity is approximated by a simple finite difference scheme every time, the intensity is measured. If a *p-u* probe is used for sound intensity measurements, E_{FD} can be avoided, because the particle velocity is measured directly. A finite difference approximation of the pressure gradient is not needed in this case. The "high-frequency limit" as well as the "low-frequency limit" of a *p-u* probe is determined by the frequency response curves of the microphone and the particle-velocity transducer.

Using the calculations for a two microphone probe in a sound field of a point source radiating into a free field, as presented in [11], the near field error can be described as follows:

$$E_{\mathrm{NF}}\left(\frac{\Delta x}{x}\right) = -10\log_{10}\left(1 - \frac{1}{4}\left(\frac{\Delta x}{x}\right)^2\right). \tag{9}$$

The near field error described by (9) is a function of the separation distance between the two microphones Δx and the distance from the source to the middle point between the microphones x. A negligible near field error of 0.063 dB was determined for the conventional sound intensity probe with the 12 mm spacer ($\Delta x = 1.2$ cm, $x = 5$ cm), but it was found that an overestimation of $E_{\mathrm{NF}} = 2.4$ dB has to be taken into account for a SIAF ($\Delta x = 10$ cm, $x = 7.6$ cm) without a surrounding tube.

In addition to these measurement limitations, and because of the tube that surrounds the SIAF-microphone pair, the deviations between plane wave propagation in one dimension inside the SIAF and spherical wave propagation in three dimensions have to be taken into account by RMS values of the measured sound pressure:

$$E_{\mathrm{PW}}(f) = 20\log_{10}\left(\frac{\tilde{p}_2}{2\cdot 10^{-5}\,\mathrm{Pa}}\right) - 20\log_{10}\left(\frac{\tilde{p}_{\mathrm{Ref}}}{2\cdot 10^{-5}\,\mathrm{Pa}}\right). \tag{10}$$

This error is in the following called plane wave error. It was calculated as the difference between the sound pressure level measured at SIAF-microphone 2 and the sound pressure level measured at the reference microphone. The latter was placed above the actively controlled SIAF, as shown in Figure 5(b).

The frequency dependencies of the plane wave error (that was derived from measurements) as well as of the finite difference approximation error, given by (8), are shown in Figure 7(a). It can be seen that the first results in an overestimation of the measured sound pressure level. The second leads to an underestimation of the measured sound intensity level.

The deviation $\Delta I = I_{\mathrm{SIAF}} - I_{\mathrm{Conv}}$ between the sound intensity that was measured using the SIAF prototype and the sound intensity that was determined by the conventional probe is shown in Figure 7(b). It was found that these deviations can be reduced, if (a) the near field error, (b) the finite difference approximation error, and (c) the plane wave error are used to calculate a corrected deviation $\Delta I_{\mathrm{corr}} = \Delta I - (E_{\mathrm{FD}} + E_{\mathrm{NF}} + E_{\mathrm{PW}})$. The corrected values are also shown in Figure 7(b). Without correction, the measurement error was at least 2.1 dB. Using the correction based on the three

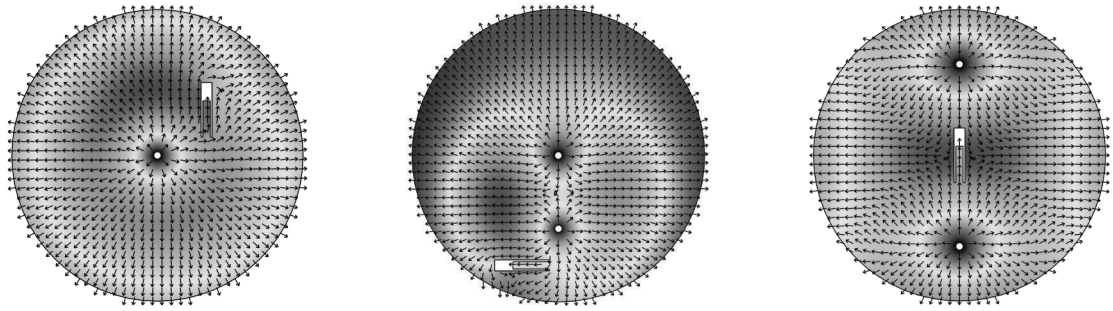

(a) (b) (c)

Figure 8: Pressure distribution and intensity flow in a free field with (a) one and (b) and (c) two sources.

Table 1: Sound intensity measured in an enclosure using the SIAF-prototype.

f/Hz	100	125	250	500
I_{SIAF}/Wm^{-2} without control	−0.043	−0.018	−0.002	−0.004
I_{SIAF}/Wm^{-2} with control	+0.056	+0.048	+0.018	+0.006
I_{Conv}/Wm^{-2} without control	+0.536	+0.107	+0.292	+0.348

relevant error types, the mean deviation in the analyzed frequency band, calculated as

$$\Delta\bar{I} := 10\log_{10}\left(\frac{1}{N_f}\sum_{i=1}^{N_f}\frac{10^{|\Delta I_i|/10}}{10^{-12}\,\mathrm{Wm}^{-2}}\right), \tag{11}$$

where N_f (representing the number of analyzed frequencies) could be reduced from 3.24 dB down to 0.61 dB. The maximum deviation was reduced from 4.2 dB down to −1.5 dB. A minimum deviation of 0.1 dB was found at 200 Hz after correction. The results prove that the SIAF prototype can be calibrated successfully under well-defined boundary conditions. For practical use, however, a calibrator that can easily be attached and coupled to a well-defined sound source (e.g., a pistonphone) would be required.

The experimental setup shown in Figure 5(b) was a simple example of a sound source that is located directly in front of the entrance of the tube. To study the SIAF concept for other arrangements, time-harmonic finite element simulations ($f = 300$ Hz) were carried out in two dimensions using free field conditions for the outer boundary of the analyzed area. It was found, that a SIAF placed in a certain distance to the surface of the source would again act as a local absorber that changes the direction of the energy flow as motivated by Figure 8(a). If two uncorrelated sources are present, and the SIAF would again not be collocated to one of these sources, the time average of the local intensity in longitudinal probe direction would be measured, as shown in Figure 8(b). This quantity would be determined by the sound field generated by these interfering sources. If the SIAF is placed between two sources with equal strength, as illustrated by Figure 8(c), the uni-directional intensity component of the source facing the open end of the sound tube would be measured.

Using the arrangement consisting of loudspeaker, accelerometer, and SIAF, compare with Figure 5(b), the prototype was also tested in a typical lab. The reverberation time of this room varies between 0.85 second at 125 Hz and 0.5 second at 400 Hz. The arithmetic mean in the frequency band between 100 Hz and 5 kHz is given by 0.64 second and corresponds to values desired for rooms of medium size (250 m^3–5000 m^3), see [19]. In this situation, a positive sound intensity was measured for every tested frequency, if active noise control based on wave separation in time domain was applied. The data shown in Table 1 indicates that a SIAF can also be used to detect acoustic hot spots in weakly damped interiors as proposed in [7].

The sound intensities that were measured directly in front of the loudspeaker using the conventional sound intensity probe—without the surrounding sound tube and without active control—are also listed in Table 1. The comparison of the results proves that the SIAF was indeed capable of detecting the loudspeaker as an acoustic source. In contrast to the calibration test that was performed under idealized conditions, the magnitudes of I_{SIAF} (with control) and I_{Conv} cannot be compared, because the first quantifies the energy transport of travelling plane waves that are absorbed inside the SIAF, whereas the second quantifies the circulation of energy in the (partly active and partly reactive) near field of an acoustic source that acts in a standing wave field.

It is obvious that it is more sophisticated to calculate the plane wave error for sound fields excited by more complicated sources than used in the calibration tests. Nevertheless, to identify a sound source by application of the SIAF approach that works under conditions in which conventional methods cannot be used, it is sufficient to detect a positive energy flow, even if the absolute values are not equal to values that can be measured with sensors of top-level quality.

4. SUMMARY AND OUTLOOK

The functioning principle as well as a prototype of a new sound intensity probe was presented. It was found that a free field can be realized inside this probe by active noise control, if a microphone pair in combination with a wave separation approach is used to determine the reflected wave components. The FxLMS algorithm was used for the signal control task using an accelerometer as a nonacoustic reference sensor. This approach will be sufficient, if access to a signal which is linearly related to the disturbance is given (e.g., in an acoustic test center or during acoustic ground tests of new aircrafts). It was shown that a sound intensity probe with an active free field can be calibrated successfully inside an anechoic chamber, if the finite difference approximation errors that appear during numerical calculation of the pressure gradient based on a two microphone technique, the near field error, and the deviations between plane wave propagation in one dimension and spherical wave propagation in three dimensions are taken into account. But, at this stage of development, the accuracy of the SIAF is of course not as high as the accuracy of well-established conventional probes. It was also found that, because of the active-free field inside the probe, a SIAF is capable of detecting an acoustic source inside standing wave fields that typically appear in weakly damped interiors. Future research will be focussed on the development of a calibration procedure that allows calibration outside an anechoic chamber. To be independent of a reference signal that is well correlated to the disturbance, the application of a stable feedback controller is intended. Furthermore, it is planned to redesign the shape of the open end of the SIAF in order to smooth the change of impedance along the inlet of the probe by conical or exponential horns.

REFERENCES

[1] J. J. Christensen and J. Hald, "Beamforming," *Technical Review 1*, pp. 1–35, Brüel & Kjaer, Naerum, Denmark, 2004.

[2] J. Hald, "STSF—a unique technique for scan-based near-field acoustic holography without restrictions on coherence," *Technical Review 1*, pp. 1–50, Brüel & Kjaer, Naerum, Denmark, 1989.

[3] J. D. Maynard, E. G. Williams, and Y. Lee, "Nearfield acoustic holography: I. Theory of generalized holography and the development of NAH," *The Journal of the Acoustical Society of America*, vol. 78, no. 4, pp. 395–1413, 1985.

[4] K. R. Holland and P. A. Nelson, "Sound source characterization: the focussed beamformer vs the inverse method," in *Proceedings of the 11th International Congress on Sound and Vibration (ICSV '04)*, pp. 1913–1920, St. Petersburg, Russia, July 2004.

[5] J. Drenckhan and D. Sachau, "Identification of sound sources using inverse FEM," in *Proceeding of the 10th International Congress on Sound and Vibration*, pp. 1913–1920, Stockholm, Sweden, July 2003.

[6] T. Kletschkowski and D. Sachau, "Noise source identification using a sound intensity probe with active free-field," in *Proceedings of 8th Conference on Active Noise and Vibration Control Methods*, Krakow-Krasiczyn, Poland, June 2007.

[7] D. Sachau, J. Drenckhan, and I. Schäfer, "Schallintensitätsdetektor sowie Verfahren zum Messen der Schallintensität," 2004, Patent Application No. 10 2004 009 644.9, Germany.

[8] H. Freienstein and D. Guicking, "Experimentelle Untersuchung von linearen Lautsprecheranordnungen als aktive Absorber in einem Kanal," in *Fortschritte der Akustik (DAGA '96)*, pp. 112–113, Bonn, Germany, February 1996.

[9] M. Utsumi, "Reduction of noise transmission in a duct by termination impedance control of a sidebranch resonator," *Journal of Vibration and Acoustics*, vol. 123, no. 3, pp. 289–296, 2001.

[10] "Acoustics—determination of sound absorption coefficient and impedance in impedance tubes—part 2: transfer-function method," 2001, EN ISO 10534-2.

[11] M. J. Crocker and J. P. Arenas, "Fundamentals of direct measurement of sound intensity an practical applications," *Acoustical Physics*, vol. 49, no. 2, pp. 163–175, 2003.

[12] D. Guicking and K. Karcher, "Active impedance for one-dimensional sound," *Journal of Vibration, Acoustics, Stress, and Reliability in Design*, vol. 106, pp. 393–396, 1984.

[13] M. S. Kou and D. R. Morgan, *Active Noise Control Systems: Algorithms and DSP Implementations*, John Wiley & Sons, New York, NY, USA, 1996.

[14] F. Jacobsen and H.-E. de Bree, "A comparison of two different sound intensity measurement principles," *The Journal of the Acoustical Society of America*, vol. 118, no. 3, pp. 1510–1517, 2005.

[15] S. Baker, "An acoustic intensity metes," *The Journal of the Acoustical Society of America*, vol. 27, no. 2, pp. 269–273, 1955.

[16] M. Hamann, *Ein Beitrag zur Realisierung eines Schallintensitätsmessverfahrens*, Ph.D. dissertation, University of Hannover, Hannover, Germany, 1980.

[17] Datasheet PU sound probe. Microflown technologies, Zevenaar, The Netherlands, 2006.

[18] F. X. Pinget, *Aktive Erzeugung der Sommerfeld'schen Randbedingungen unter Verwendung eines neuen Schnellesensors*, Diploma-Thesis, Helmut-Schmidt-University/University of the Federal Armed Forces Hamburg, Hamburg, Germany, 2005.

[19] "Acoustical quality in small to medium-sized rooms," 2004, DIN 18041.

Hindawi Publishing Corporation
Advances in Acoustics and Vibration
Volume 2008, Article ID 603084, 9 pages
doi:10.1155/2008/603084

Research Article

Improvement of Transmission Loss Using Active Control with Virtual Modal Mass

V. Lhuillier,[1,2] L. Gaudiller,[1] C. Pezerat,[2] and S. Chesne[1]

[1] *Laboratoire de Mécanique des Contacts et des Structures (LaMCoS), INSA-Lyon, 69621 Villeurbanne Cedex, France*
[2] *Laboratoire Vibrations Acoustique, INSA-Lyon, 69621 Villeurbanne Cedex, France*

Correspondence should be addressed to L. Gaudiller, luc.gaudiller@insa-lyon.fr

Received 16 January 2008; Revised 1 April 2008; Accepted 19 May 2008

Recommended by Marek Pawelczyk

This paper deals with an alternative modal active control approach to reduce sound transmission through a structure excited by an acoustic wave. Active control makes it possible to conserve lightness while improving acoustic performances. "Modal mass damping control" is proposed for light and small structures having slight modal overlap. The aim of this control is to modify the modal distribution of high radiation efficiency modes with active modal virtual mass and active modal damping. The active virtual mass effects lower eigen frequencies to less audible frequency range while reducing vibration amplitudes in a broad frequency range. An application of this concept is presented in a simple smart structure. It is harmonically excited on large bandwidth by a normal acoustic plane wave. Results obtained by active modal virtual mass and damping control are compared to other modal control approaches.

1. INTRODUCTION

The acoustic transmission loss can be improved by passive methods such as mass addition (Mass Law [1]), double panel, and/or the use of sound absorbing materials. Most of these techniques generally involve an increase in mass or volume to provide a good insulation at low frequencies. However, this is not convenient in the transport sector.

Active control can complete the passive methods and reduce the sound produced by vibrating structures at low frequencies. Various active control strategies have been developed.

In the 1930s, research focused on active noise control ANC (Lueg's Patent [2]) in which a secondary field destructively interferes with the primary disturbance. However, these feedforward controllers are tricky to implement because of the difficulty in measuring reference signal and determining the feedback effect of the secondary sources on the reference sensors. ANC was only successfully implemented in applications, where disturbance is tonal such as ducts and exhaust stacks [3].

Active structural acoustic control (ASAC) controllers were then developed to reduce sound radiation by modifying panel vibrations with shakers or piezoelectric patches.

The ASAC feedforward approach has the same drawbacks as ANC. Moreover, for the low-frequency range, the minimization of sound radiation achieved by "modal restructuring" can increase the vibration levels [4]. This method uses coupling between modes below the critical frequency to create destructive interferences in the radiated field.

If the disturbance signal is not available, control strategies are limited to feedback controllers. The type of controller differs as a function of the availability of a model. Elliott and Johnson [5] showed that at low frequencies, reducing the volume velocity of the panel leads to reduced sound power.

Networks of sensors [6, 7] or distributed sensors such as PVDF film [8] have been implemented to evaluate the volume velocity and to supply an SISO controller. System stability is guaranteed [9] when the actuators and the sensors are collocated and dual. An alternative to SISO controllers called "decentralized MIMO" consists in scattering manifold

independents control units on the structure [10]. The results are fairly good but the technical resources needed are so huge that smart structures cannot be easily introduced in everyday equipment such as double-glazed windows, machinery shielding, vehicles. Moreover, active damping provides good performances without a model, but it is only efficient in the vicinity of a resonance frequency.

The model-based control strategy presents several advantages. It allows minimizing the number of sensors with modal reconstruction [11] and reducing control energy by nonlinear modal control [12, 13]. Complex and nonlinear structures can also be controlled with modal adaptative algorithm [14].

In the vibroacoustic field, accurate modeling is also required to adjust the controller. Baumann et al. [15, 16] proposed to compute sound power by using radiation filters. These filters are introduced in the state space model of the structure and the acoustic energy is incorporated in the cost function. Experiments carried out by Bingham et al. [17] and Dehandschutter et al. [18] demonstrated the validity of this method, but this technique is limited by the number of radiation filters that have to be introduced in the state space formulation.

Below the critical frequency, transmission is mass controlled [1]. Alujevic and Gardonio [19] showed that a light panel controlled by an active virtual mass with decentralized MIMO controllers behaves like a noncontrolled heavy panel. Transmission loss is increased but the sound power peaks still remain due to the lack of active damping.

The aim of this paper is to describe the reduction of sound transmission by modifying the modal distribution. When structures are relatively small and light, the panels have low modal overlap, so in this case, modal control appears to be adapted. It enables limiting the number of active components and concentrating control energy on high radiation efficiency modes. Active modal damping squeezes sound power peaks and controls low radiation efficiency modes which may be excited and transfer vibrating energy to structure bounds. Moreover, above the critical frequency, when the incidence angle is close to the coincidence angle, the behavior of the panel is controlled by damping. Consequently, transmission loss drops dramatically for a lightly damped structure. The effect of adding modal masses shifts the resonance frequencies to a less audible frequency range. Also, the mass control of one eigen mode can be considered as an addition of virtual modal mass. Thus, the acoustic characteristics of the structure should be improved in the upper frequency range.

This paper presents a state feedback controller which acts on modal mass and modal damping. After the state-of-the-art presented previously, Section 2 deals with modeling the structure and the method used to compute the sound power. Section 3 introduces the vibroacoustic controller driven by modal accelerations and modal velocities. The principle of this new "mass damping vibroacoustic modal control" approach is shown in Section 4 on a simple one-dimensional structure excited by a normal incident plane wave. It is then compared to other vibroacoustic modal controls in simulations.

2. MODELING

2.1. Structural modeling

The modal control enables concentrating control energy on high-radiation efficiency modes and limiting the number of active components. Moreover, the effectiveness of this model-based strategy depends on the accuracy of the modeling. The first step consists in building a model that includes the mass and the stiffness of the actuators. The structure is divided into a finite number of elements. The equation of motion governing the dynamic of the controlled system is

$$(M_s + M_a)\ddot{\delta} + C_s\dot{\delta} + (K_s + K_a)\delta = F_d + F_c, \tag{1}$$

with F_d being the disturbance force, F_c the control force, δ the displacement, M, C, K the mass, damping, and stiffness matrices, respectively. The subscripts a and s denote the actuators and the structure, respectively. The control effort driven by the displacement, the velocity, and the acceleration acts on the stiffness, the damping, and the mass of the system, respectively. When the structure is lightly damped and the modes are sufficiently decoupled, the linear system is described by a set of decoupled modal equations after a change of variable:

$$\delta = \phi q, \tag{2}$$

$$\ddot{q}_i + 2\xi_i\omega_i\dot{q}_i + \omega_i^2 q_i = \phi_i^T(F_d + F_c) = f_d(i) + f_c(i), \tag{3}$$

with q_i being the modal amplitudes, ξ_i the modal viscous damping ratio, ϕ_i the modal shapes, and ω_i the frequency of the ith mode. The response v of the structure can be given as a linear combination of the modes:

$$v(x, y, z, t) = \sum_{n=1}^{N} q_n(t)\phi_n(x, y, z). \tag{4}$$

The corresponding modal state variable form is given by

$$\begin{aligned} \dot{x} &= Ax + Bu + Ew, \\ y &= Cx + Du, \end{aligned} \qquad x = \begin{Bmatrix} q \\ \dot{q} \end{Bmatrix}, \tag{5}$$

with x being the state vector, u the control vector, w the disturbance noise, y the output vector, A, B, C, D the state matrices and E the disturbance input matrix. From this formulation, the transfer function of the modal velocities can be easily computed and introduced into the following acoustic modeling.

2.2. Acoustic modeling

To predict the acoustic performances, it is necessary to model the sound radiation of the vibrating structure. The acoustic power W can be calculated from the modal amplitudes and from the frequency dependent radiation resistance matrix of structural modes M [5]. The diagonal terms of M are the self-radiation resistance and the off-diagonal terms are the mutual radiation resistance. The global sound power W can

be obtained by

$$W = \dot{q}^H M \dot{q}, \tag{6}$$

where the subscript H denotes the Hermitian. For complex geometries, M can be calculated from the radiation resistance matrix of elemental radiators and modal shapes. Each element acts as an elementary radiator, where the specific acoustic transfer impedance at position y on an infinite plane to an observation point x is given by

$$z(x, y) = \frac{p(y)}{v(x)} = \frac{j\omega\rho S_e}{2\pi r} e^{-jkr}, \tag{7}$$

with r being the distance between x and y, ρ the fluid density, k the acoustic wave number, and S_e the radiator area. It is assumed that the elementary radiators radiate into free space and are small compared to the acoustic wave length. The sound power radiated by only one single element W_e is equal to

$$W_e = \frac{S_e}{2} \Re\{v_e^* p_e\}, \tag{8}$$

where p_e and v_e are, respectively, the pressure and the complex velocity of the elemental radiator. $\Re$ denotes the real part and $*$ the conjugate. The global acoustic power W radiated by a set of elemental sources is calculated with

$$W = \frac{S}{2} \Re\{v^H p\}, \tag{9}$$

where v and p are, respectively, the velocity vectors and pressure vectors of the radiators. Next, the matrix of acoustic transfer impedances Z linking the pressure at each element to the velocity at each element is introduced. r_{ij} denotes the distance between elemental sources. R_{ij} is the radiation resistance matrix of the elemental radiators. W becomes

$$W = \frac{S_e}{2} \Re\{v^H Z v\} = \frac{S_e}{4} v^H (Z + Z^H) v = v^H R v, \tag{10}$$

with

$$R_{ij} = \frac{S_e}{2} \Re\{Z_{ij}\} = \frac{\omega^2 \rho S^2}{4\pi c} \frac{\sin\, kr_{ij}}{kr_{ij}}, \tag{11}$$

with c being the speed of sound in the medium, ω the frequency, and ρ the mass density of air. The acoustic power can be obtained from the radiation resistance matrix of the elemental radiators and the velocity of structural modes after a change of variable (2),

$$\begin{aligned} W(\omega) &= v^H R(\omega) v = \dot{q}^H \phi^H R(\omega) \phi \dot{q}, \\ M(\omega) &= \phi^H R(\omega) \phi. \end{aligned} \tag{12}$$

Then, for any structures and for any set of frequencies, the radiation resistance matrix of structural modes M can be calculated and approximated using a Laplace-domain multi-input, multiple output transfer function $M(s)$. $M(s)$ is then factorized into a stable causal radiation filter $G(s)$ (13) and $W(s)$ is given by (14)

$$M(s) = G^T(-s) G(s), \tag{13}$$

$$W(s) = \dot{Q}(-s)^T M(s) \dot{Q}(s), \tag{14}$$

with $\dot{Q}(s)$ being the modal velocities in the Laplace domain.

3. MODAL MASS DAMPING VIBROACOUSTIC CONTROL

3.1. Principle

When a structure is excited by a diffuse field below its critical frequency, the transmission is "mass controlled" [1]. The effect of mass addition at low frequency slides the resonance frequencies to a less audible frequency range, while reducing the vibration amplitudes. Therefore, the overall transmission loss is raised. Removing the stiffness scales down the eigen frequencies but increases the level of vibration. Reducing eigen frequencies with stiffness control cannot be considered due to the risk of instability.

If the frequency is slightly greater than the critical frequency, the transmission will be "damping controlled" [1]. In case of lightly damped structures, active damping becomes essential to reduce transmission. At higher frequencies, the good sound insulation does not justify extending the control bandwidth.

In the framework of small and lightly damped structures, the modal control can be effective due to low modal overlap. When the panel is excited by an acoustic plane wave, the low-order modes (odd-odd) are highly excited. Controlling only these high-radiation modes may lead to a considerable reduction of sound power.

The aim of the *modal mass—damping vibroacoustic control*— is to modify the modal distribution of the panel. The natural frequencies of high-radiation modes can be lowered by the addition of active modal mass and vibration amplitudes can be reduced at resonances frequencies by modal damping. The active modal mass can be considered as a *virtual mass* concentrated on controlled modes. Consequently, the amplitudes of mass controlled modes are reduced after resonances due to frequency shifts. Active modal damping limits sound power peaks and the vibrations of low-radiation modes. The control gain matrix is computed with an optimal control algorithm. If the cost function considers exclusively sound power, certain nonradiating modes may be highly excited leading to risks of failure and structure-born transmission. The control is driven by modal acceleration and modal velocities from the derivative state. In practice, modal displacements and velocities are calculated from sensors signals with a Luenberger observer [20]. Then, the reconstructed state feeds the controller whose dynamics is nearly independant of the controlled structure. For simplicity, observation problems are not treated in this article:

$$u = -K\dot{x}_c = -\sum_{i=1}^{N_c} K_v(i)\dot{q}_i + K_a(i)\ddot{q}_i. \tag{15}$$

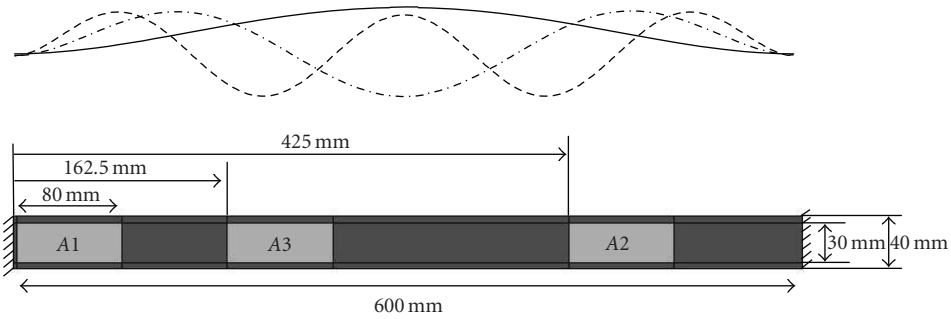

Figure 1: Smart structure.

Then, the active mass and damping can be expressed in the modal equation:

$$\left[1+\underbrace{K_a(i)\cdot f_p(i)}_{\text{Active modal mass}}\right]\ddot{q}_i+\left[2\xi_i\omega_i+\underbrace{K_v(i)\cdot f_p(i)}_{\text{Active modal damping}}\right]\dot{q}_i+\omega_i^2 q_i = f_d(i)-\underbrace{f_p(i)\sum_{j\neq i}K_v(j)\dot{q}_j+K_a(j)\ddot{q}_j}_{\text{Excitation of controlled modes}}, \tag{16}$$

with $f_p(i)$ being the control effort at the ith mode, x_c the state vector of controlled modes, and K_a and K_v the gains relative to modal accelerations and velocities. The state of the controlled system can be calculated from (5) and (15) with the following transfer function:

$$Y(s) = (C - DKs)\left((I + BK)s - A\right)^{-1}EW(s). \tag{17}$$

Next, the modal velocities enables computing the sound power. $\ddot{q}$ is a highpass filter. Consequently, when the frequency is higher than the eigen frequencies of the mass controlled modes and gains relative to the accelerations are high, the frequency response function (FRF) of the control will be constant. The problem of unwanted excitation (spillover) of modes especially above the control bandwidth has to be considered. In the control bandwidth, spillover can be attenuated with good actuator positions. At high frequency, the passive methods are sufficiently efficient. For instance, in the framework of reducing the sound transmission of the double panel (DP) the consequences of spillover on the higher modes are limited due to their good natural transmission loss (TL) in midrange and high frequencies. The performances of DP can be increased at low frequencies without excessive alteration of the TL at higher frequencies by adding modal masses exclusively to high radiation modes.

3.2. Optimization and adjustment

When the structure is assumed to be linear and its model is available, the optimization method used can be the linear quadratic (LQ) algorithm. The constant gains are obtained after minimization of a quadratic cost function. The optimal control seeks to minimize both the state function of structural system x, which is usually vibration energy or acoustic energy, and the control cost u. The control gains are computed by solving Ricatti's equation but using the derivative of state vector $\dot{x}$ does not allow computing gains in this way. If the cost function considers the control energy, the optimal gain may favor damping rather than mass control due to the acceleration FRF. During experiments, the maximal acceptable voltage of the transducers is a factor that limits controller performances. Therefore, the cost function computes the acoustic energy and forbids a control voltage higher than the voltage limit. This can be defined as follows:

$$\text{if } V \leq V_{\max},\quad J = \int_{\omega_{\text{inferior}}}^{\omega_{\text{superior}}} \dot{Q}(\omega)^H M(\omega)\dot{Q}(\omega)d\omega, \qquad \text{if } V > V_{\max},\quad J = \infty. \tag{18}$$

4. APPLICATION TO A ONE-DIMENSIONAL STRUCTURE

The aim of this section is to present modal adjustment possibilities. Constraints such as number of components, dimensions, saturation, and measurements are not discussed in this first study. Simulations are performed on a one-dimensional structure using the previously described control approach. The structure is excited by a normal acoustic plane wave to emphasize active modal mass control within the framework of sound transmission. This modal method enables concentrating control energy on high-radiation efficiency modes and limits the number of actuators. Consequently, the actuators are mainly used to act on the first odd modes. The first step of this control strategy requires using system model.

4.1. Modeling

The smart structure considered and shown in Figure 1 is a clamped-clamped beam to which three piezoelectric patches (P1 89 ceramics) are fixed. The dimensions and material characteristics are given in Table 1. An FE Model is developed using Ansys software, where the beam is modeled with Solid45 elements (8 nodes with 3 mechanical dof/node) of $2.5 \times 2.5 \times 1.5$ mm and the piezoelectric patches are modeled with Solid5 elements (8 nodes with up to 6 dof/node including structural and electrical dof) of $2.5 \times 2.5 \times 0.7$ mm.

Table 1: Simulations parameters.

Beam density	$\rho_{\text{beam}} = 7800\,\text{Kg/m}^3$	Beam width	$b = 4.0*10^{-2}\,\text{m}$
Beam Young modulus	$E = 2.1*10^{11}\,\text{Pa}$	Beam height	$h = 1.5*10^{-3}\,\text{m}$
Modal damping ratio	$\xi_i = 0.01$	Beam length	$l_b = 6.0*10^{-1}\,\text{m}$
Ceramic density	$\rho_c = 7700\,\text{Kg/m}^3$	Patch width	$b_p = 3.0*10^{-2}\,\text{m}$
Ceramic Young modulus	$Y_{11} = 6.67*10^{10}\,\text{Pa}$	Patch height	$e_P = 0.7*10^{-3}\,\text{m}$
	$Y_{33} = 5.26*10^{10}\,\text{Pa}$	Patch length	$l_P = 8*10^{-2}\,\text{m}$
Permittivity	$\epsilon_{11}^s = 1142$	Position 1	$A1 = 2.5*10^{-3}\,\text{m}$
	$\epsilon_{33}^s = 668$	Position 2	$A2 = 4.25*10^{-1}\,\text{m}$
Piezoelectricity	$d_{31} = -108\,\text{pC/N}$	Position 3	$A3 = 1.625*10^{-1}\,\text{m}$
	$d_{33} = 240\,\text{pC/N}$		

For the sake of simplicity, 3 identical patches are bonded to the smart structure.

The first 14 modal shapes are extracted and the optimal position of the actuators are sought by maximizing the coupling coefficient k of *one* high-radiation efficiency mode and minimization of coupling coefficient of other modes. The generalized coupling coefficient k_{ij} of the ith mode for the jth piezoelectric patch bonded to the structure is defined by Hagood and von Flotow [21] as follows:

$$k_{ij}^2 = \frac{\left(\omega_{ij}^D\right)^2 - \left(\omega_{ij}^E\right)^2}{\left(\omega_{ij}^E\right)^2}, \tag{19}$$

where ω_{ij}^D and ω_{ij}^E are, respectively, the natural frequencies of the structure when the piezoelectric jth patch is open-circuited and short-circuited. The modal coupling coefficient is defined by Badel et al. [22]:

$$|\alpha_{ij}| = \sqrt{C_{0P} K_{PD_i} k_{ij}^2} \quad \text{with } C_{0P} = \frac{2\epsilon_{33}^s l_P b}{e_P}, \tag{20}$$

where K_{PDi} is the equivalent stiffness of the ith mode and C_{0P} is the null strain capacitance of the piezoelectric patch. l_P, b, and e_P are, respectively, the length, width, and thickness of the patches. Next, the modal coupling is introduced in (2):

$$\ddot{q}_i + 2\xi_i\omega_i\dot{q}_i + \omega_i^2 q_i = f_d(i) + \sum_{j=1}^{N_{\text{Actuators}}} \alpha_{ij} V_j, \tag{21}$$

where V_j is the control voltage of the jth patch. The results of optimal placement are presented in Figure 1.

Once the structural modeling has been completed, the radiation resistance matrix $M(\omega)$ is calculated in a frequency band from 10 to 900 Hz and approximated using the Laplace-domain multi-input, multiple output transfer function $M(s)$ (14). The eigen frequencies of the smart structure are presented in Table 2.

Table 2: Eigen frequencies.

Mode	1	2	3	4	5	6	7	8
Frequency (Hz)	24	69	130	215	325	451	617	794

4.2. Control gain matrix

4.2.1. Transferring control energy from damping to mass

In order to present the advantages of a derivative state feedback control, the control effort is initially concentrated on modal damping before being transferred to modal mass. The initial terms of the gain matrix relative to damping can be calculated by solving the Ricatti equation stemming from the minimization of the frequency weighted energy cost function (22). Then, the terms relative to modal mass are introduced and those such as maximal voltage actuators inputs remain constant. The modal mass control is applied here exclusively on the first mode because of its high contribution to the sound power. Indeed, at low frequency and for this type of structure, the sound power is mainly radiated by volumetric modes [5].

In Figure 2, exclusive modal damping control is represented in blue. The considered excitation is a normal acoustic plane wave which is uniform on all the plate. The line color gets hotter when the first mode acceleration gain increases. The left-hand plot shows the evolution of the sound power of the controlled system computed with (14) and (17). When the modal acceleration gain increases, the first eigen frequency scales down and the overall sound power is reduced by the active mass. However, limiting the control effort does not allow still introducing as much active modal damping. Consequently, the sound power peak of the mass controlled mode is not reduced as in the exclusive active damping control.

The performances of the controlled systems differ drastically according to the weighting on the mass and damping. If the aim is to reduce the sound power peaks, the control will focus its energy on damping. A good tradeoff between mass and damping can be found when reducing sound power.

The right-hand side plot shows the control frequency response of actuator $A1$. This frequency response becomes constant when the gains applied to acceleration are high compared to those applied to damping. With full damping, the command is like a pass band filter, whereas it is like a highpass filter in mass control. Consequently, the control energy of the vibroacoustic modal mass control is slightly

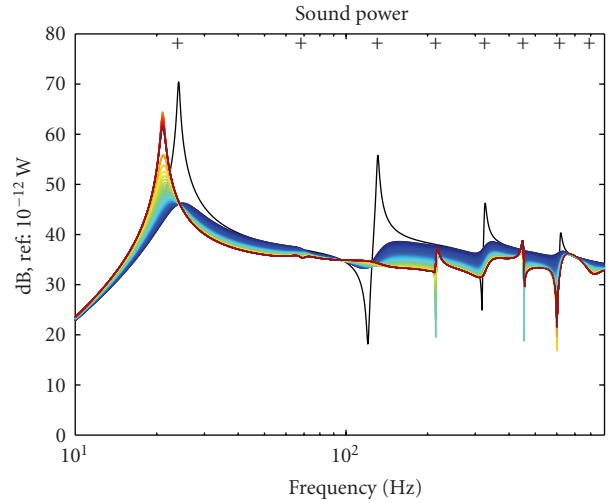

(a)

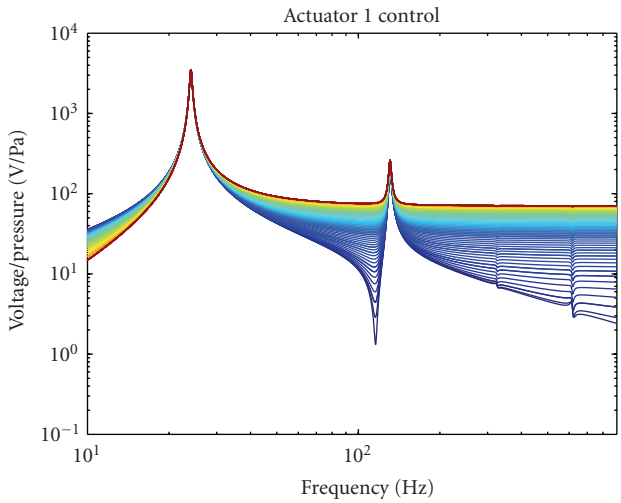

(b)

Figure 2: Transfer of control energy from modal damping to modal mass: (a) sound power, (b) control.

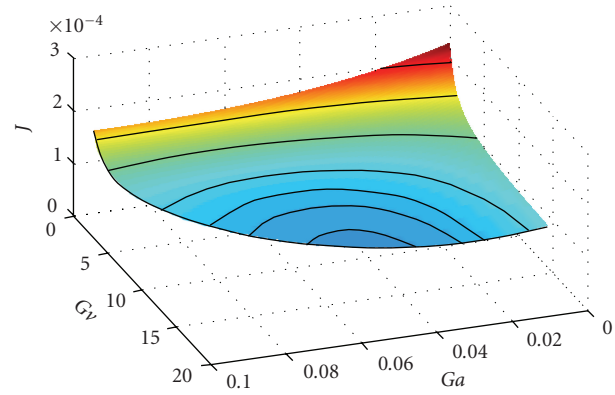

(a)

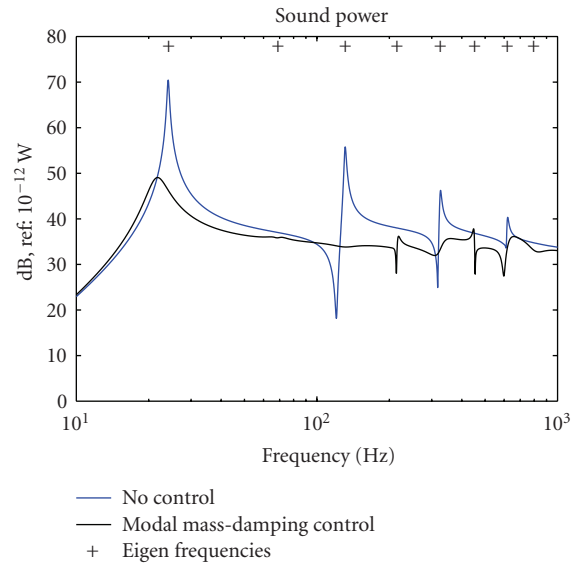

(b)

Figure 3: Evolution of acoustic energy with respect to the acceleration gain and the velocity gain on first eigen mode: (a) sound power with optimal gains (b).

higher than that of the regular state feedback controller. Note that in Figure 2(b), the control voltage is calculated at the initial state which leads to the highest control voltage. So, the first peak of the control appears at 24 Hz.

4.2.2. *Minimization of acoustic energy*

In Figure 3(a), the cost function computed with (18) between 10 and 900 Hz is drawn with respect to the acceleration gain and velocity gain of the first eigen mode. When the control voltage is higher than the maximal acceptable voltage of the transducers, the cost function reaches infinity. The bold line indicates the border beyond which the cost function tends to infinity. The acoustic energy reaches a minimum for a given gain couple. When the gain applied on acceleration is high compared to that on the velocity, the acoustic energy increases because of the peak on the first mode due to the limitation of control voltage. The right-hand side plot shows the sound power of the mass damping controlled system computed with an optimal gain matrix.

The optimal gain matrix is obtained from the results presented in Figure 3. Then, as shown in Figure 4(a) time response simulation of the structure excited by a plane shock normal wave is performed with the optimal gain matrix. The sound power is presented in the left-hand side plot. The high-frequency components of the sound power vanish after a few oscillations due to the active damping on these modes. Consequently, the sound power is mainly created by the first mode which is initially more disturbed. In the right-hand side plot, the first mode velocity shows that the mass effect increases the oscillation period and the amplitude is reduced with active damping.

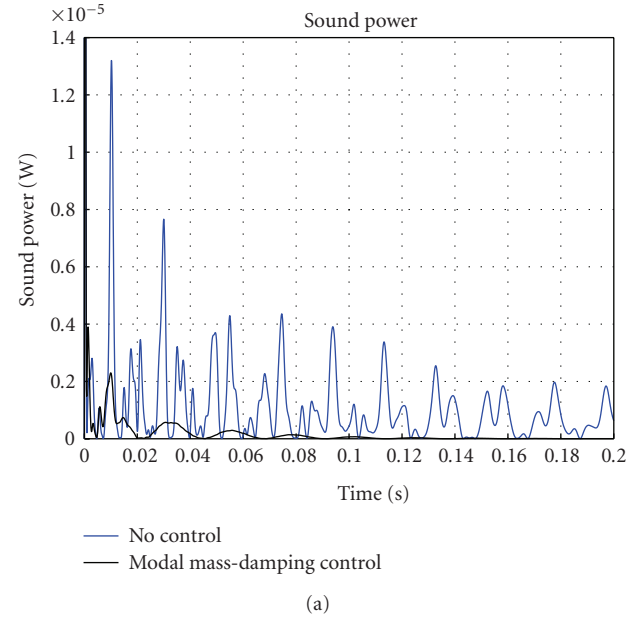

(a)

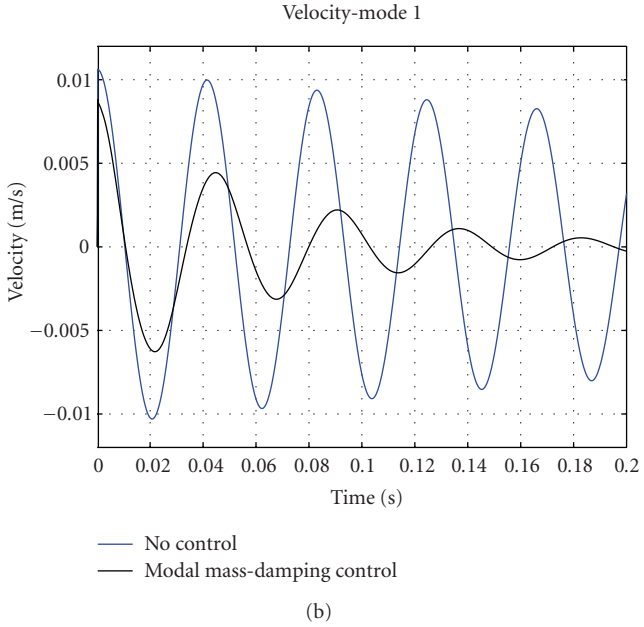

(b)

FIGURE 4: (a) Sound power, (b) first mode velocity.

4.3. Effects of the modal mass control compared to other modal controls

4.3.1. Other approaches

In this section, the modal mass control is compared with two other modal control approaches. The first is a pure vibration control using a regular state feedback control with gains computed by minimizing the frequency weighted (FW) energy cost function (22):

$$J = \int_0^\infty (x^t Q x + \rho u^t u)\, dt. \tag{22}$$

The second control strategy considers vibration and acoustics. In Baumann et al.' [15] development, the radiation filters (RF) $G(s)$ are converted to state space form (23) and introduced in the augmented state space of the system (24):

$$\begin{aligned} \dot{r} &= A_G r + B_G \dot{q}, \\ z &= C_G r + D_G \dot{q}, \end{aligned} \tag{23}$$

$$\begin{bmatrix} \begin{Bmatrix} \dot{q} \\ \ddot{q} \end{Bmatrix} \\ \dot{r} \end{bmatrix} = \left[\begin{array}{cc|c} A & & 0 \\ 0 & B_G & A_G \end{array}\right] \begin{bmatrix} \begin{Bmatrix} q \\ \dot{q} \end{Bmatrix} \\ r \end{bmatrix} + \begin{bmatrix} B \\ 0 \end{bmatrix} u, \tag{24}$$

with z being the result of the passing velocity components through the radiation filter. z^2 is the sound power. In the case of a normal incident plane wave, the general force decays with increasing frequency, which is why an integrator term is added in (26). If the optimal gain matrix is computed by a minimization of z^2, low-frequency modes will not be controlled because the $M(\omega)$ terms are small when the modes do not radiate independently. Consequently, the cost function that considers the disturbance can be written as follows:

$$J_{\text{Rad}} = \int_0^\infty (z_2^T z_2 + \rho u^T u)\, dt, \tag{25}$$

$$z_2 = \mathcal{L}^{-1}(s^{-1} G(s) \dot{Q}(s)), \tag{26}$$

where z_2^2 is the weighted sound power.

4.3.2. Transmission loss

Considering weak fluid-structure coupling, the parietal pressure can be described with the so-called *blocked pressure* [1]. The disturbance load corresponds to the incident pressure is given by

$$p(x) = -2p_{\text{in}}, \tag{27}$$

where p_{in} is the amplitude of the wave of the acoustic plane wave. The transmission loss can be defined as follows:

$$\text{TL} = 10 \log_{10}\left(\frac{W_{\text{in}}}{W}\right), \tag{28}$$

with W being the radiated sound power and W_{in} the incident sound power defined by [23, 24]

$$W_{\text{in}} = \frac{|p_{\text{in}}|^2 l_b \cdot b \cdot \cos(\theta_i)}{2\rho c}, \tag{29}$$

where ρ is the fluid density, c the speed of sound in the medium, and θ_i the incidence angle. For a normal incident acoustic plane wave, $\theta_i = 0$.

4.4. Comparison

Figure 5 presents the transmission losses of the uncontrolled and controlled structure with the three different approaches. The structure is still excited by a normal incident acoustic plane wave that exclusively disturbs odd modes. The

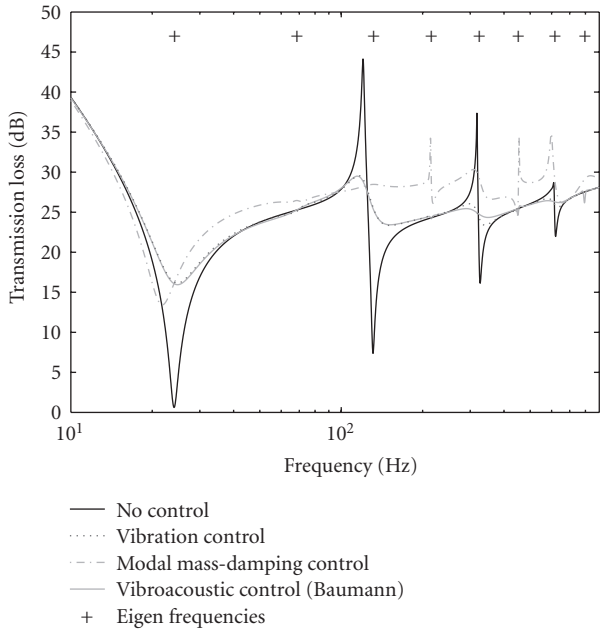

Figure 5: Transmission loss.

three controllers are tuned so that the maximal voltage inputs are the same. The modal mass damping controller uses the optimal gain matrix determined previously. The transmission losses of the FW and the RF controllers have the same characteristics. They give good isolation at resonance frequencies with damping. Consequently, the peaks disappear but the general behavior of transmission loss does not change. Note that the optimal gain matrix of the RF controller is found without searching weighting factors Q as in the frequency weight function (22). The modal mass damping control reduces the peaks at the resonance frequency with damping in the same way as FW and RF controllers, and it also improves the general behavior of the transmission loss due to the mass effect. This active modal mass is above all a mass addition. The reduction of the first eigen frequency from 24 Hz to 21.6 Hz leads to the diminution of modal velocity after the first resonance. Contrary to damping, the mass effect is not limited to the vicinity of the resonance frequency of the controlled mode.

Also, the three controllers can generate spillover. This phenomenon can be limited by considering residual modes in the patch placement optimization and by introducing them in the cost function [9]. Additional passive components are frequently introduced to reduce the spillover induced by the controllers. For future applications such as double panel control, the spillover problem can be limited by the good natural properties of the controllers in midrange and high frequency.

5. CONCLUSION

A new modal active control is proposed in this paper. It permits adjusting a frequency response template of the controlled structure. This control has been developed within an acoustic framework designed to reduce sound transmission through a structure. For each mode, the active modal mass addition lowers the eigen frequency of the mass controlled mode and reduces its velocity after resonance. The use of this method on a simple smart structure equipped with piezoelectric patches is described with an explanation of the concept by way of a simulation. The good performances at resonance frequencies obtained with an active damping controller can be completed with this approach which modifies the modal distribution of the structure. The "mass damping vibroacoustic modal control" is compared to other control approaches which mainly use damping to reduce sound transmission.

This preliminary study can be adapted to more complex structures such as double panels. Indeed double panels provide good transmission loss at midrange and high frequencies, making it possible to concentrate control energy on the first modes. Thus, the method proposed is well adapted to this kind of structure. Moreover, the downward shift of the eigen frequencies can be considered as virtual transformations of structures that could be used in the field of sound quality.

REFERENCES

[1] F. J. Fahy, *Sound and Structural Vibration: Radiation, Transmission and Response*, Academic Press, London, UK, 1985.

[2] P. Lueg, "Process of silencing sound oscillations," Us patent 2043416, 1934.

[3] S. Laugesen, "Active control of multi-modal propagation of tonal noise in ducts," *Journal of Sound and Vibration*, vol. 195, no. 1, pp. 33–56, 1996.

[4] R. L. Clark and C. R. Fuller, "Experiments on active control of structurally radiated sound using multiple piezoceramic actuators," *The Journal of the Acoustical Society of America*, vol. 91, no. 6, pp. 3313–3320, 1992.

[5] S. J. Elliott and M. E. Johnson, "Radiation modes and the active control of sound power," *The Journal of the Acoustical Society of America*, vol. 94, no. 4, pp. 2194–2204, 1993.

[6] T. C. Sors and S. J. Elliott, "Volume velocity estimation with accelerometer arrays for active structural acoustic control," *Journal of Sound and Vibration*, vol. 258, no. 5, pp. 867–883, 2002.

[7] A. François, P. De Man, and A. Preumont, "Piezoelectric array sensing of volume displacement: a hardware demonstration," *Journal of Sound and Vibration*, vol. 244, no. 3, pp. 395–405, 2001.

[8] A. Preumont, A. François, P. De Man, N. Loix, and K. Henrioulle, "Distributed sensors with piezoelectric films in design of spatial filters for structural control," *Journal of Sound and Vibration*, vol. 282, no. 3–5, pp. 701–712, 2005.

[9] A. Preumont, *Vibration Control of Active Structures: An Introduction*, Kluwer Academic Publishers, Dordrecht, The Netherlands, 2nd edition, 2002.

[10] S. J. Elliott, P. Gardonio, T. C. Sors, and M. J. Brennan, "Active vibroacoustic control with multiple local feedback loops," *The Journal of the Acoustical Society of America*, vol. 111, no. 2, pp. 908–915, 2002.

[11] L. Gaudiller and J. Der Hagopian, "Active control of flexible structures using a minimum number of components," *Journal of Sound and Vibration*, vol. 193, no. 3, pp. 713–741, 1996.

[12] L. Gaudiller and F. Matichard, "A nonlinear method for improving the active control efficiency of smart structures subjected to rigid body motions," *IEEE/ASME Transactions on Mechatronics*, vol. 12, no. 5, pp. 542–548, 2007.

[13] F. Matichard and L. Gaudiller, "Improvement of potential energetic exchange using nonlinear control," in *Proceedings of the IEEE/ASME International Conference on Advanced Intelligent Mechatronics (AIM '05)*, pp. 807–812, Monterey, Calif, USA, July 2005.

[14] L. Gaudiller and S. Bochard, "Adaptive active control of flexible structures subjected to rigid body displacements," *Journal of Sound and Vibration*, vol. 283, no. 1-2, pp. 311–339, 2005.

[15] W. T. Baumann, W. R. Saunders, and H. H. Robertshaw, "Active suppression of acoustic radiation from impulsively excited structures," *The Journal of the Acoustical Society of America*, vol. 90, no. 6, pp. 3202–3208, 1991.

[16] W. T. Baumann, F.-S. Ho, and H. H. Robertshaw, "Active structural acoustic control of broadband disturbances," *The Journal of the Acoustical Society of America*, vol. 92, no. 4, pp. 1998–2005, 1992.

[17] B. Bingham, M. J. Atalla, and N. W. Hagood, "Comparison of structural-acoustic control designs on an active composite panel," *Journal of Sound and Vibration*, vol. 244, no. 5, pp. 761–778, 2001.

[18] W. Dehandschutter, K. Henrioulle, J. Swevers, and P. Sas, "Model-based feedback control of acoustic radiation from vibrating structures by means of structural control," *Flow, Turbulence and Combustion*, vol. 61, no. 1, pp. 239–254, 1998.

[19] N. Alujevic and P. Gardonio, "Decentralized feedback control systems in double panel," in *Proceeding of the International Conference on Noise and Vibration Engineering (ISMA '06)*, Katholieke Universiteit Leuven, Leuven, Belgium, September 2006.

[20] D. G. Luenberger, "Observers for multivariable systems," *IEEE Transactions on Automatic Control*, vol. 11, no. 2, pp. 190–197, 1966.

[21] N. W. Hagood and A. von Flotow, "Damping of structural vibrations with piezoelectric materials and passive electrical networks," *Journal of Sound and Vibration*, vol. 146, no. 2, pp. 243–268, 1991.

[22] A. Badel, M. Lagache, D. Guyomar, E. Lefeuvre, and C. Richard, "Finite element and simple lumped modeling for flexural nonlinear semi-passive damping," *Journal of Intelligent Material Systems and Structures*, vol. 18, no. 7, pp. 727–742, 2007.

[23] Q. Mao and S. Pietrzko, "Control of sound transmission through double wall partitions using optimally tuned helmholtz resonators," *Acta Acustica united with Acustica*, vol. 91, no. 4, pp. 723–731, 2005.

[24] J. P. Carneal and C. R. Fuller, "An analytical and experimental investigation of active structural acoustic control of noise transmission through double panel systems," *Journal of Sound and Vibration*, vol. 272, no. 3–5, pp. 749–771, 2004.